University of Southampton

Faculty of Engineering and Physical Sciences

School of Engineering

Laser-Induced Graphene for Structural Health Monitoring of Composite Materials

by

Xue Chen

ORCID ID: 0000 0001 7168 9165

Thesis for the degree of Doctor of Philosophy

June 2025

Supervisory Team

Main supervisor:	Dr. Khong Wui Gan
Second supervisor:	Prof. Suan Hui Pu
Second supervisor:	Dr. Andrew Hamilton
Second supervisor:	Dr. Meisam Jalalvand

University of Southampton

Abstract

Faculty of Engineering and Physical Sciences

School of Engineering

Laser-Induced Graphene for Structural Health Monitoring of Composite Materials

Thesis for the degree of Doctor of Philosophy

by

Xue Chen

Fibre-reinforced polymeric composites (FRPs) have been widely used in aerospace, marine and renewable energy applications for decades due to their light weight, high specific strength, and exceptional corrosion resistance. Structural health monitoring (SHM) enables the detection of undesirable structural changes and damage that improve composites' reliability. Utilisation of laser-induced graphene (LIG) as flexible sensors has recently attracted a lot of interest due to its ease of synthesis and scalable production. However, the integration of LIG as sensors with structural components is challenging due to its fragile microstructure. This PhD thesis overcomes the challenge by demonstrating novel ways of LIG synthesis on composite structures and investigating its sensing performance.

The first part of the thesis presented a novel cork-derived LIG sandwich composite structure for impact damage sensing. A LIG mesh was embedded as the core material of the composite which enables detection of impact damage and its severity. A machine learning (K-Nearest Neighbours) model was proposed to improve the accuracy of damage classification.

The second part investigated the same cork-derived LIG as an embedded sensor for strain sensing under cyclic and monotonic tensile loading. The LIG sensors of different widths showed width-dependent piezoresistivity, with a maximum gauge factor of 133 at 0.08% strain, indicating high sensitivity. LIG piezoresistive behaviour can be described using a mathematical model based on percolation theory.

The third part demonstrated the use of paper-derived LIG directly engraved on glass fiber composites to function as a cost-effective surface strain sensor. The results show that the LIG gives a more stable response to tensile strain compared to compressive strain. A crack-bridge model was developed to describe the piezoresistivity of the LIG sensors. It is also demonstrated that the paper-derived LIG is capable of detecting moisture uptake in the composite structures and solvent leaks, enabling environmental sensing.

Overall, this PhD bridges the gap between low-cost LIG synthesis and its SHM application in self-sensing composite structures. The findings enhance the understanding of LIG's piezoresistive behaviour and lay a foundational framework for the design of LIG sensors for SHM applications.

Table of Contents

Table of Tables

Table of Figures

Research Thesis: Declaration of Authorship

Print name: Xue Chen

Title of thesis: Laser-induced graphene for structural health monitoring of Composite Materials

I declare that this thesis and the work presented in it are my own and has been generated by me as the result of my own original research.

I confirm that:

1. This work was done wholly or mainly while in candidature for a research degree at this University;
2. Where any part of this thesis has previously been submitted for a degree or any other qualification at this University or any other institution, this has been clearly stated;
3. Where I have consulted the published work of others, this is always clearly attributed;
4. Where I have quoted from the work of others, the source is always given. With the exception of such quotations, this thesis is entirely my own work;
5. I have acknowledged all main sources of help;
6. Where the thesis is based on work done by myself jointly with others, I have made clear exactly what was done by others and what I have contributed myself;
7. Parts of this work have been published as:

    1. Chen, X., Gan, K. W., Pu, S. H., Jalalvand, M., & Hamilton, A. R. Laser-induced graphene as an embedded sensor for impact damage in composite structures assisted by machine learning. *Structural Health Monitoring*. *https://doi.org/10.1177/14759217241311516.*
    2. X. Chen, K. W. Gan and S. H. Pu, Laser-induced graphene for moisture and micro-volume liquid sensing. *International Conference on Green Energy, Computing and Intelligent Technology 2024 (GEn-CITy 2024). https://doi.org/10.1049/icp.2025.0257*.
    3. Chen, X., Gan, K. W., Pu, S. H., Jalalvand, M., & Hamilton, A. R. Piezoresistive laser-induced graphene as a low-cost strain sensor for composite structures. Sensors and Actuators A: Physical. *https://doi.org/10.1016/j.sna.2025.116776.*

Signature: ..... Date:.....

Acknowledgements

The journey that has led me to the completion of my PhD thesis in the field of structural health monitoring (SHM) of composite materials began long ago, shaped by my prior research experiences and the skills I developed along the way. This work stands as a culmination of years of dedication, curiosity, and the invaluable support of many individuals who have contributed—both directly and indirectly—to my academic and personal growth. To all of you, I extend my deepest gratitude.

First and foremost, I would like to express my sincerest appreciation to my supervision team, who have been instrumental in guiding me through this challenging yet rewarding journey. Their unwavering support, insightful feedback, and encouragement allowed me to pursue my passion for research, even across two different foreign countries. I am profoundly grateful to Dr. Khong Wui Gan, Prof. Suan Hui Pu, Dr. Andrew Hamilton and Dr. Meisam Jalalvand for their exceptional mentorship, patience, and trust in my abilities. Their guidance not only shaped my research but also taught me the systematic approach to scientific investigation—how to rigorously explore problems, critically analyze results, and effectively communicate findings. Also, I gratefully acknowledge Dr. Wong King Jye from the University of Nottingham Malaysia for his support with SEM imaging throughout this PhD research.

I would also like to acknowledge the institutional and financial support that made this research possible. My sincere thanks go to the University of Southampton (Malaysia Campus) and University of Southampton (UK Campus) for providing the studentship and state-of-the-art facilities. Special recognition goes to the Boldrewood Innovation Campus, TSRL lab and MuVIS X-ray Imaging Centre, where the experimental and validation work was conducted. The facilities and collaborative research environment at these institutions provided an exceptional foundation for my work.

Finally, I owe an immense debt of gratitude to my family, whose unconditional love, patience, and encouragement sustained me through the highs and lows of this PhD. Their belief in my abilities has been a constant source of motivation.

This thesis marks not just the end of a research project, but the beginning of a new chapter in my career as a researcher.

Thank you all.

Chapter 1 Introduction

This chapter presents the research background of non-destructive structural health monitoring for composite structures. The motivation for developing LIG-based smart composites are explained and the research objectives of this PhD work are outlined. This chapter also summarises the thesis structure.

1.1 Background and motivations

In the rapidly evolving landscape of smart composite materials on a global scale, the convergence of functional composite materials, sensor technology, and data analysis techniques pave the way for industrial intelligence integration [1, 2]. Advances in sensor technology have enabled real-time in-situ structural health monitoring (SHM) of composite structures, facilitating the identification of undesirable structural changes and providing operational data for service life cycle management. Over decades, the domain of SHM has witnessed remarkable advancements in non-destructive testing (NDT), which has become a predominant technique in the industry [3]. The NDT technology allows for the detection of discontinuities and cracks, as well as the evaluation of mechanical properties like strain and delamination, all without destructive intervention [4]. The conventional NDT methods include ultrasonic testing, radiographic testing, and thermography, each operating on distinct principles and suited to different applications. The selection of an appropriate NDT method depends on the composite properties, the anticipated defects under the working environment, the required sensitivity, and the budget allocated for monitoring activities. As technology evolves [5], NDT continues to advance, integrating artificial intelligence (AI) algorithms and digital imaging devices to boost the precision and efficiency of inspections.

In recent years, as one of the cutting-edge NDT methods, self-sensing composites, which directly integrate sensing capabilities into the material structure itself, have gained a surge in research interest [6]. Unlike conventional NDT techniques that focus on intermittent measurements at specific intervals, self-sensing composites facilitate a more dynamic and comprehensive inspection of a structure's integrity, thus enabling a direct response to environmental stimuli and mechanical deformations or damage [7]. This advantage is further underpinned by advanced nanofabrication and synergistic integration technologies, which have successfully reduced the processing cost and effort associated with large-scale production of self-sensing composites.

Building on the foundation laid by traditional NDT technologies, the self-sensing composite materials represent a significant paradigm shift towards more integrated, sensitive, and

responsive composite monitoring solutions, necessitated by the higher demands of modern-day SHM applications [8]. In the following, several traditional NDT technologies are summarized, as well as the recently developed self-sensing composites which ushered in a new era of composites health monitoring. This innovation offers potential insights into the state of composite structures, providing a higher level of detail and convenience for industrial applications.

1.2 Motivations for designing LIG-based self-sensing composites

Fibre-reinforced polymeric composites (FRPCs) have been widely used in aerospace, marine and renewable energy applications for decades due to their low cost, lightweight, high specific strength, and exceptional corrosion resistance [9]. However, they typically fail in a catastrophic and brittle manner without warning or visible indication. Advanced structural health monitoring (SHM) technologies could provide operational data needed for service life cycle management as well as reveal the physical condition of FRPCs such that their longevity and reliability can be improved through preventive maintenance [10]. Combination with the sensor technology facilitates the development of self-sensing composites capable of identifying undesirable structural changes, ranging from detection to localisation of subcritical damage size and area before the ultimate failure.

Sensing elements, which are an integral part of self-sensing composites, have a crucial function in detecting diverse external environmental stimuli. Among the diverse array of carbon and metallic sensing materials, graphene-like conductive carbon nanomaterials attracted considerable interest from researchers due to their outstanding electrical transport properties, high chemical and thermal stability, excellent biocompatibility, and lightweight nature [11]. In 2014, Lin et al. demonstrated the capacity to create graphene nanostructures on commercial polyimide (PI) substrates using laser irradiation, further reducing the cost of in-situ graphene generation [12]. In comparison to previous chemical vapor deposition (CVD) or carbon nanomaterials doping methods, the laser-induced graphene (LIG) method substantially reduced the processing equipment requirements and costs in large-scale manufacture [13]. Over the past few years, the LIG method has gained attention as a cost-effective and efficient technique for the single-step production of graphene. Its applications have been widely explored in strain sensing flexible electronics, gas sensing, and functional membranes. However, the use of LIG for structural health monitoring (SHM) structural composite materials is not well studied. There is a knowledge gap in the selection of suitable or compatible substrates for LIG synthesis and its integration with composite materials to develop an application-specific smart system. Its feasibility and sensing performance for various stimuli also require further investigation.

Addressing those issues are crucial for translating the remarkable potential of LIG into tangible solutions for SHM in smart composite systems.

Therefore, this PhD work focuses on exploring and developing LIG-based self-sensing composites for different applications, such as impact damage sensing, strain sensing, and external environmental monitoring. For this purpose, a literature review was done to summarise the previous research of LIG composites. The properties of LIG from different organic substrate are summarized to evaluate the viability of using it as sensing element combined with composites. In general, the morphology and electrical properties of LIG will be modified by laser treatment parameters according to substrate and application requirements. The LIG generation mechanism, lasing parameters, and sensor design are investigated in detail experimentally. The performance and reliability of LIG sensors in various sensing applications will be assessed assisted by a series of data analysis techniques. It is envisioned that the developed system could provide early detection of potential damage or anomalies in the structural health of composite materials in a cost-effective manner, complementing the inspection using established NDT methods which have been well-received by the industrial standards or regulations.

1.3 Research Aims and Objectives

This PhD work aims to investigate the applicability of LIG-based sensors for structural health monitoring of fibre-reinforced composite materials.

The objectives of this PhD work are:

(1) *To characterise and optimise the synthesis of LIG for integration with fibre-reinforced composite materials*

The synthesis of LIG requires an organic substrate to serve as the precursor material. Two inexpensive substrates, i.e. cork paper and brown paper, are selected to study the choice of LIG when placed within or on the surface of the host composite. The quality of the LIG such as electrical conductivity and morphology is dependent on the lasing parameters, such as laser power, line density, and scanning speed. The optimal lasing parameters for LIG synthesis and integration with the host composite are investigated.

(2) *To assess the sensing performances of LIG in composites for different applications*

The sensing performance of LIG as a sensor embedded within the host composite and a sensor placed on the host composite's surface is assessed for various sensing applications, such as impact damage sensing, strain sensing, and moisture uptake sensing. The investigation also allows the understanding of the limitations of LIG sensors.

(3) *To develop simple mathematical models/algorithms for LIG sensor design and application*

Using empirical data, simple mathematical and geometric models are developed to describe the sensing behaviour of the LIG sensors. It can also work with machine learning algorithms to improve the sensing capability. These are essential for demonstrating the technological readiness such that they can be designed and used in real applications with a high level of confidence and certainty.

In this thesis, the feasibility of LIG as SHM sensors for composite structures is demonstrated on glass fibre reinforced polymer composites only as they are electrically non-conductive and therefore will not interfere with the sensing capability of the LIG network. Without any loss of generality, the work developed here can be extended to other non-conductive composites (such as aramid or natural fibre composites) or conductive composites (such as carbon fibre composites) with proper insulation.

1.4 Research novelty

Current research predominantly shows that LIG is synthesised on polymeric films (e.g., polyimide) as the substrates, before it is transferred via intermediate steps to the host materials as sensors, with limited exploration of sustainable substrates or direct integration strategies. This PhD work advances the study of LIG-based sensing in composite structures by investigating low-cost cork and paper substrates for synthesising LIG as embedded and surface-mounted sensors which can be integrated directly with the host composite materials.

The first work package investigated the LIG on a cork substrate embedded within the composite sandwich structure for impact damage sensing. The originality of this work lies first in the direct generation of LIG on sustainable cork substrates before it is embedded as the core of the composite laminates. This approach eliminates the need for LIG transfer steps, and does not incur additional steps to the existing composite manufacturing process. The mesh design of the LIG sensor enables detection of impact damage and its size in a composite sandwich laminate simply by measuring the change of electrical resistance of the LIG channels. Furthermore, the implementation of a machine learning model significantly improves damage classification accuracy, particularly for borderline cases where conventional threshold methods prove inadequate. The systematic post-processing algorithm reduces both manual effort and subjective interpretation errors, thereby enabling efficient large-scale structural health monitoring applications.

The second work package investigated the cork-derived LIG composite sandwich structures with different LIG widths for strain sensing under cyclic and monotonic loading. The experimental results reveal strain dependent piezoresistive behaviour, i.e. linear behaviour at low strains and nonlinear behaviour at higher strains. While prior research has predominantly characterized linear piezoresistive behaviour in LIG sensors, this work extended the study by proposing a simple phenomenological model to describe the non-linear piezoresistivity. These findings enable the reliable design of LIG strain sensors with tailorable sensitivity.

The last work package investigated the LIG sensors directly synthesised on a brown paper substrate pre-attached on the surface of the host composites for strain and environmental sensing. Without the need to bond the sensors on the host material, this paper-derived LIG configuration provides another cost-effective and straightforward solution for strain sensing and early warning detection of structural failure. A crack-bridging model is developed to describe the piezoresistivity of the LIG sensor. The LIG sensor is also sensitive to moisture uptake and exposure to chemical solvents, which can potentially function as an environmental monitoring sensor.

1.5 Thesis structure

The structure of this PhD thesis is outlined as follows.

Chapter 2: Literature Review– This section summarises previous research about graphene-based sensors using electrical resistance change for structural health monitoring of composites. The different forms of graphene-like nanomaterials and fabrication techniques are discussed and compared with the laser-induced graphene method. Moreover, the synthesis mechanism and background of the LIG are explained followed by a comprehensive review of LIG applications in structural health monitoring.

Chapter 3: Cork-LIG for impact damage sensing - This section discusses the synthesis of LIG on cork paper and its incorporation as a core material in FRPC sandwich structure for impact damage sensing. The cork-LIG is characterized to establish the relationship between the LIG's physical properties and the lasing parameters. Using the optimised properties of the LIG, a LIG mesh pattern was designed on the cork substrate and embedded in the glass fibre composite laminates before they were subjected to impact loading. To validate the impact damage sensing capability, the results are compared against the images from X-ray computed tomography which are able to reveal the internal damage of the composite samples. A machine learning algorithm is applied to further improve the accuracy of damage identification.

Chapter 4: Cork-LIG for strain sensing - Using the same laser and laminate configurations defined in Chapter 3, the LIG on cork paper is employed to assess its strain sensing performance under cyclic and monotonic tensile loading. The working mechanism of the LIG conductive network and the geometric effect of LIG on the sensing sensitivity are discussed. A phenomenological model based on the percolation theory is proposed to describe the relationship between electrical resistance, applied strain and LIG width-to-length ratio.

Chapter 5: Paper- LIG for strain sensing - This section presents the synthesis of LIG on brown paper on the surface of glass fibre composite. The LIG morphology and graphitization quality at various lasing parameters are characterised and discussed in connection to their electrical properties. The strain sensing performance of the LIG composite is investigated by cyclic and monotonic loading to figure out the suitable dimension for different operations.

Chapter 6: Paper- LIG composite on environmental sensing - With the same laser and laminate configurations defined in Chapter 5, the potential of LIG on brown paper to monitor moisture uptake in a composite laminate is evaluated. The response of LIG to microvolume liquid droplets is also investigated to study its capacity to detect hazardous chemical leakage or exposure.

Chapter 7: Conclusion and outlook- This chapter summarises the primary findings of this PhD project along with the publication outcome. Some recommendations for the subsequent phase of the research are outlined.

Chapter 2 Literature review on graphene-based sensors for structural health monitoring of composite materials

This chapter summarizes the previous research on graphene-based self-sensing composites. The knowledge gap between the fragile LIG which is commonly used for flexible sensors and its potential for SHM of structural composites is identified. Different manufacturing methods for various sensing applications have been reviewed which can guide the design of novel LIG-based self-sensing composites.

2.1 In-situ NDT techniques for structural health monitoring in composites

Conventional NDT techniques for composite materials include a set of analytical methods based on physical mechanisms such as ultrasound, optical fibre, thermography, radiology, and so on, giving high level of accuracy but often requiring expensive and sophisticated equipment. The suggested domains for the main NDT techniques are as shown in **Figure 2.1**, and the advantages and disadvantages will be presented thereafter [4]. The acoustic emission (AE) can cover a wide range of damage detection [14]. Compared to ultrasonic waves technique, AE detects passive signals generated by material deformation or damage in real-time, using transient elastic waves generated from rapid energy release during mechanical deformation, fracture, or microstructural changes. However, this method faced difficulties when inspecting parts with complex geometries or irregular shapes, especially with high environmental noise.

The ultrasonic techniques use high-frequency sound waves to probe internal structural characteristics [15]. When a transducer emits ultrasonic waves into a material, these waves propagate through it. The wave reflection from any discontinuities, such as cracks or delamination is picked up by the receiver. The ultrasound method is highly effective for evaluating the thickness of materials and detecting flaws that are not accessible from one side only, however, the unpredictable wave reflections will make real-time interpretation obscure when the structure is under loading. Also, the ultrasound method can be time-consuming when applied to large structures, making scanning over extensive areas not viable.

Radiographic testing involves the use of X-rays or gamma rays to penetrate materials and reveal internal structures or defects which mostly focus on micro to meso range [16]. The radiation passes through the material, and a detector on the other side captures the remaining radiation.

The difference in material densities causes the variation in radiation absorption., For instance, defects or material discontinuities can absorb more radiation that the surrounding material and result in darker areas in the radiograph. The radiographic testing is commonly used for detecting volumetric flaws in dense materials, the direct visualization can be reconstructed after the test. This method is expensive due to the specialized facility required, including radioactive sources and protective gear. Only well-trained technician can perform inspections correctly and safely, which limits the application for large scale monitoring in most industries.

Thermography uses infrared cameras to capture temperature variations across a material's surface. The analysis of visual temperature map can reveal the structural anomalies [17]. After applying a stimulus, such as heat or electricity, the abnormal heat signatures that correspond to defects or inconsistencies within the composite can be identified. Nevertheless, thermography is also sensitive to environmental factors. Outdoor conditions such as wind and solar heating can produce false positives or negatives. Therefore, this technique requires a significant temperature difference between the defect and the surrounding material for effective detection, limiting its use in versatile environments, especially when the detecting small defects over large surfaces.

Fibre Bragg grating is a popular SHM methods after 2000s. It relies on the refractive index along the length of the optical fibre embedded in the material which reflects a narrow spectrum of light wavelengths when it is strained [18]. The reflected wavelength shifts proportionally to the strain changes. An anomaly in the signal indicates the presence of composite subsurface defects. On the other hand, optical fibre sensors can be over-sensitive to environmental factors such as temperature and humidity, which may affect their comprehensive performance. Besides, the installation and operation of optical fibre systems is costly, particularly for large-scale. It can also introduce resin pockets which can be a stress raiser affecting the material strength when embedded in composite laminated structures.

Over the past several decades, electrical resistance-based techniques are prevalent in structural health monitoring, especially for composite structures as they do not require expensive support equipment [19]. However, conventional resistivity sensing mentioned in **Figure 2.1** performs better at detecting microscale damage (fibre breaks, microcracks) due to localized resistance changes and macroscale damage (specimen-wide failure) due to bulk resistance shifts. However, at the mesoscale (ply level), delamination or debonding often does not sufficiently disrupt the conductive network in the whole matrix if the damage size is small, therefore the current shunting through adjacent plies limited the damage detection. For conductive fibre reinforced composites, e.g. carbon fibre-reinforced polymer composites (CFRP) [20], changes in the composite's electrical conductivity responding to physical stimuli such as pressure, heat, strain, etc. can be detected and used to monitor the composite's structural health [21]. For

composite reinforced by nonconductive fibres, such as glass fibres, previous research has demonstrated transformative approaches to develop self-sensing composite materials by incorporating conductive fillers such as carbon nanotubes, carbon black, or graphene into the polymer matrices [22]. Carbon nanomaterials can also be coated on fibre or matrix after chemical modification [23, 24]. By strategically manipulating the percolation threshold and spatial distribution of conductive networks, researchers have successfully engineered composites capable to monitor mechanical deformation by measurable electrical resistance changes. These techniques facilitate the development of self-sensing composites that can monitor deformation, damage, and structural integrity in situ via real-time fluctuations in electrical properties, therefore bridging the essential gap between structural performance and autonomous sensing capabilities.

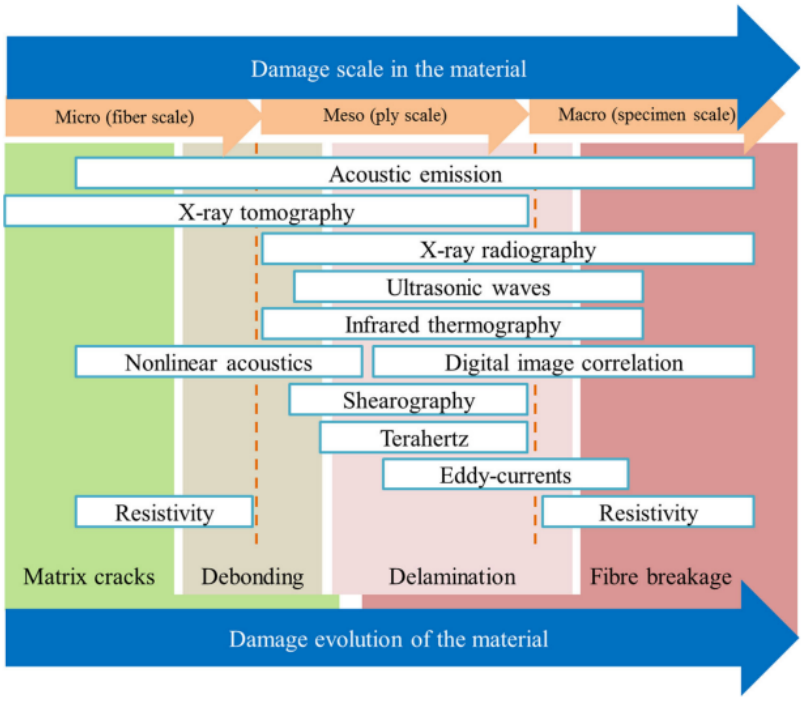

Figure 2.1 Summary of the use of NDT techniques for damage detection (scale and damage mechanism) [4].

Before the discussion of different types of graphene smart composites, several terminologies are listed below to give reference for standard sensor performance description.

Resistive sensor: The resistance changes due to geometric deformation (strain) or material damage. Resistive sensors are simpler and more widely applicable but less sensitive to subtle stress changes [25].

Piezoresistive sensor: The resistance changes the piezoresistive effect—resistance changes due to stress-induced resistivity variations in the material. Piezoresistive sensors are more

sensitive and can detect stress without significant strain, making them ideal for pressure and force sensing [26].

Sensitivity: The ratio of the change in output signal (ΔV or ΔR) to the change in input measurand (ΔM) (e.g., strain, stress, pressure, temperature). Mathematically can be expressed by:

$$S = \frac{\Delta(Input)}{\Delta(Output)} \quad \text{Equation 2.1}$$

Drifting: refers to the undesired, gradual change in a sensor's baseline resistance or output signal over repeated cyclic loading (mechanical, thermal, or electrical). This phenomenon is critical in assessing long-term stability and reliability of sensors, particularly in applications requiring repeated measurements.

Guage factor: A measure of strain sensitivity, defined by the relative resistance change per unit strain. Higher GF sensor gives better strain sensitivity.

Hysteresis: The difference in sensor output for the same input when approached from opposite directions which indicates lag and non-reversibility.

2.2 Graphene-based nanomaterials and smart composites

The incorporation of graphene nanofillers has historically been applied for enhancing the mechanical properties and electrical conductivity of fibre-reinforced composites. By monitoring their electrical resistance, these modified composites are able to detect changes in structural or environmental conditions, such as strain, damage, temperature and humidity [27]. The integration of graphene or graphene oxide (GO) into polymer matrices such as epoxy or polyurethane facilitates the development of resistance-based sensing mechanisms for strain and damage assessment, representing the established paradigm for self-sensing composite systems [28]. Graphene-based materials have large specific surface areas and unique two-dimensional conductive networks, which effectively impart good electrical conductivity to the composite matrix. Researchers have investigated graphene synthesis methods and dispersion techniques for decades with comprehensive characterisation of graphene morphology and structure. The present section will systematically review graphene-based self-sensing composites and their diverse applications, providing a summary of their sensing performance that will serve as foundational comparative benchmarks.

2.2.1 Conventional synthesis methods of graphene-like nanomaterials

2.2.1.1 Chemical vapor deposition (CVD)

CVD is a coating technique for producing high-quality, high-purity thin films, particularly high-performance graphene sheets. In a typical CVD process, vaporized atoms or molecules are introduced into the chamber, where a thermally induced chemical reaction is triggered by the external energy and gaseous reagent support to build the desired film [13]. In the past decade, graphene sheets and fibres have been produced using CVD methods; the most common processing techniques include template CVD, film-scrolling, and secondary growth. Due to its superior structural integrity and relatively large growing area, CVD methods are commonly used in producing high-quality graphene in the laboratory. However, processes are always energy-intensive; high-temperature furnaces that operate at temperatures above 900 °C significantly raise the cost of preparation, making them challenging to scale up for industrial usage. Moreover, these processes require precise temperature regulation and specialized gas flow controllers to ensure consistent graphene formation, hence can only be managed by well-trained technicians.

2.2.1.2 Mechanical and chemical exfoliation

Exfoliation techniques represent another path for graphene synthesis with mechanical and chemical assistance. Mechanical exfoliation, commonly depicted as the “scotch tape method”, implies the mechanical separation of graphene layers from graphite via repeated peeling [29]. This method produces high-quality graphene but in limited quantities, which is not viable for structural composites usage, particularly over extensive areas. Chemical exfoliation, on the other hand, employs intercalation agents and solvents to create interlayer spacing, facilitating graphene sheet separation [30]. This method can be performed under ambient conditions using inexpensive laboratory equipment, including simple mechanical tools and chemical reaction vessels. However, although chemical exfoliation enhances production with little compromises in graphene crystalline quality, the usage of chemicals is a challenge for large-scale manufacturing amid the growing need for environmentally sustainable practices.

2.2.1.3 Liquid-phase exfoliation

Liquid-phase exfoliation emerges as a third critical graphene synthesis method, which can produce graphene based on increased interfacial energy [31]. Using a sonication bath to generate cavitation forces between layers, high-aspect-ratio graphene nanosheets can be achieved after van der Waals forces are weakened. With high shear mixing equipment, e.g. planetary mixers, in organic solvents with specific surface energy characteristics, a large amount of graphene layer can be separated by significant shear forces. The requirement of fairly inexpensive equipment

and the less chemical requirement enhance its potential for large-scale production. However, the resultant graphene has decreased crystalline quality and purity, requiring complicated processing in centrifugation to separate unexfoliated graphite and other contaminants.

Overall, the conventional graphene synthesis methods involve complex processing protocols and substantial investment. However, the methodological framework and experimental evaluation developed from previous self-sensing composites can provide valuable insights for the LIG-based self-sensing composites studied in this thesis.

2.2.2 Previous studies of graphene-based self-sensing composites

The fibre-reinforced composites with graphene nanomaterials have emerged as an economically viable strategy for enhancing mechanical performance and electrical conductivity. Two predominant methods have been utilized: surface coating of non-conductive fibres and graphene dispersion within the composite matrix. Through systematic electrical resistance monitoring, these modified composites enable the detection of structural deformation, thereby establishing a foundational work for self-sensing fibre-reinforced composite systems.

2.2.2.1 Graphene surface coating of non-conductive fibres

Coating fibres/fabrics with graphene nanomaterials is feasible because nanoparticles without functional groups tend to spread evenly due to van der Waals interactions. In composite materials, graphene coatings provide the conductive path for electrical resistance change measurement, simultaneously enhancing mechanical strength and durability under multiple cyclic operations, especially, for non-conductive fibre, e.g. glass and natural fibre. Dip coating, electrophoretic deposition, and pad-dyeing are the processes commonly utilized. In a previous study, Balaji and Sasikumar [32] manufactured reduced Graphene Oxide (rGO)coated glass fibre reinforced epoxy composites by dip-coating a single bundle glass fibre into the mixture of rGO and epoxy resin. **Figure 2.2** depicts the dip coating process of rGO on glass fibre and the electrical measurement apparatus of rGO-coated glass fibre within the glass fibre composites. The nanoscale thickness of the rGO coating enables strain and damage sensing, and a good linearity of piezoresistance response is observed during the low-strain deformation phase (below 3.7% strain). In the subsequent loading phase, the permanent damage induced in the polymer composites significantly disrupts the effective conduction path in the coated glass fibre, which is shown via the nonlinear variation in the piezoresistive response under high strain. Despite the great capability of graphene-coated sensors to monitor composites under strain, the manufacturing process is complicated due to the time and energy-intensive steps of prewashing, dispersion, reduction, and continual heating and drying.

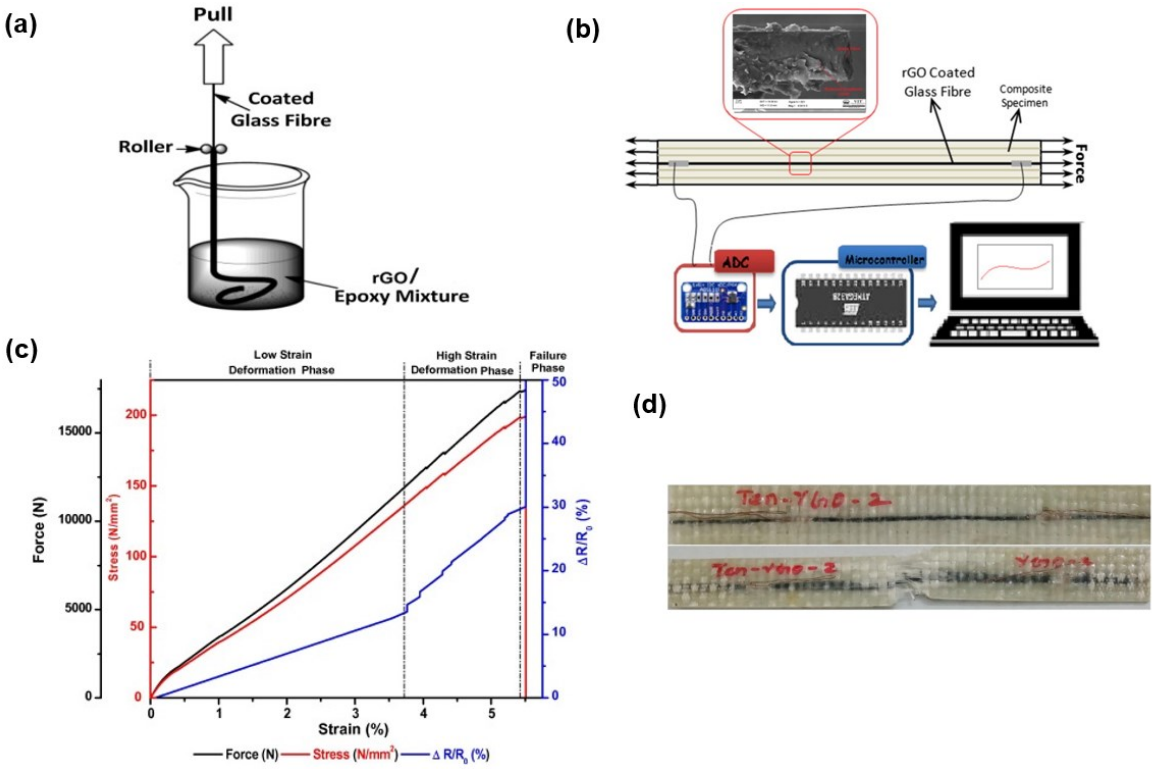

Figure 2.2 The rGO-coated glass fibre reinforced epoxy. (a) The schematic of epoxy dip-coating of rGO on glass fibre. (b)The schematic diagram of electrical measurement setup within the GFRP. (c) Normalized piezoresistivity response of embedded rGO coated GFRP under uniaxial tension loading(d) Image of rGO coated glass fibre embedded composite specimen [32].

Mahmood et al. deposited GO nanosheets on glass fibres using a novel electrophoretic deposition (EPD) method [33]. **Figure 2.3 a** depicts the glass fibres (attached to a metallic window frame) positioned close to the anode to facilitate deposition during the oxidation reaction. After 1 hour of bath-sonication, GO powder was dispersed in water. After hydrate vapourise at 100 ℃, the GO coating is reduced to rGO coating and the volume resistivity value drops to as low as 100 Ω/cm. Both GO and rGO-coated composites exhibit superior fibre-matrix interfacial adhesion in **Figure 2.3 b**, as well as improved mechanical test performance under a variety of loading configurations, including three-point bending, short beam shear, and mode-I fracture toughness. The piezoresistive response under dynamic conditions is evaluated by the electrical resistance which changes proportionally to the applied strain. **Figure 2.3 c and 2.3 d** depict the results obtained under cyclic tensile and bending loading, indicating that sample exhibits better reversibility in tensile elongation compared to cyclic bending, with a gauge factor of around 3.8.

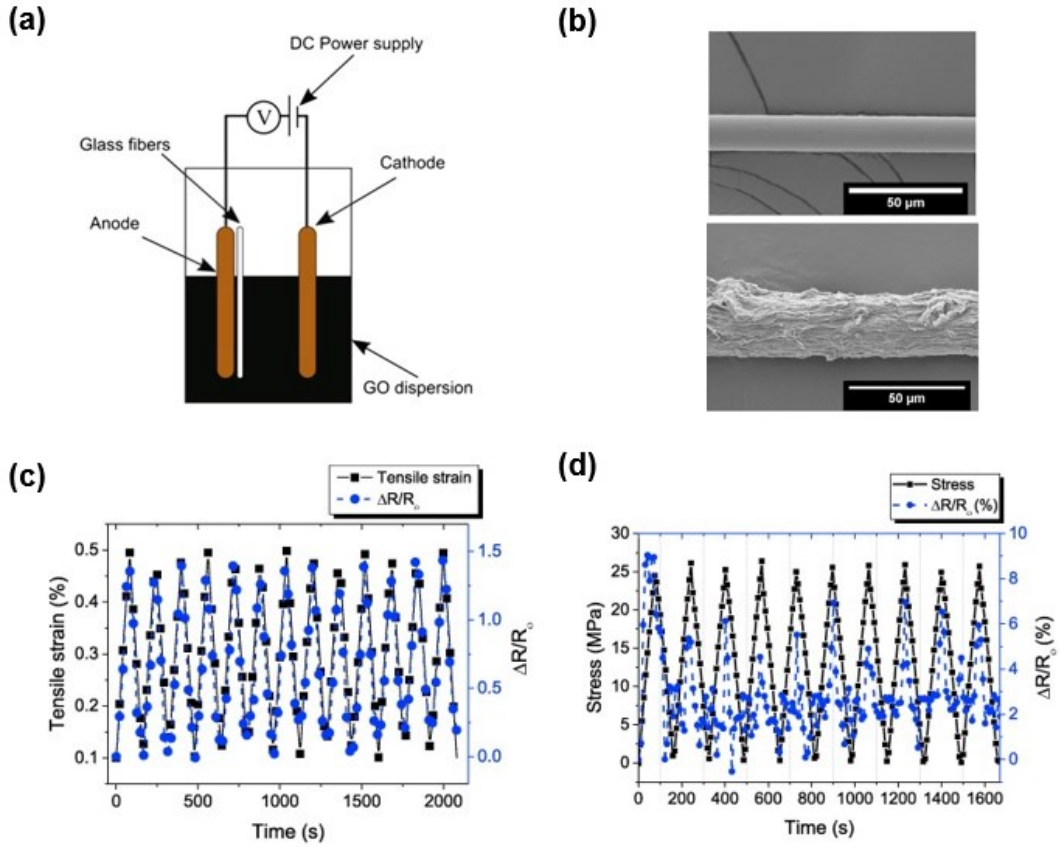

Figure 2.3 (a) The configuration for EPD processing of GO nanosheets on glass fibres. (b) Scanning electron microscopy images of bare glass fibre (top) and glass fibre coated with GO (bottom). (c) Piezoresistivity response of unidirectional composites with rGO coated glass fibres under cyclic tensile elongation tests and (d) under cyclic bending tests (tension) [33].

Overall, the coating of graphene nanomaterials provides good strain sensing performance, but still a few restrictions that hamper mass-scale industrial applications. For example, it is challenging to obtain a uniform dispersion of graphene nanomaterials solvent for coating preparation. These materials have a tendency to aggregate producing clusters or bundles. In addition, the coating processing of structural composites necessitates specialised fabrication equipment and additional reduction stages which can be complicated and time-consuming. For large size self-sensing composites, it is difficult to integrate this fabrication method into existing production lines or to scale up production. Consequently, graphene coating technologies are mainly preferred for body motion sensing, which demands greater flexibility, compared to their application in structural health monitoring.

2.2.2.2 Graphene dispersion within the composite matrix

The graphene-based nanofillers with excellent electrical conductivity such as graphene platelets (GnPs) and carbon nanotubes (CNTs) and graphene are commonly dispersed in composite matrix. On top of constructing the electrical network, the graphene dispersion enhances the

interfacial interaction by increasing the surface roughness of the reinforcing fibres. The expanded contact area between the matrix and fibres enhanced the composite mechanical properties.

Han and coworkers[34] created a self-sensing composite of epoxy resin and GnPs that can detect micron-size damage and provide real-time monitoring of the epoxy curing process. The electrical conductivity increases by orders of magnitude from 2% to 6 vol% of GnPs. The authors invented a unique approach to detect epoxy curing phases connected to matrix shrinkage which brings GnPs closer and reduces electrical resistance. It is important to mention that the researchers were able to identify the spot of the damage by utilising copper strips as eight distinct channels to monitor the electrical resistance change at the local level. The greatest relative resistance variation among the channels indicates the area where damage manifests as drilled holes and cracks. **Figure 2.4** depicts a diagram of drill damage and a heat map of damage localization. However, the noticeable reduction in tensile strength occurred because GnPs nanoparticles act as a partial stress raiser, making areas with agglomeration of a large number of nanoparticles prone to tensile failure in the polymer matrix.

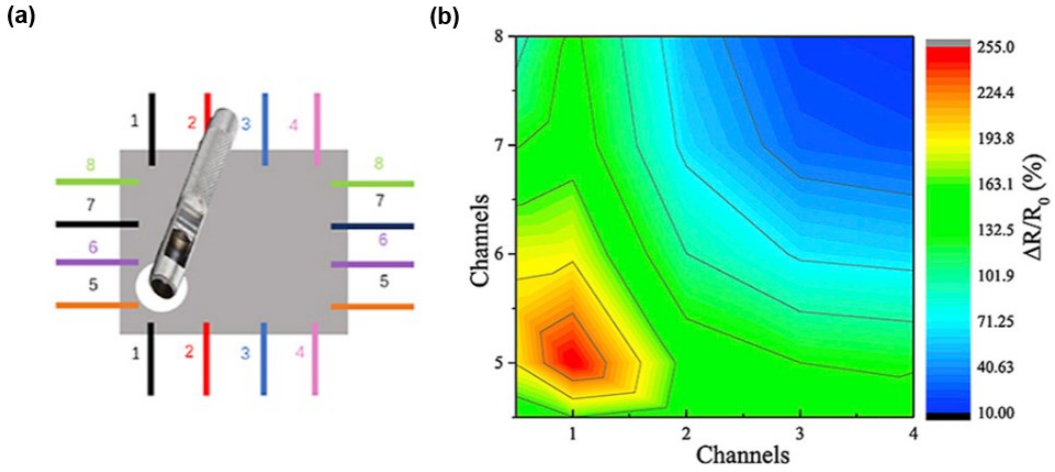

Figure 2.4 Electrical response for self-sensing damage (a) schematic of a drilled hole. (b) the electrical resistivity measurement heat map [34].

In conclusion, graphene materials dispersed in liquid composite matrices can modify the electrical properties of composites and facilitate self-sensing capabilities, there are still limitations that prohibit the widespread application of this technique. First, in the context of strain sensing, the fabrication of graphene is comparatively costly when compared with traditional external strain gauges, particularly for large composite panels. Second, it can be challenging to disperse graphene nanofillers uniformly through the epoxy matrix and to maintain uniform mixing during the curing process. Suspended graphene materials tend to agglomerate, producing clusters that reduce the overall effectiveness of nanofillers as well as compromise the composite's mechanical and thermal stability.

2.3 Laser-Induced Graphene

2.3.1 LIG synthesis mechanism

Laser-induced graphene is defined as the process of generating graphene materials through laser irradiation. In general, the LIG produced by laser relies on the photothermal effect. During laser irradiation, infrared and visible light emit energy as photons, which are absorbed by the polymer molecules and converted into potential energy. The collected energy intensifies the molecular vibration and rotation; the polymeric covalent bonds are then broken as the temperature increases, forming short-chain small molecular groups that can be freed from the substrates [35]. In 2014, the creation of LIG from a Kapton polyimide sheet was first reported [36], wherein laser irradiation disrupts C-C and C-O bonds, resulting in a porous 3D LIG structure as gaseous products are released during the photothermal conversion of sp^3-carbon atoms to sp^2-carbon atoms.

On the other hand, the energy of a single photon in a short-wavelength laser also produces photochemical reaction, such as blue and UV light have greater energy than 300kJ/mol, which is sufficient to directly break chemical bonds such as C-C and CO bonds, releasing more energy in a shorter period and converting less energy into heat [37]. Previous research has shown that UV emits photon energy in the same order of magnitude as covalent bonds, minimizing the volume of the decomposition process [38]. As a result, the temperature rise will be smaller, and the substrate deformation will be less significant. However, it is important to note that when the laser energy contacts the polymer, however, it is not completely absorbed by the polymer; instead, some of the energy is reflected after it meets up with the material surface, and if the substrates are partially transparent or translucent polymer materials, a large amount of laser energy is directly transmitted. **Figure 2.5** depicts a sketch of the polymer substrate response after laser treatment. Thus, transparent substrates are unsuitable as LIG precursors due to their energy absorption efficiency. Energy reflection must be considered when selecting a suitable substrate for the LIG self-sensing composites.

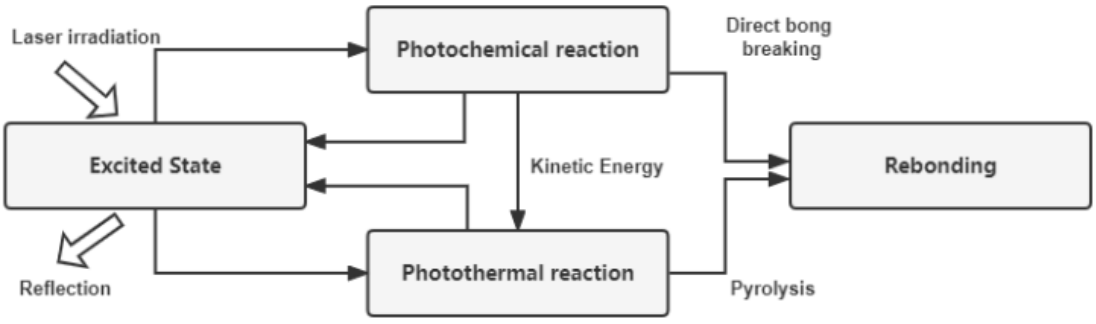

Figure 2.5 The reactions of polymer molecules are caused by laser irradiation.

2.3.2 Working mechanism of LIG-based damage sensing

The LIG network as a sensing element in the non-conductive composite matrices can be considered as a heterogeneous sensor. Changes in the conductivity or resistance of a heterogeneous strain sensor are mostly caused by changes in the conductive network separation [39]. Variations in the distance between the nanoparticles due to mechanical perturbation will alter the conductive path. Moreover, the 3D structure of LIG makes it even harder to predict how the electrical resistance and conductivity will change in different directions. For example, horizontally stretching along the in-plane directions along x and y axes may cause the vertical structure of the LIG to collapse, providing more contact between the graphene layers that may cancel out the increase in electrical resistance caused by in-plane elongation. Therefore, in comparison with metal-based strain sensors or monolayer graphene structures, the electrical conductivity experiences greater fluctuations, requiring an extended duration for internal nanostructure rearrangements, leading to elevated noise-to-signal ratios especially in cyclic strain sensing. To stabilise the electromechanical sensing response of LIG-based sensors in composites, matrix infiltration into the porous LIG can provide mechanical support to the LIG microstructure. The LIG connections are pressed into contact or pulled apart during the compression and tension loading, which leads to a decrease and an increase in electrical conductivity response. **Figure 2.6** shows the schematic of the LIG component under strain or after impact damage.

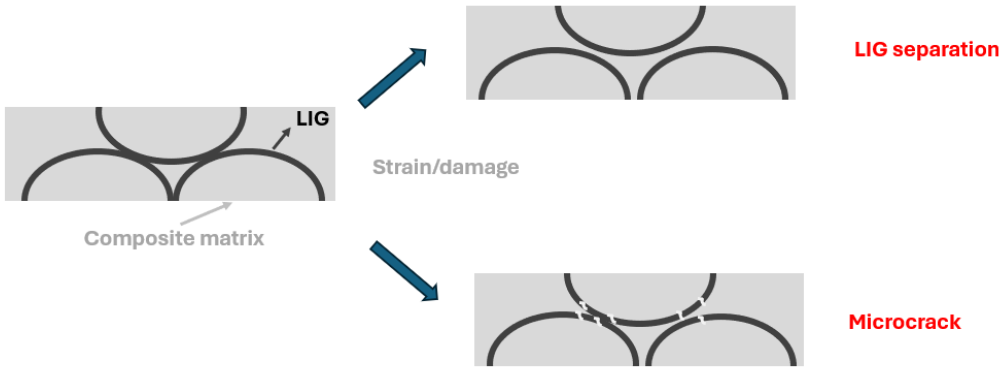

Figure 2.6 The schematic of LIG-based composites working mechanism.

Other key phenomena that influence the LIG sensor are caused by changes in the size of the micropores. For example, the interparticle distance change will directly affect quantum tunneling probabilities. As the distance expands, the tunneling probability will reduce exponentially. For charge hopping, the mechanical strain can alter the energy landscape by changing the potential barriers between the conductive sites or the spatial arrangement of conductive elements. Therefore, it is often observed that slight compression could initially enhance conductivity by

optimising tunneling and hopping paths; however, excessive strain inevitably damages the network, resulting in a significant rise in electrical resistivity [40]. In the following chapters, we simplify the complex electrical charge transformation at the nanoscale and assume that LIG sensors infused with resin serve as a homogeneous conductive channel for monitoring electrical resistance. The electrical response under strain will be examined individually based on various LIG substrates and geometric patterns.

2.3.3 Laser treatment parameters and LIG quality

The most extensively employed methodology for investigating novel materials is the processing–structure–property–performance (PSPP) relationship. For graphitic hierarchy structure (a few layers of LIG packed together to make a 3D network), both the laser and substrate conditions determine the morphology and defect levels of the LIG structure, resulting in different sensitivity and dynamical response patterns. According to prior research [41], the commonly employed laser parameters include power, wavelength, focal conditions, and scanning speed. The parameters for the substrate are typically substrate composition and thickness, and the controlled environment includes ambient air, nitrogen, argon, and hydrogen. The presence of many processing parameters makes it challenging to determine the correct ones to obtain the desired nanostructure, hampering the commercialization of the LIG-based composites.

Researchers attempted to correlate LIG characteristics following laser treatment to their sensing performance; however, the differences in substrates, laser wavelength, irradiation energy, and image density units made it difficult to compare these properties directly. Establishing uniform terminology will assist future studies in providing a baseline for comparison among various application cases. For example, Duy et al. [41] used the term "accumulated fluence" (J/cm^2) to characterize the laser energy density and investigated the initial carbonization energy for various wavelengths. An energy meter was used to monitor the average power for laser treatment in vector and raster modes. Various critical carbonisation points (the start of LIG generation) were determined at different laser wavelengths, which correspond to the distinct laser absorption rates of each wavelength for the PI substrate.

Burke et al. used the phrase "irradiated laser dwell time per pixel" to explore the LIG morphological features and graphitizing level. Based on the observation of the obvious graphene-like carbon peak fingerprints from Raman spectrum and the low sheet resistance, they established that the optimal dwell time window for a low-power 500 mW, 405 nm wavelength, and low-cost laser system is around 50 ms/pix [42]. Using electrical resistance as a function of laser parameters, Wang et al. conducted the first study on the impact of different types of lasers on LIG formation. They discovered that when the same laser fluence was used, the CO_2 laser-

induced LIG exhibited a significantly lower sheet resistance than the UV laser-induced LIG. This could be due to the LIG layer's structural differences, as CO_2-produced LIG has larger pore sizes and fewer graphene layers on average [43].

Luo et al. invented the term "linear laser energy density (LLED)," which refers to the ratio of laser power to scanning speed, as a key laser parameter. The critical thresholds of LLED on PI substrate indicate both the lower energy limitation for LIG generation and the upper energy limitation for substrate deformation. The LIG is not electrically conductive when LLED is below 20 J/m and LLED over 100 J/m resulting in significant substrate distortion, leading the LIG flake to peel off [44]. Based on the previous research, the LIG electrical properties and nanostructure generated from different laser system configurations are summarized in **Table 2.1**, and **Figure 2.7** concludes the basic relationships between LIG quality and laser parameters.

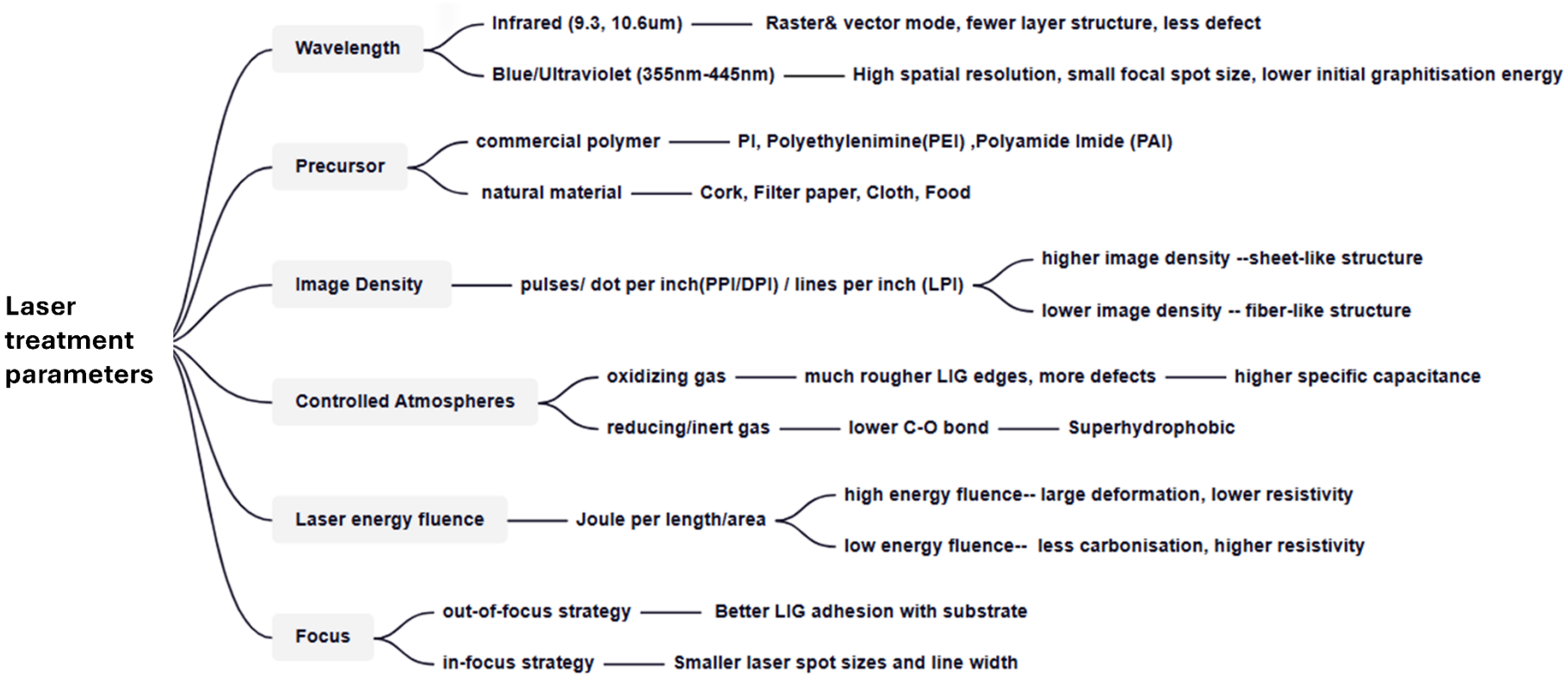

Figure 2.7 The influence of main laser treatment parameters.

The electrical sheet resistance measurement and the Raman spectroscopy are the most common charaterisation methods of the LIG samples. However, the majority of studies focus on the electrical resistivity and graphitization level of pristine LIG. The LIG when integrated within composite materials is not well-studied. Given that LIG defects will significantly increase resistivity and introduce variations, it is worth looking into how various laser parameters affect LIG to produce uniform conductive patterns on diverse substrates. The LIG nanostructure exhibits weak adhesion to its substrates, necessitating a protective encapsulation layer when placed on the composite surface.

Table 2.1 The previous research of relationships between laser parameters and LIG quality on polymers.

Substrate	Power/ fluence	Wavelength (nm)	Image density	Raman peaks (cm^{-1})	I_D/I_G ratio	I_{2D}/I_G ratio	Resistance (Ω/square)	Ref
Kapton PI film(125um)	2.4 - 5.4 w	10600	1000 PPI	1350, 1580, 2700	0.5-1	NA	32-15Ω	[36]
Kapton HN PI film(125um)	0.11 w	405	NA (CNC control)	1350, 1580, 2700	~1	NA	250	[45]
PI paper(90um)	1.25 w	10600	500 PPI	1345, 1580, 2690	0.9	NA	30	[40]
Kapton PI tape (80um)	0.5 w	405	300	1350, 1580, 2700	0.9	0.23	100	[42]
Kapton PI film (125um)	4.3 J/cm^2	355	NA	1350, 1580, 2700	0.9	0.25	400	[46]
PDMS (50um)	0.5 w	405	NA	1350, 1580, 2700	0.8	1.05	5000	[47]
PI tape (attached on PET sheet)	6.75 w	10600		1350, 1580, 2700	0.8	0.7	60	[48]
Kapton PI film(127um)	0.75 w	10600	1000	1350, 1580, 2690	0.8	0.8	40	[49]
Kevlar® KM2+ unidirectional tape	12 w	10600	400	1354, 1580, 2699	0.78	NA	NA	[50]
Kapton PI tape(125um)	3 w	355	150 kHz, pulse duration 1 µs	1350, 1580, 2700	0.68	0.45	240000	[51]

Kapton PI film(127um)	2.5 w	10600	400	1360, 1580, 2730	0.6	NA	46.1	[44]
Kapton PI film(127um)	3.5 w	10600	400	1360, 1580, 2730	0.3	NA	23.4	[44]
Kapton PI film(125um)	6.6 J/cm^2	10600	NA	1350, 1580, 2700	0.3	0.6	100	[46]
Kapton PI film(125um)	122 J/cm^2	10600	1000	1350, 1580, 2700	NA	0.8	NA	[52]

2.4 LIG applications in composite health monitoring

In general, laser induction approach demonstrates a new way of creating graphene-based composite sensors in a one-step process, considerably simplifying the graphene production and patterning process. Prior studies have shown that LIG can be easily generated in ambient air or H_2/Ar aided environments from multiple carbon-based materials. This cost-effective and mask-free method of synthesising high-quality graphene has been thoroughly investigated from manufacturing to specific sensing capabilities. The LIG-based self-sensing fibre reinforced composites are discussed as follows based on their fabrication methods and sensing performance through different sensing applications.

2.4.1 The different fabrication methods of LIG-based self-sensing composites

By bridging the gap between the fragile LIG structures on organic substrate and integrating LIG in smart composite fabrication, researchers attempt to unlock the potential of the LIG in SHM applications through three distinct approaches.

2.4.1.1 Directly conversion of matrix/fibre constituent

Previous research has proven that almost all types of organic precursor can generate graphite after being pyrolyzed. By optimising laser parameters, including wavelength, power, and number of scans, composite materials consisting of organic matrix and reinforcement fibre can be converted to achieve the desired conductive characteristics of LIG. Groo et al. demonstrated the fabrication of LIG strain sensors directly on the surface of GFRP composites and detected damage in the composite, such as delamination and matrix cracking, through changes in electrical resistance [53]. Nasser et al. explored the properties of LIG generated using the laser scribing of aramid fibres [50]. The LIG-aramid fibre reinforced composite with coarser fibre surface exhibited improved electrical conductivity and intralaminar strength. By observing in-situ

ballistic impact damage and delamination, Steinke et al. expand the self-sensing capability of LIG-aramid fibre-reinforced composites [54]. A self-converted approach was devised by Wang et al. to produce composites with strain sensing capabilities by lasing the surface of carbon fibre prepreg and transferring it to the LIG structure within the composites[55]. In summary, those direct LIG generation methods have the capability to incorporate the LIG structure seamlessly into composites, thereby providing excellent stability for LIG sensors.

2.4.1.2 Transfer printing

Transfer printing is a technique used in composite fabrication for transferring functional materials or devices from their original substrates to another substrate with precise alignment and control. The requirements for the new substrate after LIG transfer printing are, firstly, having no reaction with the LIG and minimal impact on their electrical conductivity, and secondly, the capability to preserve the fragile LIG structure during the transfer process. Typically, the transfer target layers include elastomer, polymer, or prepreg that can provide adhesion or infusion to LIG nanostructure adhesion [56]. Groo et al. employed a controlled pressure rolling technique to minimize the impact on the vertical structure of LIG. They embedded the LIG structure into GFRP composites, preserving the LIG's high sensitivity and stability while protecting it against environmental factors [57]. Huang et al. created a novel wavy-LIG strain sensor with high sensitivity and low hysteresis by transferring the LIG constructed from PI film to silicone rubber [58]. In general, the transfer printing method enables the replacement of graphene from fragile precursors e.g. PI to suitable substrates based on the applications required, facilitating the creation of LIG self-sensing devices. However, the transfer process may introduce contaminants or defects into the graphene structure, potentially affecting its intrinsic properties of intricate graphene electrode pattern.

2.4.1.3 Encapsulation or surface protection

Using the LIG together with the original substrate is the best option to preserve the LIG hierarchical structure. However, the LIG structure will experience detachment when subjected to significant deformation. A cover layer is not required for applications where the LIG sensors do not experience contact stresses or large bending angles. To improve the attachment of LIG and PI substrate, for example, Carvalho et al. [51] constructed an extra thin LIG layer with a penetration depth of approximately 5 μm, while keeping the integrity of the underlying precursor structure. Yao et al investigated the internal reflection features of PI film to effectively fabricate a self-sealing LIG within a 50 μm thick PI film, and achieved remarkable mechanical stability [59]. For applications that require the LIG microstructure to be exposed for sensing purposes, such as gas sensors, humidity sensors, and heating elements, some researchers

choose to retain the LIG structure with the substrate [52, 60]. In the design of self-sensing composites, it is often necessary to incorporate extra protection or encapsulation to maintain the integrity and longevity of the LIG nanostructure.

In conclusion, these studies convey the versatility of LIG fabrication techniques applicable to diverse aspects of monitoring the physical conditions of fibre-reinforced epoxy composites, including strain distribution, damage detection, curing processes, interfacial bonding, fatigue behaviour, moisture absorption, and so on. The subsequent section will further review previous LIG composite designs, including the sensing performances in diverse contexts and data processing.

2.4.2 Sensing applications and performance of LIG composites

The determination of the placement of LIG sensing elements in composite structures should be based on individual monitoring requirements. In the case of detecting internal damage, it is sensible to incorporate the sensing devices within the composite structure. Conversely, to effectively monitor material deterioration or physical changes on the surface, it is preferable to locate the sensing layer either on or in close proximity to the composite's surface. The research methodology employed to investigate the individual damage-sensing applications that integrate LIG within FRPs is illustrated in **Figure 2.8**. Based on the applications and manufacturing requirements, one can determine the ideal position of the LIG sensing layer and establish the corresponding design of the LIG composite. Therefore, the sensing performances of the LIG designs incorporated with composites for different applications will be reviewed below.

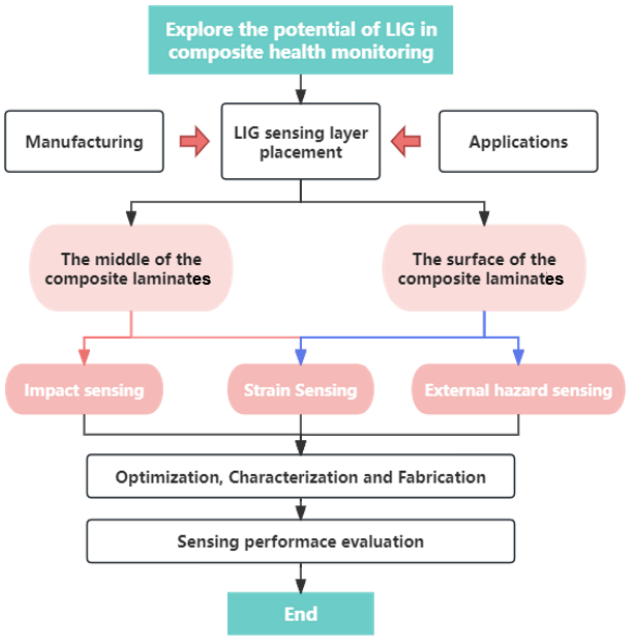

Figure 2.8 The research methodology for investigating the potential of LIG in monitoring the health of composites.

2.4.2.1 Impact damage sensing

The use of LIG composites for impact sensing was less common in prior research. Steinke et al. continue their investigation of LIG generated from aramid fibre; prior to the CO_2 laser treatment, the aramid fabric is prewashed and dried. After laser scanning, vacuum-assisted resin transfer moulding (VARTM) is employed to generate aramid fibre-reinforced polymer composites [54]. **Figure 2.9 a** shows the flow chart of LIG generation process and the VARTM fabrication of the LIG-treated aramid laminates. Since aramid composites are commonly used in high-speed impact applications, the ballistic impact test is conducted to demonstrate the in-situ damage monitoring capability of LIG interface aramid composites. Through the real-time monitoring of electrical impedance by a four-point probe technique, the authors discovered that the impact velocity is directly related to the severity of the impact, and thus correlates to electrical impedance and ply delamination. **Figure 2.9 b** depicts the electrical impedance percentage changes under different impact speeds. The connection electrodes were placed at the parallel edges of LIG which are perpendicular to the resin flow direction. In addition, it was demonstrated that mechanical locking provided by the LIG interface improves both the areal-density-specific V50 ballistic performance and the Mode I interlaminar fracture for aramid composites. Therefore, the LIG-treated aramid fibre demonstrates multifunctional mechanical and piezoresistivity improvement, which enhances interlaminar strength and successfully predicts impact velocity as well as the degree of composite damage.

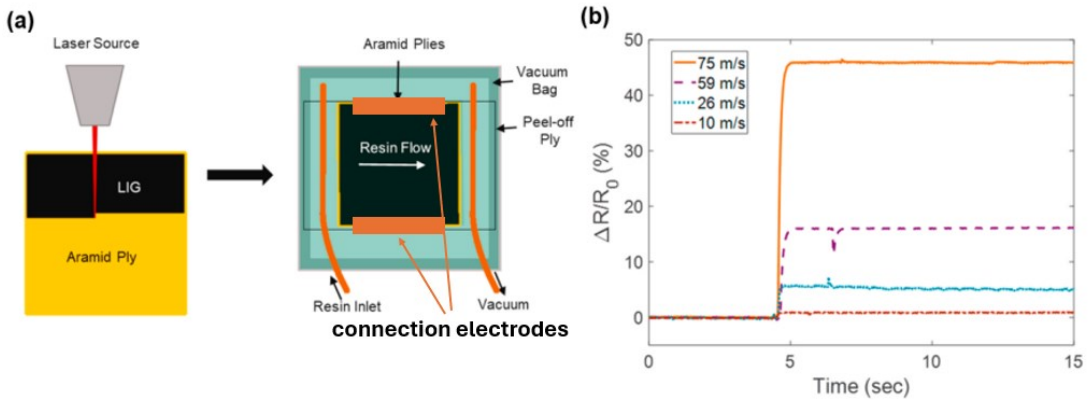

Figure 2.9 The LIG aramid fibre composites for ballistic impact sensing. (a) The schematic diagram of LIG generation and LIG-treated aramid composites fabrication. (b) The corresponding electrical impedance percentage change of impact speed from 10m/s to 75 m/s [54].

2.4.2.2 Strain sensing

The epoxy resin successfully penetrated the fragile LIG layer, resulting in the full integration of the LIG structure into the polymer matrix and providing stability for electromechanical sensing. For strain sensing application, the LIG structure is either generated on or integrated into composites. FRPs typically are very stiff and the suitable strain sensing range for FPRs is limited to a relatively small strain range (2%). Two commonly employed electromechanical tests were conducted to measure the sensitivity of the LIG strain sensors in composites. For the tensile elongation test, the LIG layer can be embedded in the FPRs or applied on the surface. For the bending test, it is more advantageous to apply the LIG to the surfaces as this minimises the influence of interlaminar shear.

To build a fully integrated strain and damage-sensing LIG composite, Groo et al. used a 5.4 W CO_2 laser with a 400 DPI image density to create textured LIG on 25.4 µm PI tape [57, 61]. The constant pressure rolling method was used to transfer printing the LIG design to Solvay E773 prepreg with glass fibres. **Figure 2.10 a** shows the LIG production, transfer, and layup processes, as well as a finished sample with silver paste rings wired out for taking measurements. The LIG nanostructure and alignment were maintained after transfer to the fibreglass prepreg, but the fuzzy texture was converted to a smooth surface immersed in an epoxy matrix. According to scanning electron microscopy (SEM) analysis, the LIG causes the stick-slip effect in composites, which makes it easier for interface energy to dissipate as heat and raises the damping property (average tan angle) by 12%. When a load is applied and the composite under tension strain, small microcracks form within the LIG's microstructure. In the low strain range (0.15% strain), the host fibreglass structure experiences little or no mechanical damage or plastic deformation, the average gauge factor is highly correlated with the initial resistance. **Figure 2.10 b** and **2.10c** show the percentage change in resistance versus strain and the gauge factors of different samples ranging from 0.5 to 1.3 below a maximum strain of 0.15% over 20 cycles of quasi-static loading. In cyclic strain sensing, the response shows no severe distortion and minimal observable latency compared to commercial strain gauges, indicating that transferring the LIG structure to a polymer matrix for future SHM applications is promising.

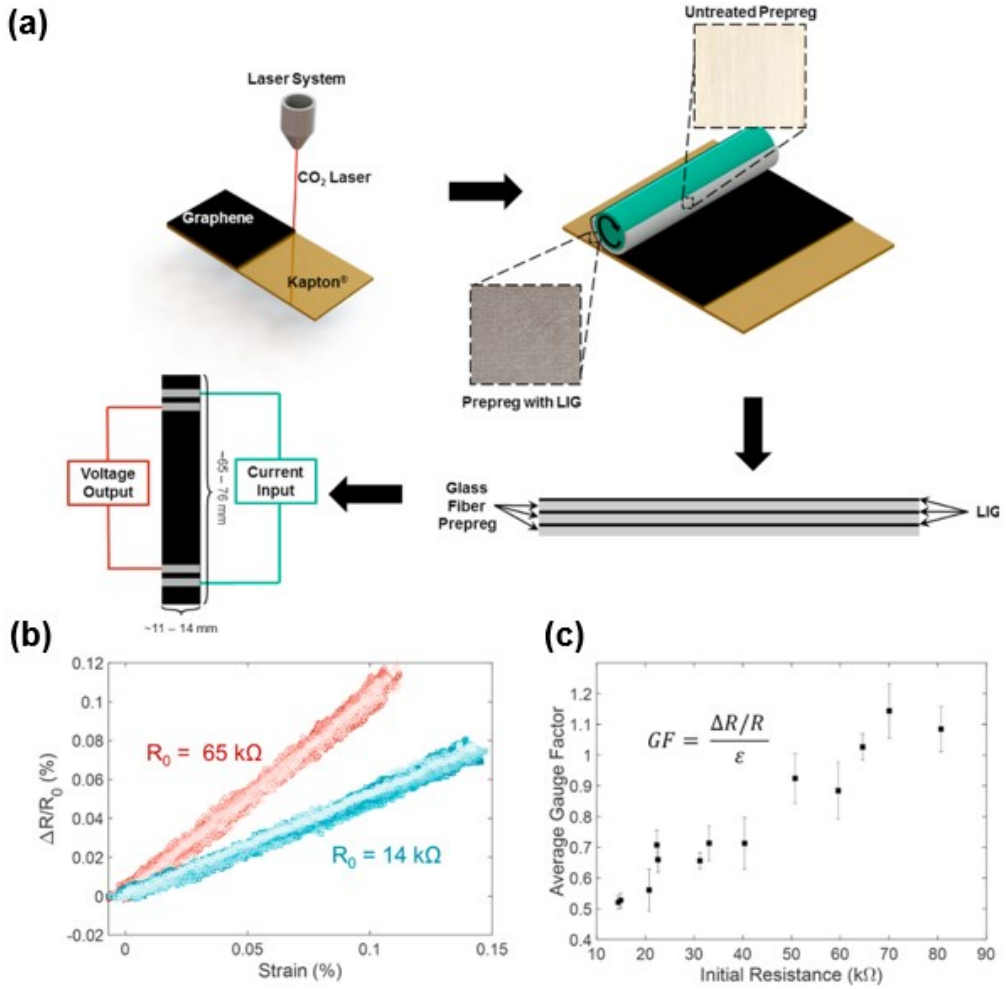

Figure 2.10 (a) Flow diagram for LIG composites production: LIG process on polyimide tape; LIG transfer methods; composite layup and 4 probe silver paste rings wired out. (b) The electromechanical properties of the LIG composites for resistance change versus strain over 20 cycles for two samples. (c) Gauge factor versus initial resistance [57, 61].

Luong et al. explored various forms of LIG composites (LIGCs) by infiltrating the LIG produced from PI film with liquid polymers [56]. This method transferred the LIG structure once the liquid polymer penetrates the porous LIG structure and before it is fully cured as depicted in **Figure 2.10 a**. The researchers successfully transformed the LIG structure to a wide variety of common materials including solid hydrocarbons, elastomers, epoxy, cement, and geopolymer. The special surface roughness of the LIG given the LIGCs enhanced hydrophobicity and antibiotic properties. The LIG-PDMS has been employed to examine the correlation between the strain sensing gauge factor (GF) and the laser pulse density, as shown in **Figure 2.10 b**. Notably, when pulse density increases, the gauge factor exhibits similar pattern until 1000 PPI, at which point both surface conductivity and gauge factor increase. A gain factor of 1000 can be achieved at merely 5% strain in LIGC–PDMS which can be used in flexible electronics.

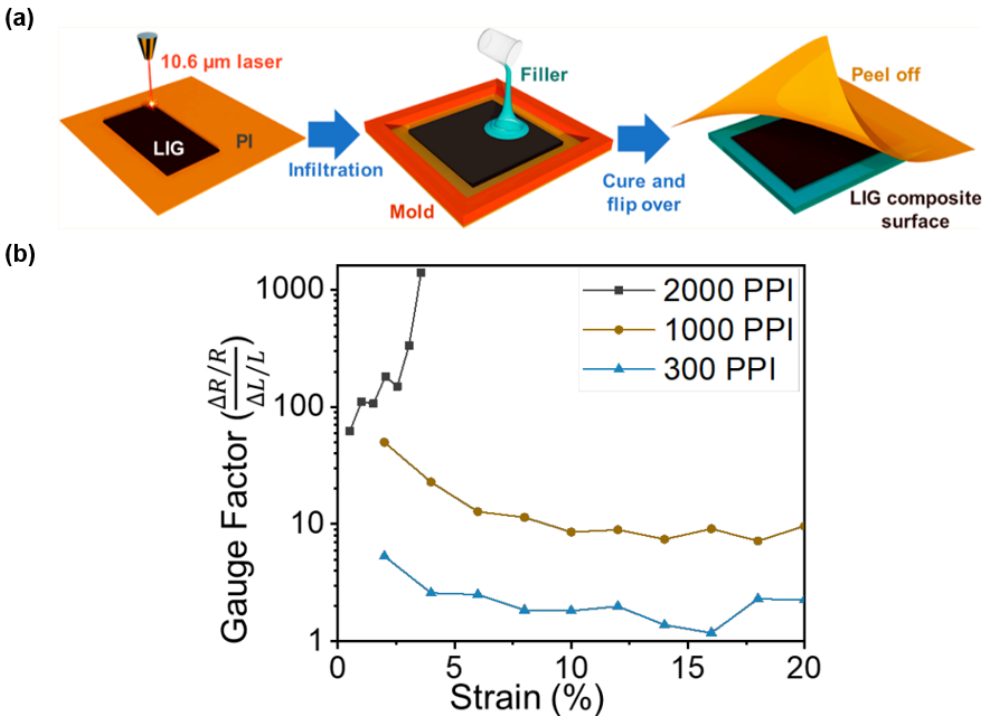

Figure 2.11 (a) The LIG infiltration transfers from PI film to other types of composites after curing. (b) Piezoresitive response of LIGC-PDMS. Gauge factor of LIGC-PDMS made with different laser pulse separation [56].

Despite the fact that transfer printing offers benefits for the composites mechanical strength and solves the key issue of weak LIG adhesion with the PI substrate, this method has limitations and challenges when dealing with complicated or precise patterns. The adhesion between the donor substrate and the transfer layer can result in distortion of the patterns, making large-scale fabrication challenging since any distortion or misalignment during the transfer process could result in discontinuity or the loss of pattern symmetry. Therefore, transfer printing is more suitable for strain and tensile sensing, which requires a relatively simple pattern, than for impact sensing which requires a high-resolution sensing pattern.

Groo et al. also performed a three-point bending test to investigate in-situ strain correlation with electrical resistance for the LIG composites printed from aramid fabric [53]. **Figure 2.12 a and b** show the LIG-coated fabric with different lay-ups in epoxy resin composites. The black lines in the **Figure 2.12 a and b** represent the LIG component layers in the composite laminates. The LIG layers were connected along the thickness direction. In **Figure 2.12a**, greater concentration of LIG was observed above the mid-plane, indicating that this region is subjected to compression. Conversely, in **Figure 2.12b**, more LIG was distributed below the mid-plane which experienced tension. The test sample showed no obvious resistance increase during small deformation when LIG is positioned at the bottom and subjected to up to 1.5 % tensile strain in **Figure 2.12 c**. It was due to the increased carbon-carbon contact between LIG microfibre bundles as a result of transverse compression following the Poisson's effect during bending, which compensated for

the separation of carbon contacts by elongation. During the next 2–5 % strain range, the longitudinal tension in the composite exceeds the transverse compression in the LIG microrods, and the resistance increases due to the extension of the carbon conductive sites. On the other hand, when the LIG is loaded in compression, the electrical resistance decreases within the first 0.2% of compressive strain in **Figure 2.12 d** because the LIG micro rods generate transverse contact between lamina and enhance the carbon-carbon contact path. During the dynamic cyclic loading, single-sided LIG aramid composites demonstrate the ability to detect increasing strain at varying strain rates with gauge factor ranging from 0.6 to 1 up to maximum strain of 0.5%, making them a promising multifunctional material with applications in both dynamic and random load monitoring. The composite matrix component can also be transformed to LIG following laser irradiation. Given that the uncured resin in its liquid phase is incapable of generating a well-defined laser-induced pattern, the partially cured prepreg emerged as a potential solution.

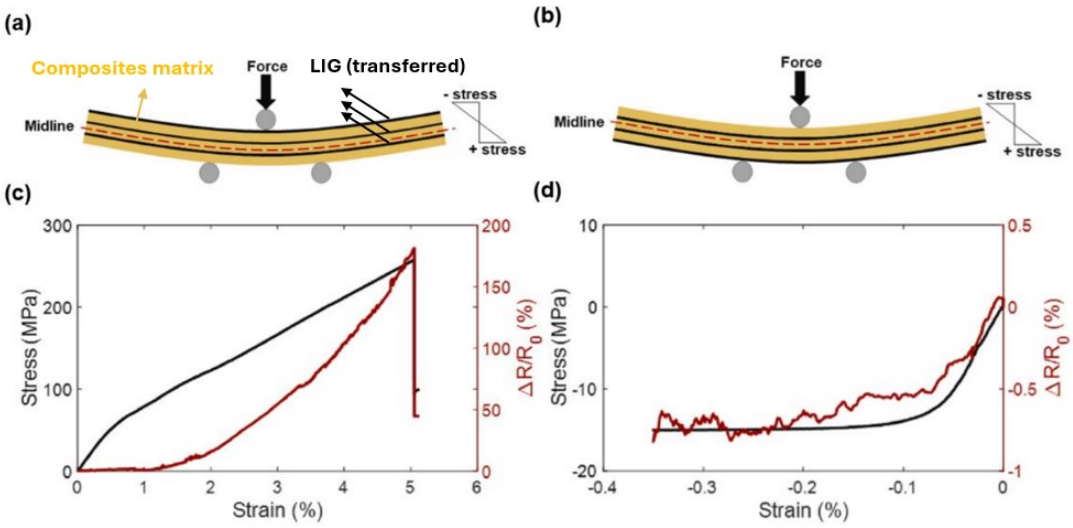

Figure 2.12 Schematic of LIG-coated aramid sample with LIG primarily (a) under compression and (b) under tension. The stress, strain and resistance change relationships of a single-sided LIG aramid sample (c) under tension and (d) under compression [53].

Wang et al. proposed self-converted LIGC-FRP-composites (LIGC) by integrating the laser irradiation process with different curing stage of glass fibre epoxy prepregs [55]. **Figure 2.13 a** depicts the LIGC production process flowchart with the functional graphitized pattern on top or inside of composites. After modifying the laser pass time and laser power, the LIG generated from epoxy prepregs achieved sheet resistance of 0.77kΩ/sq with negligible mechanical degradation (1.58%) in comparison to pristine composites. The LIG strain gauge pattern was encapsulated between two prepregs for tensile test. During the tensile strain sensing (**Figure 2.13 b**), the electrical resistance variations versus strain results demonstrate a high linear correlation up to 2.4% strain. The LIG composites' repeatability was validated through 5 loading-unloading cycles.

In the three-point bending tests (**Figure 2.13 c**), the $\Delta R/R_0$ similarly follows a near-linear increase with mechanical strain, although it exhibits more pronounced signal fluctuations and less distinct peak characteristics. **Figure 2.12 d** illustrates the electrical performance of the LIGC sample under tension-to-failure, where $\Delta R/R_0$ initiates exponential ramping concurrent with a dramatic instantaneous gauge factor (GF) increase beyond the elastic regime.

Overall, within the elastic deformation range (1% strain), the LIGC gauge factors for tensile and bending tests were approximately 1.5 and 2.8, respectively. Exceeding 3% strain results in non-elastic deformation, causing the gauge factor to surge to 6.7, signifying the onset and development of irreversible separation within the LIG network, thereby illustrating LIGC's capacity for self-diagnosis to serve as a warning sign before catastrophic structural failures. The sheet resistance of the LIGC (around 1kΩ/sq) is higher compared to that of LIG generated from PI film. (50 Ω/sq) The authors explained that it is due to the chemical structure of the prepreg, which consists of approximately 50% bisphenol-A epoxy, 30% phenolic epoxy, and 20% diglycidyl hexanediol (resin diluent). Having fewer aromatic repeating units compared to the PI precursor limit the production of high-quality graphene and introduces more insulating components, such as molten glass and other residual organic fragments which become the impurities of graphitic components after laser.

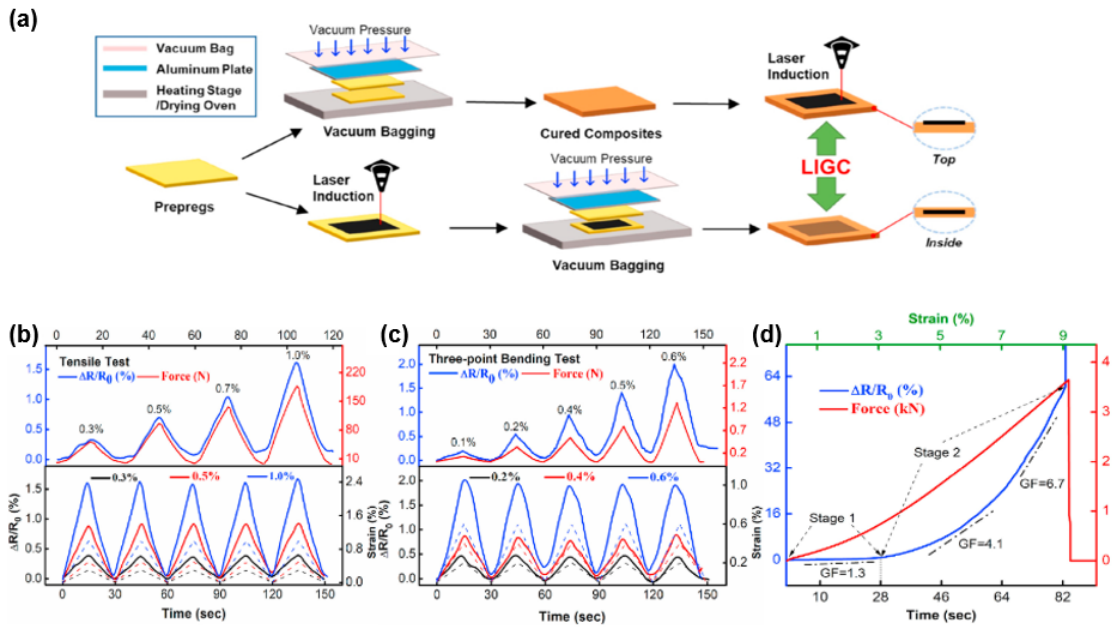

Figure 2.13 (a) Schematic diagram of LIGC manufacturing with the functional graphitized pattern on top or inside the glass fibre prepregs. (b) Electromechanical sensing of LIGC under cyclic (b) tensile and (c) three-point-bending tests. (d) Sensing behaviour of LIGC during a tension-to-failure test [55].

Table 2.2 summarizes the previous works of LIG composites for strain sensing fabricated using different substrates. The appropriate laser parameters, such as power density and number of

scans, are determined by the specific organic substrate. The quality of the resulting LIG varies, as shown by the electrical resistivity and sheet resistance, which range from 10 Ω/sq to 104 Ω/sq. The gauge factor, which measures the sensitivity of LIG composites, varies significantly from a minimum of 0.38 to a maximum of 20000 The gauge factor can vary with applied strain, which differ significantly from the behaviour observed in conventional metal strain gauges. The fragile LIG nanostructure skeleton can develop irreversible discontinuities in its conductive pathways under applied strain. This phenomenon results in unique electromechanical (piezoresistivity) characteristics which are not well understood and worth investigating.

Table 2.2 Summary of LIG composites and their sensing performances.

Substrate	Transferred matrix or protection	Sheet resistance (Ω /sq)	Strain range (Tensile)	Gauge factor (Tensile)	Gauge factor (Bending)	Ref. No.
Filter paper with fire retardant	NA	32 -120	1.67%		NA	[62]
PI film	NA	15.9-46.1	1.5%	4.9- 112	NA	[44]
PI film	NA	12000	1%	19- 40	NA	[51]
Aramid fibre	NA	20-130	4%	21.4- 27	NA	[50]
Based on PEEK and coated with PDMS/hexane solution	NA	5.39	5%	32.6 - 155.36	51.08- 212.35	[63]
Epoxy prepregs (TXG30-290-38T)	NA	740	1%	1.3- 6.7	NA	[55]
Kapton PI tape	E-glass epoxy prepreg	14k - 65k strain gauge	0.1%	0.5-1.2	NA	[57]
Kapton PI tape	silicone rubber	815.4 after transfer	31.8%	37.8	NA	[58]
Kapton PI tape attached to PET sheet	PDMS	60	5%-100%	50 - 20000	NA	[48]
PI film	medical grade polyurethane (MPU)	100 - 800	30%	70- 200	NA	[64]
Kapton PI tape	E-glass epoxy prepreg	300-1000	0.25%	0.38	NA	[61]
Plain-weave Kevlar fabric	Infused in epoxy resin	10-100	0.15%	1	NA	[53]

PI film with super substrate ZnSe	NA	60- 36000	NA	NA	0.7(compression)- 1.3 (tension)	[59]
PI particles added in PDMS	NA	300	15%	30	NA	[65]
PI film	Ecoflex prepolymer	58	6%	1.68	NA	[66]

2.4.2.3 External environmental sensing

Composite structures can be exposed to external weather or environmental factors such as corrosive gases, hazardous solvents and moisture which can significantly affect their structural integrity and functionality. For instance, the water ingress can lead to matrix plasticization, swelling, and interfacial degradation, compromising the load-bearing capabilities and service life of composite structures. Therefore, integration of simple environmental sensors into composite structures allows continuous monitoring of the internal condition or external environment, facilitating prompt maintenance and repair.
Previous research reveals that graphene exhibits rapid reaction in electrical conductivity when subjected to external stimuli, including fluctuations in humidity [67], chemicals [68] , and variations in atmospheric gases and pH levels [69]. Vivaldi et al. provide a comprehensive summary of the fabrication of three-dimensional (3D) LIG from PI films using multiple laser scans for chemical and biosensing [68]. Their findings indicate that compared to bare LIG sensors which demonstrate effective performance in detecting small- and medium-sized analytes through voltammetric methods, functionalization enhances the sensor's selectivity and sensitivity. For example, LIG sensors modified with spray-coated PEDOT polymer and electrodeposited silver nanoparticles achieved detection limits of approximately 0.33 μM for amoxicillin and ascorbic acid across a broad pH range (pH: 4–10).

Kulyk et al. created the LIG-based humidity sensor using cellulose paper with fire retardant [67]. The fabrication involved a single-step pulsed UV laser (355 nm) irradiation of common filter paper, converting cellulose fibres into a conductive LIG network. The paper-based LIG sensors are designed in a rectangular bar pattern (6 × 20 mm^2, **Figure 2.14 a**) and placed inside a climatic chamber maintained at 20 °C, where relative humidity (RH) was systematically varied in 10% increments from 10% to 90%, with additional steps at 95% and 98% RH, and then continuous descending back to 10%. Each step lasted approximately one hour to allow sufficient interaction time with the water molecules. The researchers observed a ladder-type resistance rise across the 20-80% RH range as shown in **Figure 2.14 b**, achieving a sensitivity of up to 1.3 × 10^{-3}%/ RH. The

humidity sensing mechanism was explained using the framework of the variable range hopping electrical conductivity model. They suggested that the sensor's response is primarily governed by water intercalation within the interlayer spacing, with an additional contribution from charge hopping along the graphene plane, which is enhanced at higher humidity levels. Notably, the resistance values during the descending phase of the measurement exhibited greater fluctuations compared to the ascending phase. This behaviour is attributed to water desorption, where residual water molecules are retained within the sensor after prolonged exposure to high humidity, giving a large residual electrical resistance and hindrance to the flow of electrical charge.

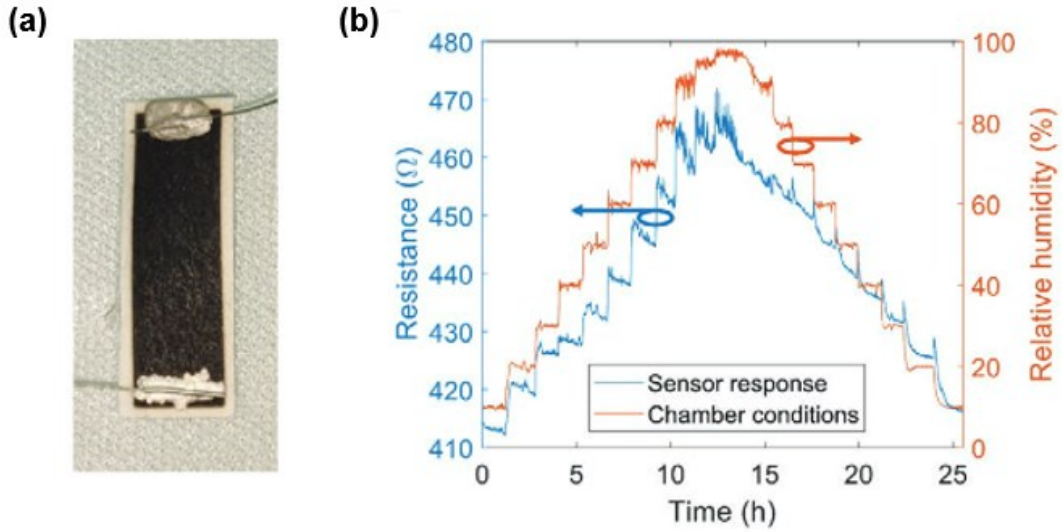

Figure 2.14 (a) Optical image of a paper-LIG humidity sensor. (b) Resistance of the paper-LIG humidity sensor in response to different relative humidity as measured by the climatic chamber's capacitive sensor [67].

Wang et al. recorded the resistance sensing response of LIG sensor fabricated from polyimide PI paper when exposed to organic solvents through full immersion [70]. The LIG was produced using a low laser power range of 0.875 W to 1.75 W, with a scanning speed of 2 inches per second, resulting in the formation of a uniform porous LIG network at sub-micron levels. They conducted dripping tests, where a square LIG pattern measuring 1 cm × 1 cm was positioned beneath acetone droplets, with micro-volumes ranging from 1.5 to 7.5 µL dispensed onto the central region of the LIG pattern using a micropipette. In the submersion tests, a U-shaped LIG pattern was employed to prevent the silver electrodes from being wetted or disrupted by the testing fluid. The sensors were fully immersed until their resistance stabilized for at least 30 seconds. **Figure 2.15 a** and **b** illustrate the relative resistance changes for LIG sensors produced at different laser powers, revealing that the sensor synthesised at 0.875 W power exhibited the highest sensitivity and fastest response time. In **Figure 2.15 c**, the optimal LIG sample produced at 0.875 W was

further evaluated for long-term chemical sensing performance. The results demonstrated high reproducibility across multiple immersion-drying cycles in acetone, showing a consistent maximum resistance change of 17.5% ± 0.16% and full recovery (>99%), confirming the exceptional reliability and durability of the LIG sensors for acetone detection.

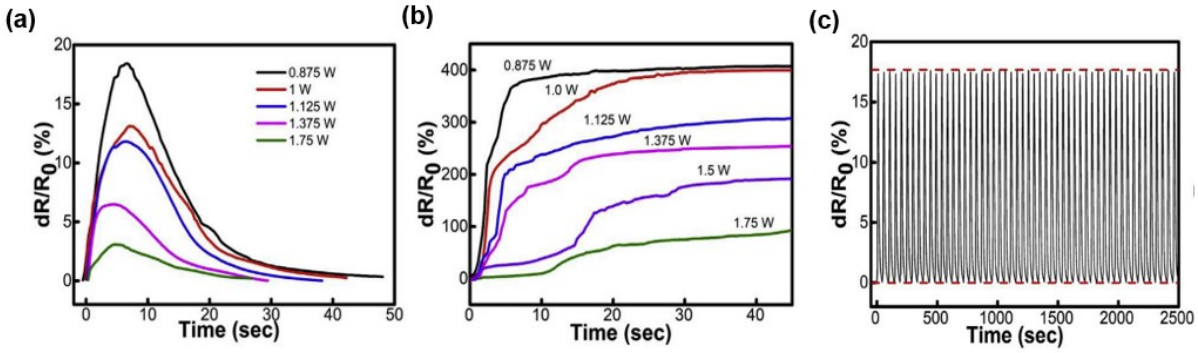

Figure 2.15 Real-time resistance changes of various laser-processed LIGP sensors subjected to (a) 4 mL acetone dripping and (b) full submergence. (c) The resistance changes of 0.875W LIG sample under 50 immersion-drying cycles of 4 mL dripping acetone droplet [70].

Houeix et al. used a natural cork sheet to create a sustainable resistive humidity transducer [71]. LIG was synthesized on an agglomerated cork sheet using a 532 nm green laser, without prior treatment. This differs from the equipment employed in the current PhD project, which utilizes a blue laser system and will be comprehensively detailed in Chapter 3. The porous LIG structure was achieved under optimal laser parameters of 0.5 W power and a scanning speed of 5 mm/s. The resultant LIG exhibited excellent electrical conductivity, with a sheet resistance as low as 31 Ω/sq. SEM microscopy revealed that the cork's original vegetal hexagonal structure was transformed into a more heterogeneous black foam. The LIG-based transducers demonstrated high sensitivity and minimal temperature dependence over long-term operation. A proof-of-concept transducer fabricated on a cork stopper is presented in **Figure 2.16 a**, while the dynamic response is detailed in **Figure 2.16 b** and **2.16 c**. The resistance exhibited a stepwise increase in response to gradually increased RH; however, hysteresis was observed, with the greatest deviation occurring at 40% RH. After being placed at high humidity levels, the subsequent RH reduction phase showed fluctuations and irregular behaviour, likely due to the physical change of the cork materials. This study highlights the high reliability of cork-LIG transducers within the 40–80% RH range, demonstrating the feasibility of LIG in environmental monitoring applications, particularly in storage conditions with gradual humidity variations. The optimal lasing parameters depend on the type of substrate and laser source, which requires further investigation. In our study, we employ a different laser source (blue light laser) compared to this reference, the optimal laser parameters will consequently differ.

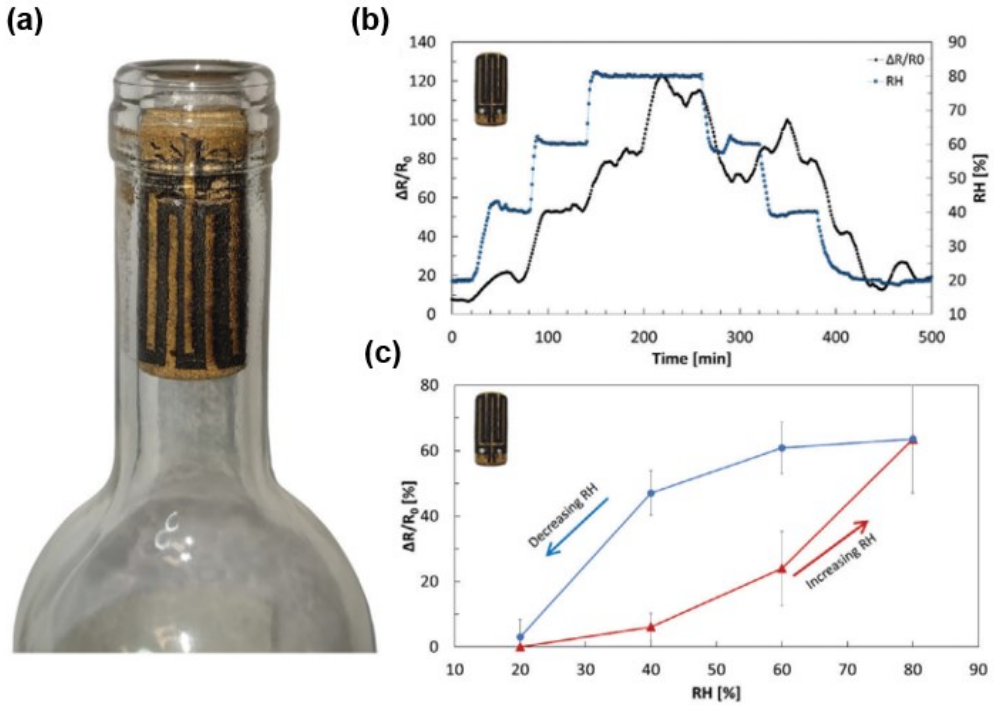

Figure 2.16 (a)The optical image of Cork-LIG-stopper RH sensor on a bottle of wine. (b) Dynamic variation of the transducer over RH increasing and decreasing cycle. (c) Static response and hysteresis over RH variation [71].

2.5 Conclusion for literature review

This section explores the recent research on graphene-based self-sensing composites and LIG-based self-sensing composites. In comparison to conventional graphene generation and dispersion methods, laser irradiation significantly simplifies the manufacturing process and reduces equipment and fabrication costs. Although the graphene quality of LIG is not as good as that produced using conventional processes, the LIG sensors still show outstanding potential in their sensing capability. The majority of previous research predominantly focused on utilizing LIG composites for applications such as strain sensing or damage detection. However, research gaps can be identified in the following fields:

- *Integration of LIG sensors into composites*

- *Size and geometric effects on sensing performance*.

- *Theoretical modelling of LIG piezoresistivity*.

This PhD project aims to address these gaps by investigating the fabrication of LIG-based sensors and their integration within composite structures for diverse sensing applications based on simple electrical resistance measurements. The ultimate goal is that the works carried out in this project can provide a better understanding of LIG's role in self-sensing composite materials and

also pave the foundation of optimal design of LIG sensors tailorable for real-world SHM applications.

Chapter 3 Cork-derived LIG for impact damage sensing

This chapter describes the sensing performance of LIG sensors for impact damage when embedded in a composite sandwich structure. The properties of LIG on a cork substrate after irradiation by a commercial blue laser engraver were firstly characterised to assess its viability as a sensing element. The morphology, graphitization quality, and electrical properties of the synthesised LIGs were then investigated to find the lasing parameters that offer a good balance between graphitization quality and LIG geometry. Subsequently, its damage sensing capability was demonstrated in a drop weight impact test for internal damage detection and damage area estimation, validated against the results from X-ray computed tomography.

3.1 Introduction

Interlaminar delamination and internal fibre breakage due to impact loading in a laminated composite structure can lead to catastrophic failure Cork is available commercially in the form of thick sheets (more than 1 mm thick), making them suitable to be the core material for a composite sandwich structure [9]. Detecting damage caused by low-velocity impacts is particularly challenging because such damage is often not visible to the naked eye from the exterior. This type of damage is commonly referred to as Barely Visible Impact Damage (BVID) and typically requires non-destructive testing for detection. To detect internal damage effectively, it is practical to integrate sensing devices within the composite structure itself. When multiple of these embedded sensors are arranged in an appropriate pattern, they can not only detect the depth of impact damage but also the size of damaged area. For a large coverage area, it means the graphene-based sensors need to be designed and processed on a large scale. LIG can provide the solution as it can be synthesised simply using a 2D laser engraver regardless of the area size under the ambient conditions at a low cost. The literature review in Chapter 2shows that the most common precursor substrate for the manufacturing of LIG is polyimide (PI) film, which has a high level of optical transparency in the infrared laser wavelength range. However, PI films undergo significant thermal deformation during laser irradiation and exhibit poor compatibility with the resin matrix of polymeric composites due to their smooth surface. Therefore, alternative precursor substrates with higher compatibility need to be explored.

Recent research has demonstrated that the majority of biodegradable carbon-based precursors can be transformed into amorphous carbon and then to graphene using multiple lasing methods, offering a sustainable and eco-friendly way to synthesise LIG [72]. In this work, cork was identified as one of the potential substrate candidates of LIG, as it offers a few advantages. It is lightweight and commercially available in the form of thick sheet (more than 1 mm thick), making

it a suitable choice as the core material of the composite sandwich structure studied in this chapter. Considering the hardware constraints of producing LIG using a low-cost commercial laser printer with relatively slow processing speeds, substrates with higher thermal conductivity and greater resistance to deformation are preferred. Due to its thick and porous nature which assists thermal energy dissipation, cork paper exhibits less thermal distortion during laser irradiation [73]. Consequently, cork substrates have been successfully used to produce graphene structures, as demonstrated in prior research with different applications [71, 74]. Additionally, cork enables the fabrication of complex LIG patterns, facilitating damage detection over large surface. The cork's porous structure also permits infiltration and wetting by the resin, allowing it to form an integral part of the composite sandwich structure after the resin is cured.

The following presents a new approach for using the cork-derived LIG as a damage sensor in a fibre-reinforced composite sandwich structure. The properties of LIG on a cork substrate after irradiation by a commercial blue laser engraver are firstly characterised to assess its viability as a sensing element following selected lasing parameters. The morphology, graphitisation quality and electrical properties of the synthesised LIGs were then investigated to find the lasing parameters that offer a good balance between graphitisation quality and LIG geometry. Subsequently, the LIG on cork substrate was embedded into a glass fibre-reinforced epoxy composite to demonstrate its damage sensing capability in a drop weight impact test for internal damage detection and damage area estimation.

3.2 Experiments

3.2.1 Laser engraving system

The laser diode system used was a commercial laser engraver unit (GKTOOLS All Metal Mini CNC Laser Engraver Cutter Engraving Machine). **Figure 3.1** shows the set-up of the laser engraver, as well as its corresponding dimensions. It came with the FB03 laser head diode which has a maximum power of 2500 mW and emits a blue laser beam of wavelength 445 nm. The CNC laser machine's positioning accuracy of ±0.2 mm imposes a limitation on line density, restricting reliable printing to patterns with fewer than 5 lines per millimeter. The laser head has an adjustable power range from 0 to 100% and works under DC voltage 12 V. The communication between the laser engraver and the PC was done via the LaserGRBL v4.8.0 control software (open source). The maximum engraving area was 45×45 cm. The adjustable laser focus was set at the minimum diameter of the laser spot about 0.2 mm.

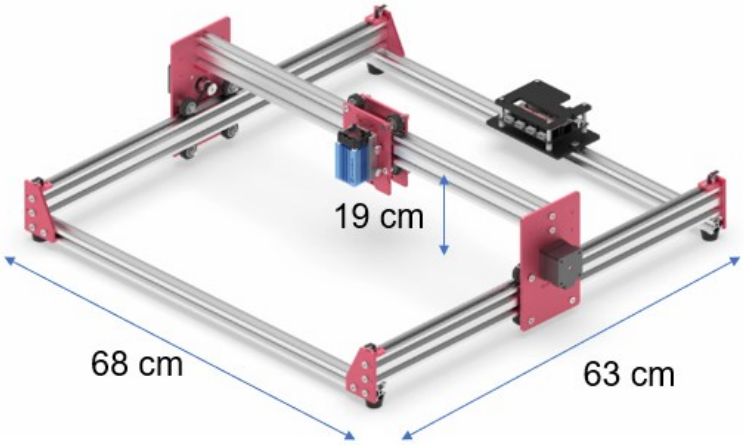

Figure 3.1 The laser engraving system used for LIG synthesis on cork substrate.

3.2.2 Sythesis of LIG on cork paper

Cork paper (BENECREAT, 1 mm thick) was taped to a wooden board during laser treatment. Before the laser treatment, the cork paper was wiped with isopropyl alcohol (IPA) and dried at room temperature. The laser irradiation on the cork paper was done following the horizontal line-by-line tracing approach for all patterns used in the characterization and sensing test, as depicted in **Figure 3.2 a.** To limit the number of parameters, the laser focal distance, scanning speed and pattern resolution were fixed at 19.5 cm, 16.7 mm/s, and 300 dot per inch (dpi) respectively based on the recommended setting imposed by the hardware constraints. The line density of the scanning was set at 2 lines/mm to avoid irreversible thermal deformation and burnt marks on the substrate after multiple scans. In this study, the variables for LIG generation that required optimization were reduced to two, i.e. laser power and number of laser scans, which are easy to manipulate using the control software. For convenience, the LIG samples prepared on cork paper were named based on the processing parameters, that is, scanning time (1 to 3 times) and power (0.63 W, 1.25 W, 1.88 W and 2.50 W, which is 25%, 50%, 75% and 100% power respectively). For example, LIG-2T-1.88 refers to LIG fabricated with 2 times scanning and 1.88 W power.

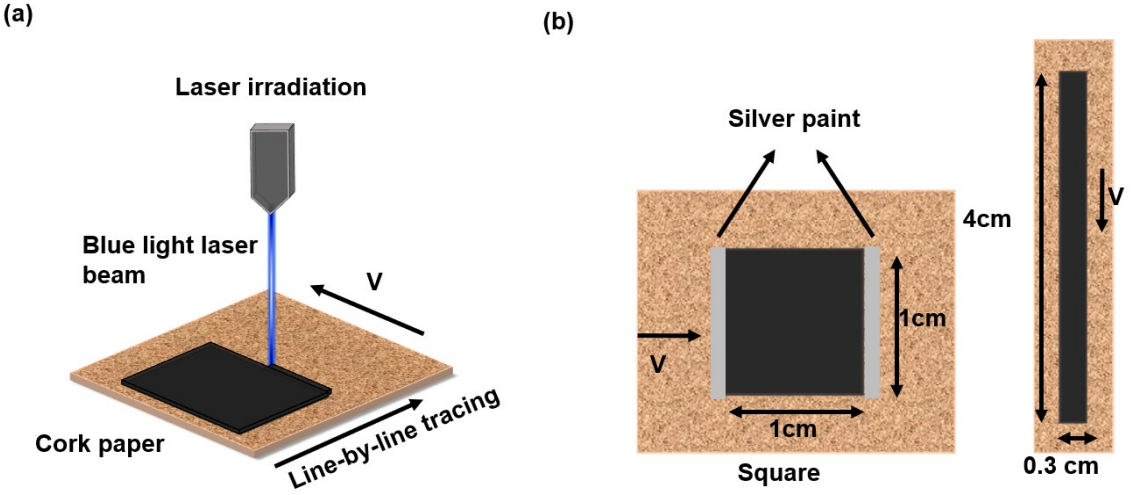

Figure 3.2 The LIG structure on cork paper substrate. (a) Schematic depiction of the laser irradiation on a cork paper substrate, where the morphology and quality can be systematically designed by the laser power *P*, scanning speed *v*, and lasing pass number *n*. (b) Schematic top view of the sheet resistance measurement and LIG characterisation.

3.2.3 LIG morphology, structure, and electrical properties characterization

The electrical properties of the LIG are closely related to its morphology and graphization quality as a result of the lasing parameters. As illustrated in **Figure 3.2 b**, two LIG patterns were created on cork paper for characterisation. The square-shaped (1 cm× 1 cm) LIG patterns were lased for sheet resistance measurement, while the rectangular (40 mm× 3 mm) LIG patterns were for microstructural characterisation. All laser treatments were processed under normal room conditions. Silver conductive paste was applied on the opposite edges of the square-shaped LIG pattern to facilitate copper foils connection for resistance measurement. The surface and cross-section morphology of LIG were investigated via field emission scanning electron microscopy (SEM, HITACHI SU8000). Horiba Xpolora Plus Raman microscope was employed with a 532 nm excitation laser at the power of 5 mW to measure the constituent components and carbonization level of the LIG. A 3D laser scanning confocal microscope (Alicona G4 Infinite Focus) was used to characterise the geometry of the LIG lines. The surface resistance of the LIG electrodes was determined by a handheld digital multimeter (Fluke 175).

3.2.4 Fabrication of cork-LIG damage-sensing composites

Following the characterisation work in Section 3.2.3, the laser parameter setting which gives the optimal LIG properties was used to produce LIG mesh patterns before they were embedded as the sensing layer in the glass fibre-reinforced epoxy composite plates. The 10 cm ×10 cm mesh pattern consisted of 9 horizontal and 9 vertical 1.5 mm width LIG channels with the dimensions as shown in **Figure 3.3 a**. The design of the mesh pattern featured a higher mesh density in the central region, where larger deformation and damage are expected to happen during impact tests, while a lower mesh density at the edges to prevent cluttering the pattern with too many channels. The terminals of each channel were connected to 0.1 mm thick copper strips for electrical resistance measurement. An image of the LIG synthesised after laser irradiation on the cork substrate is shown in **Figure 3.3 b**. As shown in **Figure 3.3 c**, the cork paper with the LIG mesh pattern was then directly placed as the core material between two face sheets each consisting of 6 plies of S-913 unidirectional glass fibre/epoxy prepreg (HexPly, United States) arranged in a cross-ply [0°/90°] configuration. The complete lay-ups were then vacuum bagged and cured in the autoclave at 120°C and 7 bar for 60 minutes following the prepreg manufacturer's recommendation. The autoclave used in this experiment is shown in **Figure 3.3**

e. During the curing process, the excess resin was allowed to flow and infiltrate into the porous cork paper substrate, bonding the cork paper to the glass fibre composite face sheets, **Figure 3.3 d** and **3.3 f** display the composite lay-up before and after the curing process. A total of nine plates of the LIG self-sensing composites, each measuring 14 cm × 14 cm, were manufactured for the drop weight impact test. Prior to impact testing, visual inspection confirmed no delamination or debonding between composite laminates, and electrical resistance measurements verified the integrity of all channel connections from the extended copper strips. The central region of the plate which designated as the impact test area remained fully integrated.

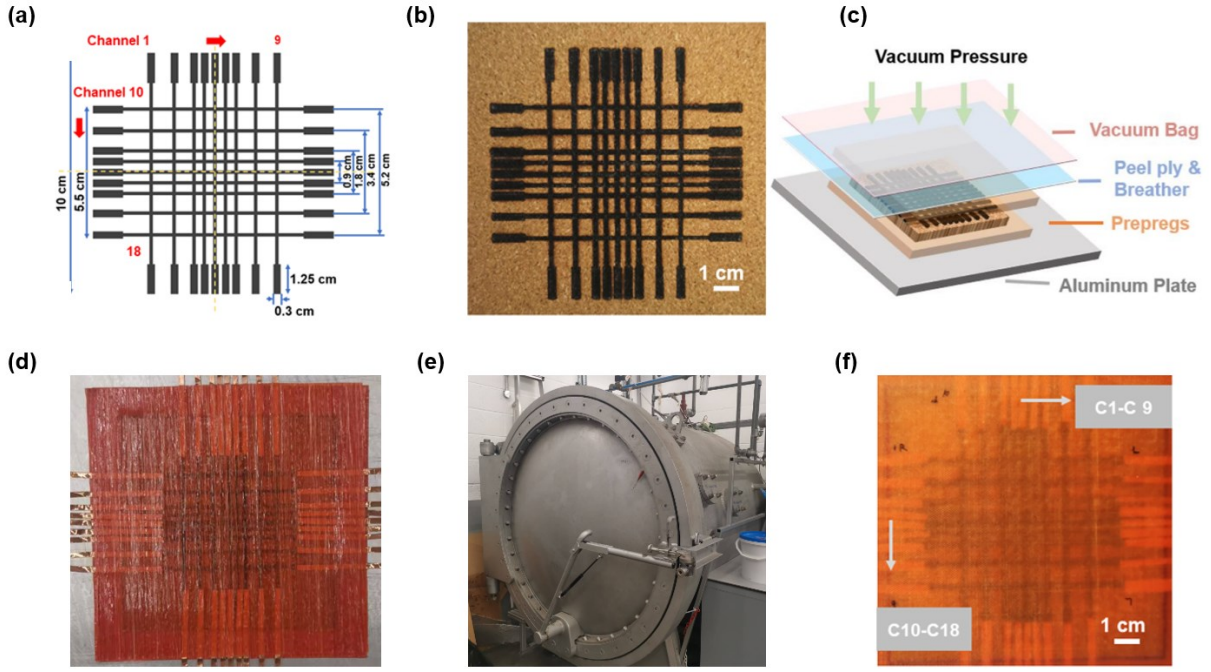

Figure 3.3 (a) The LIG mesh pattern design with 18 channels. (b) The cork paper with the LIG mesh pattern embedded between two glass fibre composite face sheets in a vacuum bag. (c) The cork-LIG mesh before embedded in the composite plate. (d) The cork-LIG layer inserts between uncured glass fibre prepregs. (e) The autoclave for composites prepreg plates curing. (f) Composite plate with embedded LIG mesh before impact damage.

3.2.5 Drop weight impact test of LIG damage-sensing composites

The impact energy applied on the nine composite plate specimens as described in Section 3.2.4 was generated by a drop tower impact system (CEAST 9350, Instron) as shown in **Figure 3.4 a** using a standard hemispherical indenter (16mm diameter). Six of the plates were used for providing training data to machine learning model (more in Section 3.3.3) and the remaining three plates for model validation purposes. All composite plates were placed on a support plate with a central 40 mm diameter hole. To evaluate the sensing capability of the multichannel LIG mesh design, the plates were impacted at a different location having different LIG channel densities. The impact energy of 10 J was applied on the six training plates, while 10 J, 12 J, and 15 J were

applied on the three validation plates. This could give a good variety of test data covering different loading scenarios.

The working concept of embedding a LIG layer to locate the damage affect area in composite materials is inspired by previous graphene-based sensor designs [75]. In this study, the epoxy resin fills up the LIG pores and offers mechanical support to the otherwise fragile LIG microstructure, at the same time stablising its electrical properties. In the impact test, damage such as interlaminar delamination takes place at the interface between the cork core layer and the composite face sheet. Damage in the form of crack opening and graphene pull-out perturbs the LIG microstructure, hence increasing the electrical resistance. Knowing the number of damaged channels and their spacing in the horizontal and vertical directions, similar to x- and y-coordinates in a Cartesian coordinate system, one can uniquely determine the position of the impact damage and the damage size. The resolution of the predicted damage size is given by the separation of the LIG channels.

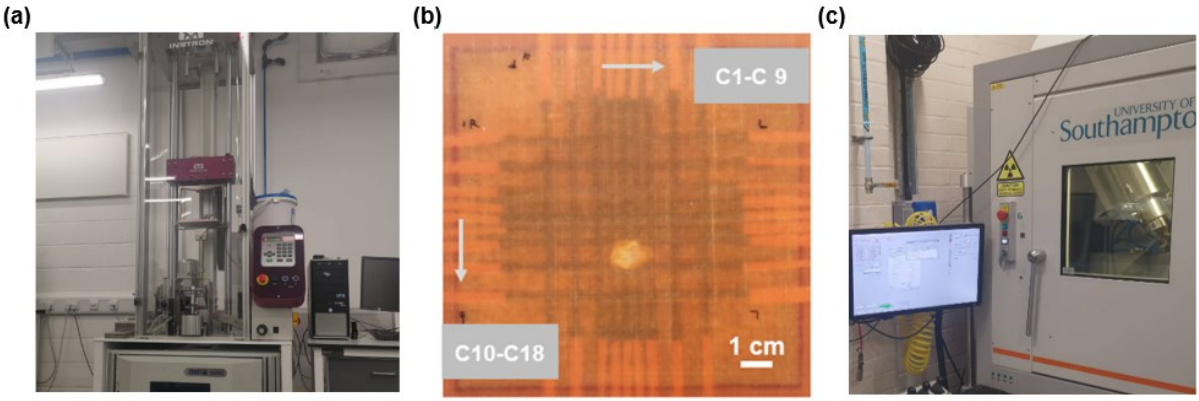

Figure 3.4 The impact damage test set-up and analysis equipment. (a) The drop impact testing tower. (b) Discoloration of the composite plate with embedded LIG mesh showing damage after impact. (c) The Nikon XTEK 225 kVp CT system within the safety chamber.

Due to the heterogeneous composition of the cork paper substrate as a natural material, the cork-derived LIG has electrical resistances varying slightly from plate to plate. This should not affect its damage sensing performance as the main monitoring parameter was the change in electrical resistance. The electrical resistance of each LIG channel was recorded before and 10 minutes after the impact test to allow for the LIG internal structure to recover and stabilize. All readings were measured three times to calculate the mean and standard deviation. **Figure 3.4 b** shows composite specimens with post-impact damage, illustrating the extent of damage in the composites, which will be analyzed further in the results section. In order to validate the damage sensing performance of the LIG channels, the internal damage of the composites was evaluated using a Nikon XTEK 225 kVp micro-focus X-ray computed tomography (CT) system as shown in

Figure 3.4 c. The CT images were reconstructed by the VGSTUDIO 2022 software with a voxel size of 75 µm/pixel for the x- and y-axes, and 50 µm/pixel for the z-axis.

3.3 Results and discussion

3.3.1 Characterisation results of Cork-derived LIG

In order to determine the optimal laser parameters, the characterisation results of LIG including its microstructure, graphitization level and area electrical conductivity are discussed in this section.

3.3.1.1 Microscopy

The basic microscopic analysis is essential to ensure the creation of a LIG pattern with uniform quality. Minimizing the gap between adjacent laser scanning paths was the first step to achieving a continuous LIG surface, which is necessary for developing consistent electrical conductivity and reliable sensing capabilities.

The profile analysis of a single LIG line pass on a cork substrate, including its shape and width were carried out. Previous study has shown that using a lower laser energy with multiple time lasing generates higher quality graphene because of the conversion from amorphous carbon to structurally ordered graphite or graphene[76]. The LIG single lines from 1 to 3 lasing passes at different laser power are depicted in the micrographs in **Figure 3.5**. The line width of LIG (between the red dots lines) was found to gradually grow with rising laser irradiation power, i.e., the ignition vaporized particle deposition area expands with increased number of lasing passes. In **Figures 3.5 a** and **3.5 b**, the first laser scan produced a relatively uniform carbonized region, while subsequent scans increased the line widths. However, at 75% laser energy (**Figure 3.5 c**), the first scan generates a carbonized zone with two distinct grey shades: a darker central region (indicating higher carbonization) and lighter edges (lower carbonization). This occurs because the Gaussian-distributed laser beam concentrates most energy at the centre, achieving significant carbonization in a single pass. In contrast, at the lower power of 1.25 W, high carbonization only emerges after the second pass. At the maximum power (2.50 W, **Figure 3.5 d**), excessive heat causes substrate burning, obscuring the dark/light grey contrast. This effect worsens with additional passes, where the second scan produced bulging uneven light-grey regions (second subpicture in **Figure 3.5 d**). The misalignment of LIG lines, resulting from substrate deformation, adversely affects the carbonization process and consequently compromises subsequent sensing performance investigations.

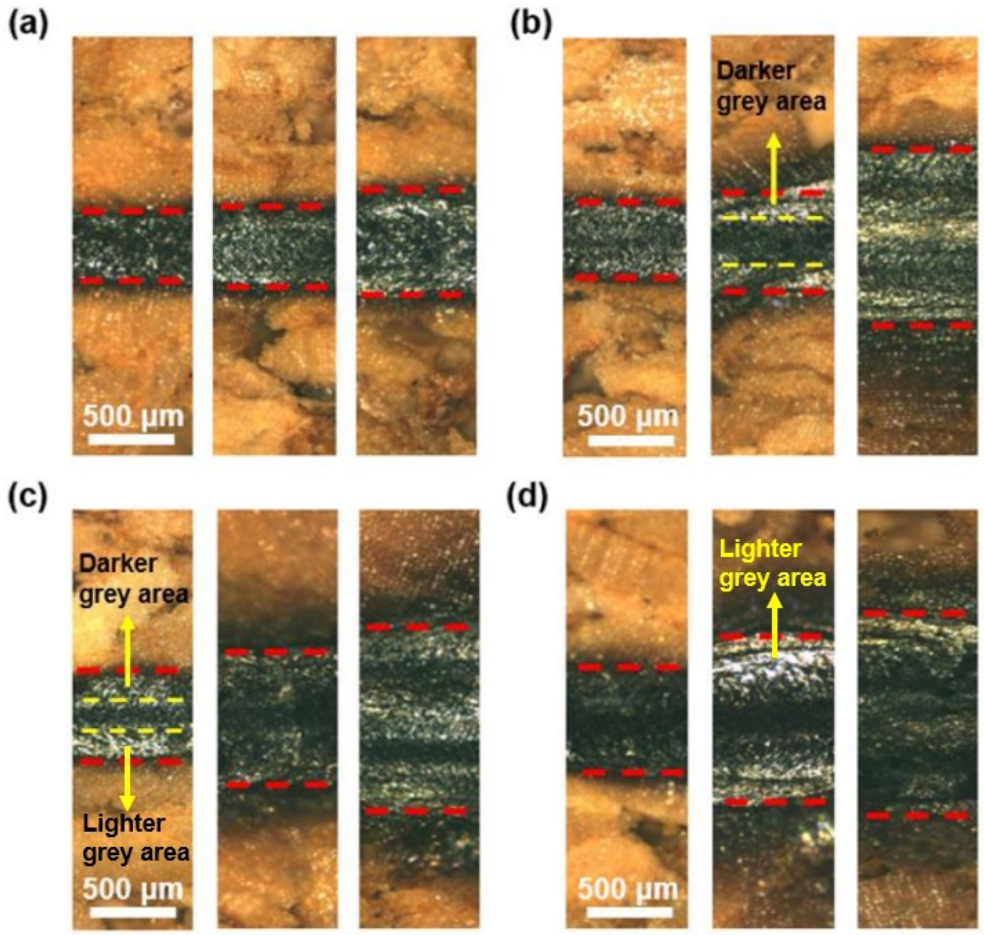

Figure 3.5 Surface morphology of the single line pattern after one to three laser scans. Th red dot lines showed the boundary of the laser-irradiated region. (a) Microscope image of cork irradiated with 0.63W laser power (1 to 3 times from left to right line width: 380 μm,440 μm, 560 μm). (b) with 1.25W laser power, line width (470 μm, 510 μm, 980 μm). (c) with 1.88W laser power, line width (490 μm,740 μm,1080 μm). (d) with 2.50W laser power, line width (590 μm, 960 μm,1150 μm).

The resolution of the laser scan stage (defined as the minimum incremental movement of the laser CNC arm around ±0.2 mm) during the second scan could contribute to line widening in LIG fabrication. Partial alignment during repeated scans can result in partial overlap of laser spots, leading to localized broadening of the LIG conductive lines. However, the system-induced errors can be mitigated by printing multiple parallel LIG lines and analyzing their average width. The cross-sectional SEM analysis below in **Figure 3.7** revealed concave profiles with minimal skewness, while width measurements showed strong agreement with optical microscopy measurements. These observations together confirm that the second laser scanning pass introduced no significant misalignment effects.

3.3.1.2 Scanning Electron Microscopy

Figure 3.6 a-d show the SEM images of the cork-LIG microstructure from the top view produced using different number of lasing passes and power. **Figure 3.6 a** illustrates the transformation of the regular cell structure of the cork into a more irregular porous structure of LIG in the LIG-1T-1.25W sample, which is attributed to the gas release. The cork area that stays intact between the LIG is bounded within the two yellow dashed lines in the images. The two-pass lasing at the lower 1.25 W power manages to close the LIG line gap further, as shown in **Figure 3.6 c**. By increasing the laser power to 1.88 W, in **Figure 3.6 b**, the width of the single-pass LIG lines increases with decreasing gap between them, but not sufficient to close the gap fully. Lastly, having two-pass lasing at the higher 1.88 W power in **Figure 3.6 d** successfully transformed all cork to porous LIG structures without any visible cork remaining, resulting in the formation of fully interconnected LIG lines.

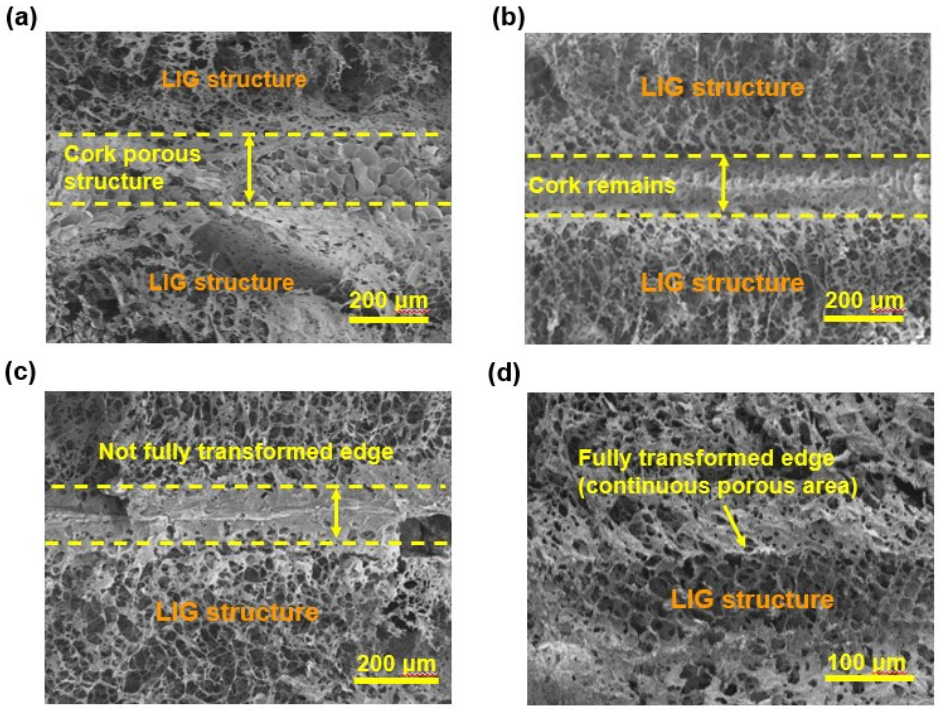

Figure 3.6 SEM images of LIG microstructure (viewed from top). The SEM images of (a)sample LIG-1T-1.25. (b) Sample LIG-1T-1.88 (c) Sample LIG-2T-1.25. (d) Sample LIG-2T-1.88.

To develop the correlation between LIG morphology and the laser parameters at the irradiation area, it is necessary to quantify the irradiation energy encompassing all the lasing parameters. The dynamical fluence energy F (J/mm^2), which estimates the energy injected into the scanning path encased by the laser spot, can be calculated as follows:

$$F = \frac{nP}{vs} \qquad \text{Equation 3.1}$$

which is a function of laser power P, number of scanning pass *n*, scanning speed *v*, and laser spot radius *s*. The cross-section profile of each LIG line under different dynamical fluence energy is shown in the SEM images in **Figure 3.7** and can be well represented by a Gaussian distribution. For F = 0.75 J/mm^2 (**Figure 3.7 a**), the carbonization area shows a concave curve with the lowest depth. With increasing F values, the carbonised cross-section curve displays a sharper edge, and the overall depth of penetration increases substantially (**Figure 3.7 b – d**). Fifteen representative points on each cross-sectional profile were used and fitted with a Gaussian distribution (the yellow curves in the figure), enabling the calculation of geometrical parameters such as line width w, depth D, and arc tilt angle θ (at half D_{max}) (**Figure 3.7 e**). The results confirm that the carbonised LIG profile conforms with the Gaussian irradiance profile of the laser beam. The cross-sectional images demonstrate how irradiation energy (F) relates to the LIG line profile. By adjusting laser parameters, it is possible to increase both depth D_{max} (from 230 μm to 510 μm) and line width w (from 440 μm to 780 μm). However, the arc tilt angle is more closely related to the laser power than the number of scans. The higher laser power results in a steeper slope and the second pass at the same laser power significantly increases the depth of the contour while maintaining a similar arc tilt angle. This study of LIG geometry and laser parameters provides a design guideline to obtain the optimum LIG geometry to fit certain applications given a cork substrate thickness.

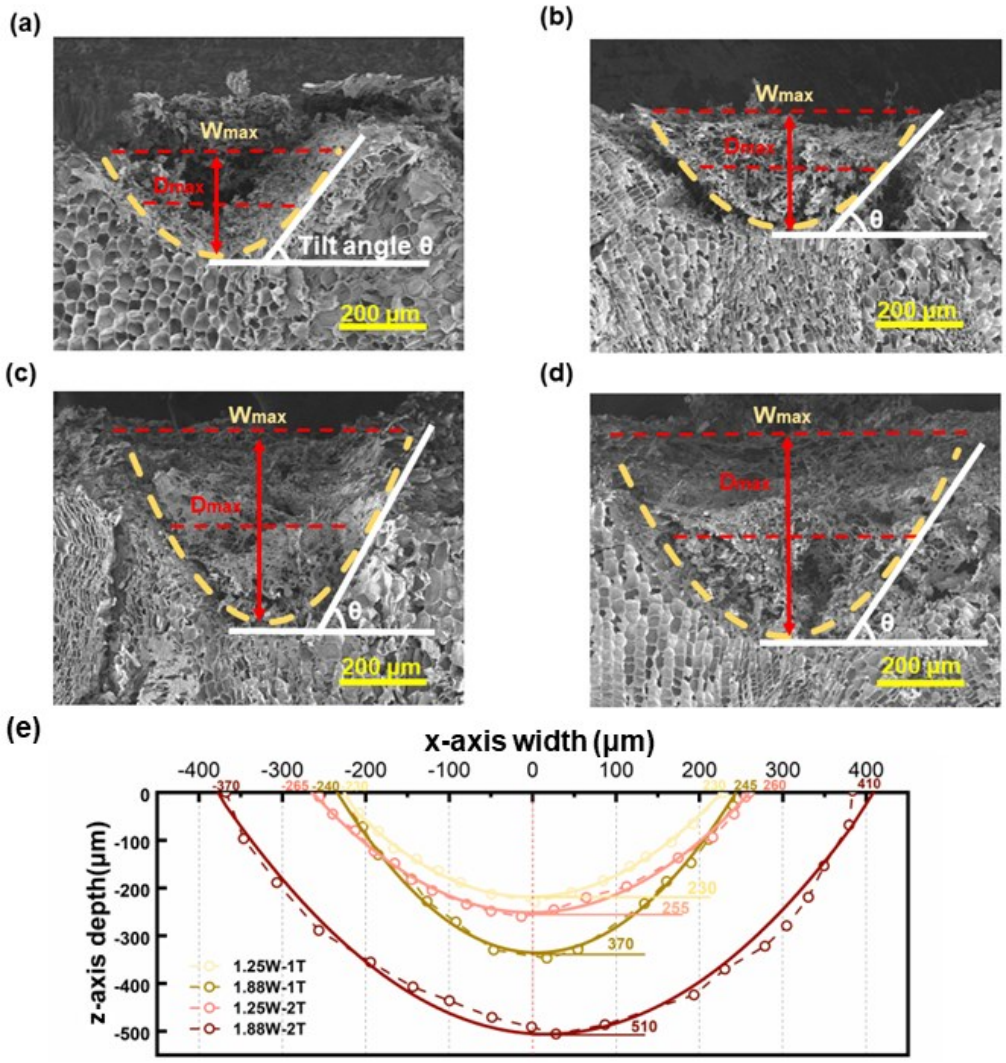

Figure 3.7 SEM images showing the cross-section of single LIG lines and the relationship with F values. (a) LIG-1T-1.25, F= 0.75 J/mm^2. (b) LIG-2T-1.25, F= 1.5 J/mm^2. (c) LIG-1T-1.88, F= 1.13 J/mm^2. (d) LIG-2T-1.88, F= 2.25 J/mm^2. (e) Comparison of the LIG cross-section profiles with varying laser energy at a constant scanning speed of 16.67 mm/s. The profile is fitted using a Gaussian distribution.

3.3.1.3 Raman spectrum and sheet resistance analysis

Raman spectroscopy, which reveals the intensity and symmetry of scattered wave peaks, is regarded as the fingerprint signal and an indispensable approach for identifying and analyzing the structure of all graphitic materials [77]. The Raman spectrum of graphene should have three characteristic peaks: the D peak at around 1350 cm^{-1}, the G peak at around 1580 cm^{-1}, and the 2D peak at around 2700 cm^{-1}. The D band is associated with structural defects, vacancies, and distorted sp^2 bonds, whilst the G band results from the first-order scattering process and the 2D band correlates to the second-order scattering. With the lasing power fixed at 1.25 W, the results of Raman spectroscopy reveal a distinct change in the LIG structure from a single pass up to three passes, as shown in **Figure 3.8 a**. The characteristic peaks of the D, G, and 2D peaks indicate the

presence of graphene in each of the three samples. The peak intensities, corresponding to the heights of the three characteristic peaks, are denoted as I_D, I_G, and I_{2D}. Between the first to third time lasing passes, the decrease in I_D/I_G ratio in the second pass indicates reduced defect density and improved sp^2 crystallinity in the graphene structure. Simultaneously, the increasing I_{2D}/I_G ratio suggests a transition towards fewer graphene layers and enhanced electrical properties. The slightly leftward shift (red-shift) of the 2D peak typically signifies reduced strain on the graphene lattice. These spectral changes altogether indicate the evolution towards higher-quality, less-defective graphene with fewer layers and diminished external perturbations for the second laser passes. Particularly after the second lasing, there is a noticeable increase in the I_{2D}/I_G ratio and significant growth in the 2D peaks, indicating that the additional scanning can improve the quality of the graphene. However, the broader 2D peaks and the increased I_D/I_G ratio after the third pass of lasing indicate a rise in the LIG structural defects. It again confirms that two lasing passes give the optimum graphene structure.

Figure 3.8 b compares the representative Raman spectra of LIG generated at fluence ranging from 0.75 to 3 J/mm^2 (referring to lasing power from 0.625 W to 2.5 W) for two lasing passes. The Raman spectra comparison in **Figure 3.8c** before and after laser treated cork substrates demonstrates that the characteristic 2D and G peaks originate from the LIG formation. The absence of these peaks in the untreated cork spectrum conclusively eliminates any potential contribution from the cork substrate material. **Figure 3.8 d** summarizes the corresponding intensity peak ratios as a function of laser fluence. The decreasing I_D/I_G intensity ratio and the increasing I_{2D}/I_G intensity ratio from 0.75 J/mm^2 to 2.25 J/mm^2 indicate the creation of graphene materials with fewer structural defects and fewer layers. As the fluence energy reaches 3 J/mm^2, greater structural defects and additional graphenic layers appear, revealing that the 2.25 J/mm^2 energy fluence produces graphene of the highest quality among the four chosen fluence values. The exponential relation between sheet resistance (SR) and laser energy fluence is depicted in **Figure 3.8 e**. Within the range of fluence values investigated in this study, an empirical relation $SR = 71.30exp(-F/0.4481) + 0.1974$ can be defined after curve fitting. The electrical conductivity improves with increasing laser fluence as more sp^2 carbon bonds break and sp^3 carbon bonds are produced. Nevertheless, there is no significant change in sheet resistance after 2.1 J/mm^2. At higher laser fluence, the sheet resistance only decreases slightly, but its I_D/I_G ratio increases indicating increasing structural defects in the graphene, and therefore a lower LIG quality. So any further decrease in sheet resistance after 2.25 J/mm^2 is simply due to the increase in the thickness of lower quality LIG. At the optimal point where F= 2.25 J/mm^2, a good balance of the electrical conductivity, the quality of the characteristics, and the degree of substrate distortion is achieved. Consequently, the LIG used in the mesh pattern for damage detection was set at F= 2.25 J/mm^2 achieved by having two lasing passes at the power of 1.88 W, i.e. LIG-2T-1.88.

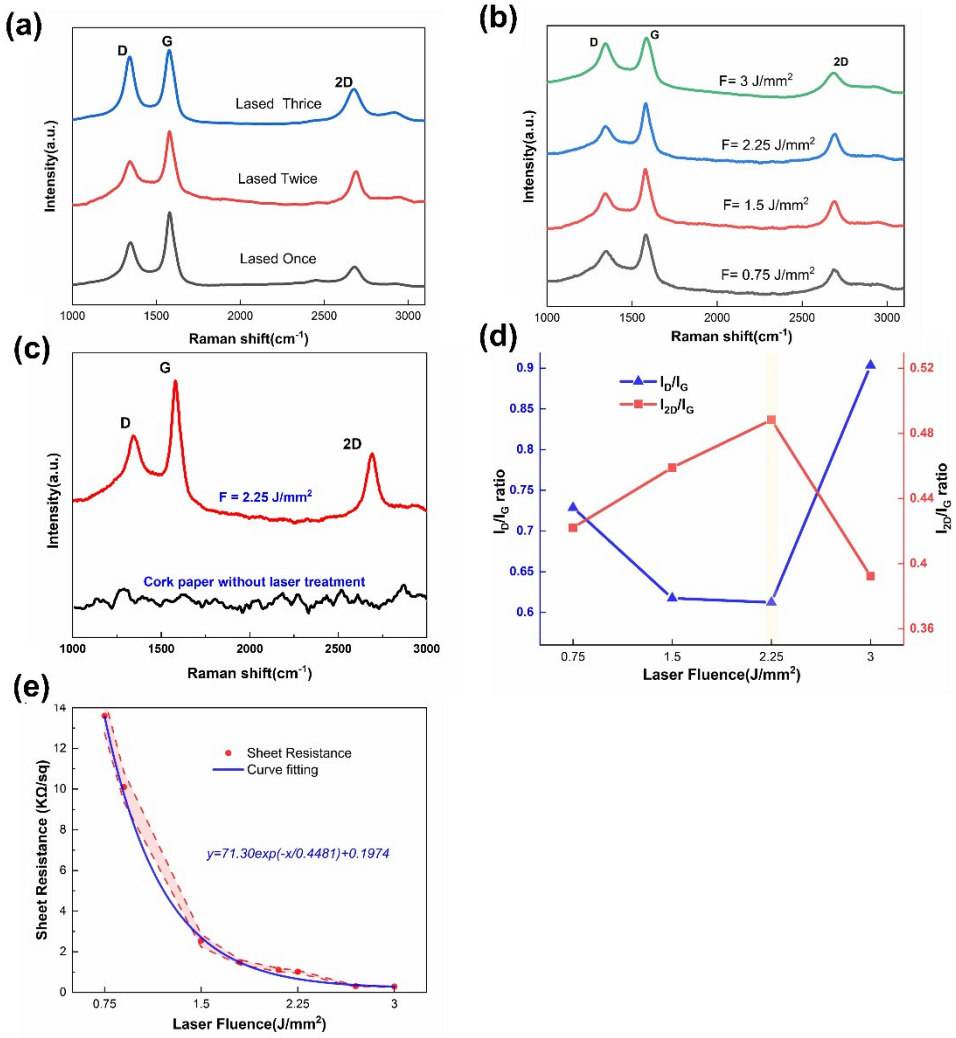

Figure 3.8 Raman spectra of one lasing pass, two lasing passes and three lasing passes on cork paper at the power of 1.25 W; (b) Raman spectra of LIG processed under two-time lasing with varied F value; (c) The comparison of Raman spectra of cork paper before and after laser treatment. (d) I_D/I_G and I_{2D}/I_G ratios of LIG at different F values; (e) Empirical relation between sheet resistance of LIG and laser fluence. (The red region between the dashed lines represents the error domain).

3.3.2 Damage sensing of LIG in composites

Using the optimised laser parameters, the LIG meshes were printed on cork substrates and embedded in S-glass fibre prepreg to fabricate a LIG sandwich composite panel. The initial electrical resistance measurement of the LIG on the cork layer when incoporated as a core material within the composite laminate remains stable (fluctuating within 0.8%) after left unloaded in a room environment for five days. The embedment of cork within the composite matrix mitigates the influence of ambient conditions on the electrical characteristics of cork-LIG, thereby conferring a stable initial baseline for subsequent damage-sensing applications.

Following the impact event, the damage classification of the LIG channels requires some data post-processing as it cannot be performed simply based on the magnitude of electrical resistance change. The impact damage can cause different amounts of resistance change in the LIG channels, depending on the location and energy of the impact on the LIG mesh pattern. When the damage occurs at the edge of the plate, there are fewer intact channels around the neighbourhood of the affected channels to serve as alternative electrical routes for resistance measurement, resulting in a significant increase in resistance. In contrast, affected channels in the centre of the plate are surrounded by more intact channels which are closely packed, giving a smaller increase in resistance. Moreover, some LIG channels in the small neighbourhood of the impact zone can also experience a small increase in resistance due to the energy dissipation after the impact event. To simplify the analysis for damage classification, the resistance changes of each channel in the same plate were fitted to a normal distribution, with the mean (μ) and standard deviation (std) calculated. A damage threshold was established at one standard deviation (1 std) of resistance change determined from the results of impact test at 10 J. The damage threshold of one standard deviation is chosen here as the standard deviation is a common concept in statistics to determine what constitutes an outlier and what does not. The channels are diagnosed as damaged when their resistance change exceeds the damage threshold value of 1std. The damage threshold may vary slightly for each plate depending on the damage location. For instance, plates with more affected channels—particularly those damaged in the central region—may exhibit a higher threshold (e.g., exceeding 1 standard deviation, such as 1.1 std). However, determining the exact threshold is highly labour-intensive, as it relies on purely numerical analysis and cannot be generalized to other plates; therefore, this study set the damage threshold at 1 std and use a machine learning algorithm for further post-data analysis. A sensitivity analysis was conducted to determine the optimal threshold by comparing 0.9 std (selecting 30 channels) and 1.1 std (selecting 23 channels) against the baseline of 1 std (28 channels). The results demonstrate that 1 std provides the balanced selection with the reference from **Figure 3.10**, as lower thresholds lead to over-selection (0.9 std) while higher thresholds result in under-selection (1.1 std). In practice, the value of the damage threshold can be adjusted depending on the required conservatism.

Figure 3.9 displays the resistance change for each channel of the six training plates, along with the corresponding threshold line used to distinguish the damaged channels. Four out of the six plates (Mesh 1- 4) were impacted in the middle with a 4.5 mm LIG channel spacing, whereas the remaining two (Mesh 5 and 6) were impacted near the edge of the plate with channels having an 8 to 9 mm channel spacing. Although impact damage was consistently induced in the central region for Meshes 1–4, slight variations in channel accessibility were observed. The detailed damage locations were subsequently verified through CT analysis, as presented in **Figure 3.10**.

The channels with resistance changes that exceeded the threshold are highlighted in beige in the figure indicating damaged channels.

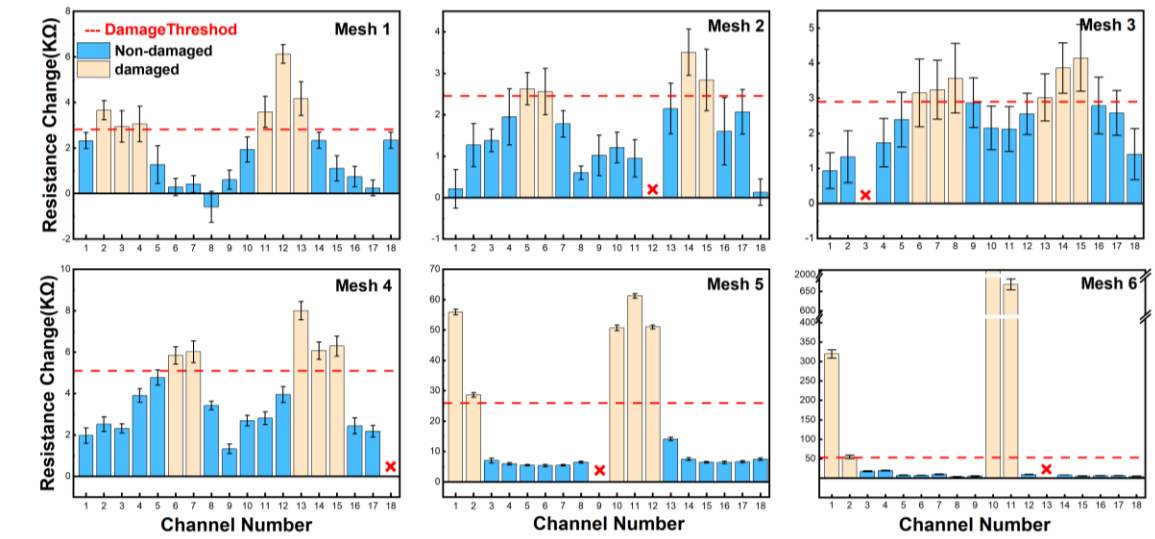

Figure 3.9 The channel-by-channel resistance change of the LIG mesh after the impact event of 10 J of 6 composite plates. Mesh 1 to 4 were impacted in the centre of the plate while mesh 5 and 6 at the edge of the plate. The red dash lines show the damage threshold (1 std standard deviation) calculated by normal distributions. The red cross represents the disconnected damaged channels.

The results of channel resistance changes can be translated to a 2D damage heatmap to indicate the damage location and its size on the composite plates. Each horizontal and vertical LIG channel was assigned a binary number for damage condition classification after impact [78], i.e. 0 when undamaged and 1 when damaged. Damage heatmaps were generated by summing the binary values at the location where the horizontal and vertical LIG channels intersect, as shown in **Figure 3.10 (right)**. The intersection points having values equal to 2, therefore, marking the damaged area and its frequency of appearance on the plate can provide an estimate of the damage size. The damage sensing capability of the LIG channels was assessed by comparing the damage heatmaps with the scan results of X-ray CT of the same specimens. The CT images of the plates were reconstructed focusing on the interface between the top face sheet and the cork layer. The computed tomography (CT) images were converted to grayscale representations before further processing. To enhance the visualization of the CT results, the damaged or delaminated regions were highlighted in red utilizing the masking function (cvtColor). This masking process capitalised on the discrepancy in the grayscale values between the solid and air regions (i.e., delamination opening) within the plates. The comparison reveals a strong correlation between the electrical resistance heatmap and the presence of damaged channels observed in the CT images, confirming the sensing capability of the resistance-based LIG mesh for detecting impact

damage. The good agreement between the measured and CT scan results shows that one standard deviation is a sensible choice.

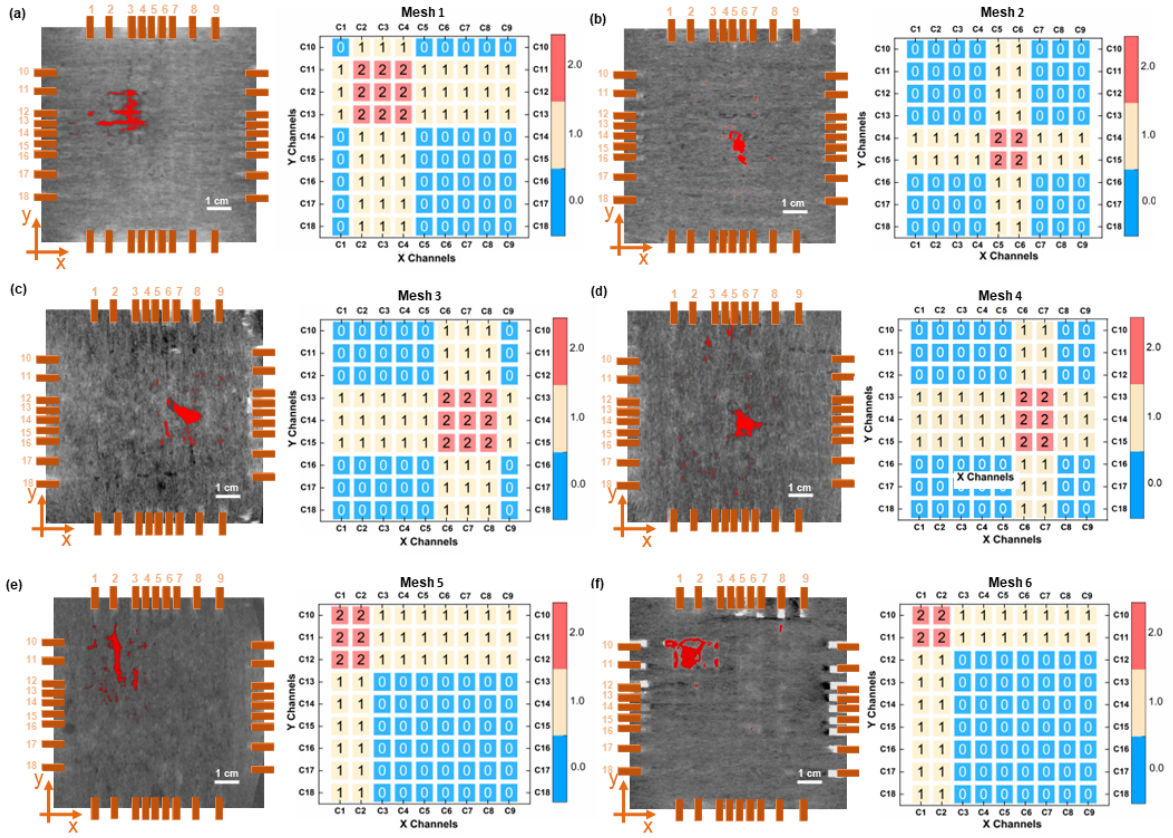

Figure 3.10 The damage heatmaps (right) generated based on channel-by-channel resistance changes and compared against X-ray computed tomography (CT) images (left) for (a) Mesh 1, (b) Mesh 2, (c) Mesh 3, (d) Mesh 4, (e) Mesh 5, (f) Mesh 6. The delaminated regions are highlighted in red in the CT images.

3.3.3 Damage classification by machine learning

It is challenging to distinguish between LIG channels whose electrical resistance changes result from direct impact damage and those marginally affected by propagated delamination in the adjacent areas. For example, extensive damage can substantially increase the mean value of resistance change across the plate and heavily skew the dataset, therefore, neglecting the resistance changes of moderately damaged channels (i.e. erroneously treating them as undamaged when they should be considered as damaged) under the enlarged standard deviation range. Subtle differences in resistance change can also arise between damaged and non-damaged LIG channels depending on the damage location and the impact energy. A simple machine learning (ML) approach was therefore adopted to offer a more adaptive and efficient solution for damage assessment. The integration of ML techniques in self-sensing composites

offers several advantages. Firstly, it eliminates the need to establish new resistance change thresholds for different impact scenarios. The model can also be easily adjusted to meet the desired level of conservatism for specific applications. Secondly, it enables automated and continuous monitoring of complex composite structures with sophisticated LIG patterns and a large dataset, providing a more comprehensive understanding of their condition compared to conventional human inspection methods. Once the models are trained, new test data can be input into the trained models, which subsequently predict the presence, location, and severity of damage in the composite material in a unified working flow. Thirdly, ML models hold great promise for improving the reliability of the prediction with lower experiment costs. For example, the K-Nearest Neighbour (KNN) was applied to predict the fracture toughness of silica particles reinforced polymer composites [79]. With limited experimentation, the KNN model accurately predicted the fracture behaviour of different aspect ratio composites with an accuracy of 96%.

In this study, the KNN model was selected due to its minimal parameter tuning requirements and the limited training data obtainable from experiments [80]. The KNN algorithm is a non-parametric, instance-based learning method that classifies new instances based on their similarity to existing instances in the training dataset[81]. Compared to more advanced models, such as Convolutional Neural Networks (CNNs), KNN employs lazy learning, deferring model construction until a new instance requires classification which makes it computationally efficient for small datasets and less susceptible to overfitting. In terms of model performance, the KNN model is capable of handling non-linear decisions Its accuracy after all the hyperparameters are optimised could be comparable to multilayer neural networks. Furthermore, when compared to algorithms that rely on feature importance or feature selection, such as the decision tree method, KNN is less sensitive to irrelevant features in the dataset. It focuses on the proximity of data points in the feature space and gives labels based on similar neighbours. For the KNN algorithm, hyperparameters are parameters that are not learned from the data but are set by the user prior to training the model. These hyperparameters substantially affect the KNN model's behaviour and performance. Aside from the weighting system discussed above, two additional key hyperparameters are introduced for a better understanding of the model training process.

Number of Neighbours (K), defines the number of adjacent neighbours taken into account when making prediction. Choosing a suitable value for k is essential. A smaller value of K can result in more adaptable decision boundaries, but it may be more susceptible to noise; conversely, a larger value of K can smooth the decision boundaries, but it may neglect local patterns. The optimal value of K depends on the dataset and the problem at hand and is usually found through the grid search and cross-validation approach during model training. The second hyperparameter is the Distance Threshold. The distance threshold parameter can be used to restrict the search space for the nearest neighbour algorithm. By establishing a distance threshold, the algorithm

can disregard data points beyond a certain distance, thereby reducing the search space and enhancing computational efficiency. This parameter can be useful when coping with a huge change in resistance when the damage completely breaks the connectivity of the LIG channels and significant change the plane average resistance. The selection of an appropriate distance threshold is dependent on the data characteristics, problem domain, and data understanding.

To ensure accurate model training and mitigate potential classification biases, data preprocessing techniques were implemented prior to model construction. Any resistance changes of the LIG channel exceeding 2 MΩ (about 60 times more than the typical initial resistance reading), were confidently identified as a completely broken channel and were excluded from the calculation as it could heavily distort the normal distribution of the results. The decimal scaling normalization, and oversampling were employed to improve the comparison of data points from six training plates and to speed up the learning process[82]. To further improve the prediction accuracy of the algorithm, a hyperparameter tuning process was undertaken through the grid search algorithm [83]. The KNN model hyperparameters subjected to optimization includes the k values, which determine the number of nearest neighbours considered for data processing; the distance threshold, which determines the maximum distance a data point can be away from its nearest neighbours to be considered in the same class; the distance metrics, which quantify the dissimilarity between data points through different distance function, and the weight function, which is responsible for assigning relative importance to the k nearest neighbours. The logic behind weighted KNN is to give more weight to nearby data points and less weight to distant points, thereby improving the prediction performance.

The remaining three composite plates from the test group were employed to validate the predictions made by the KNN model, after comparing the results with the X-ray CT images. The impact damage detection workflow for these plates is summarised in **Figure 3.11**. The electrical resistance change ($\triangle R_i$), average plate resistance change ($\triangle R_{average}$), relative resistance change ($\triangle R_i - \triangle R_{average}$), and the standard deviation of plate resistance change (std_i) were selected as input features (f) to the KNN model. All the input parameters and definitions used in the model training are summarized in **Table 3.1**. The KNN algorithm and data processing code in this study were implemented using Python 3.9 and the Scikit-learn package for machine learning. The matplotlib and cv2 package was used to create visualization [84].

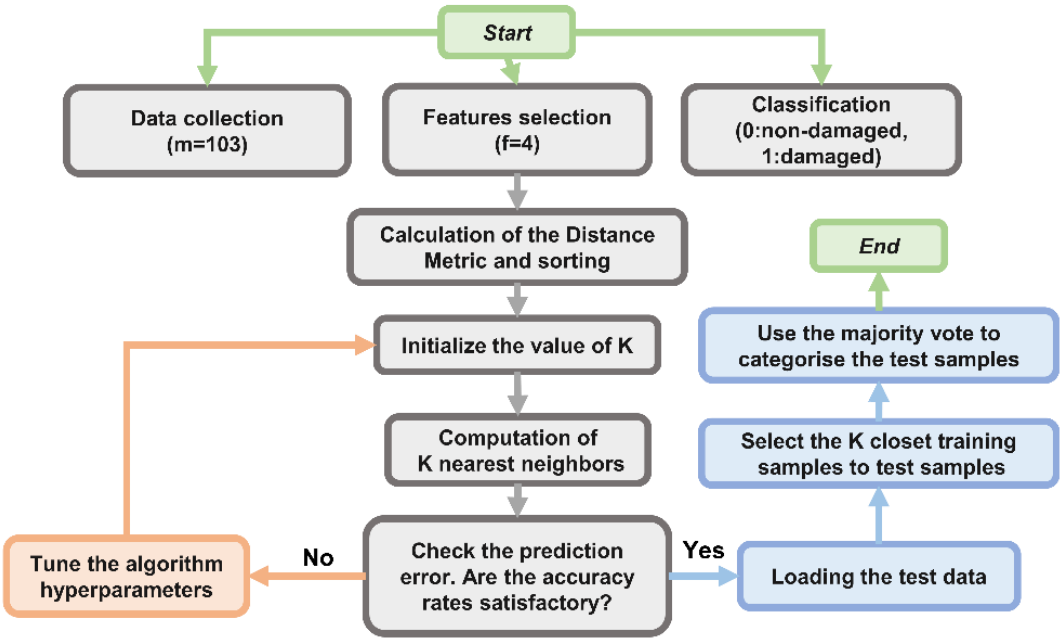

Figure 3.11 Flowchart depicting the process of applying the KNN model to predict outcomes for new test samples. The steps for model training are coloured grey, while the steps for model validation are in blue.

A total of 103 data points (*m*) were collected from the six training plates. The training accuracy is calculated based on the mean accuracy of a 10-fold cross-validation test against various values of K neighbours. The four features used in KNN model were analyzed using Pearson correlation, with results visualized in the heatmap (**Figure 3.12**). All feature pairs exhibited weak to moderate correlations ($|r| < 0.6$), indicating minimal redundancy. This low inter-feature correlation enhances model performance by ensuring each feature provides distinct information, thereby improving the accuracy of distance-based calculations in KNN. Furthermore, it maintains computational efficiency by preventing redundant processing of highly correlated variables. The absence of strong correlations ($|r| \geqslant 0.6$) helps mitigate overfitting and preserves meaningful distance metrics in the feature space, allowing effective utilization of all features without pattern duplication. **Figure 3.13** depicts the training accuracy with different hyperparameters in the KNN model. After optimised the hyperparameters of the KNN model through the grid search method, the K values = 5 were selected with a distance threshold set at 0.4, using the Euclidean distance metric and Gaussian Kernel weighting method [83]. This configuration was determined based on the criteria of maximizing the overall accuracy while minimizing the false negative rate, which corresponds to cases where the presence of damage was not detected.

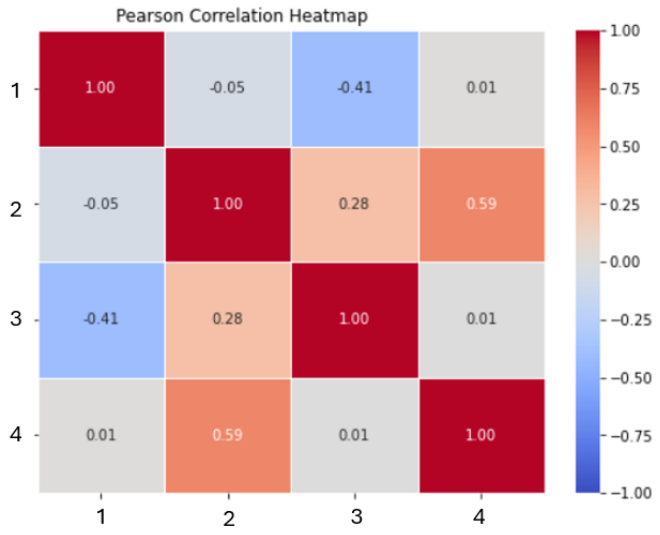

Figure 3.12 The Pearson heatmap between the four training features in KNN model.

Table 3.1 The training inputs for the KNN model and the data pre-processing methods before the model training.

Input parameters	**Definitions**	**Equations**
Electrical resistance change	The resistance changes of each channel before and after impact (The average of three measurements).	$\triangle R_i = R - R_i$ (i ϵ [1,18], refers to the numbering of each channel)
Average plate resistance change	The average resistance changes of all the connected channels (**n** is the number of the connected channels) on the same plate.	$R_{average} = (\sum_{i=1}^{n} R_i)/ n$
Relative resistance change	The difference between resistance change of channel **i** and the average plate resistance change.	$\triangle R_i - \triangle R_{average}$
Standard deviation of plate resistance change	The amount of variation or dispersion of the channel resistance value about the average plate resistance change (mean).	$\text{std} = \sqrt{\frac{\sum_{i=1}^{n}(R_i - R_{average})^2}{n-1}}$
Synthetic Minority Over-sampling Technique (SMOTE)	Select a minority instance and generate new samples to make the input classification case balance.	smote = SMOTE(sampling_strategy=1, random_state=42)
Truncation function	Defining an upper limit (chosen to be 60 times compare to the original channel resistance values) to eliminate extreme values.	Math.truc (original, upper limit)
Decimal scaling normalization	Converting the values of numeric resistance change to a	Resistance/ max(np.abs(Resistance))

	common scale by dividing it by the maximum absolute value of the attribute.	

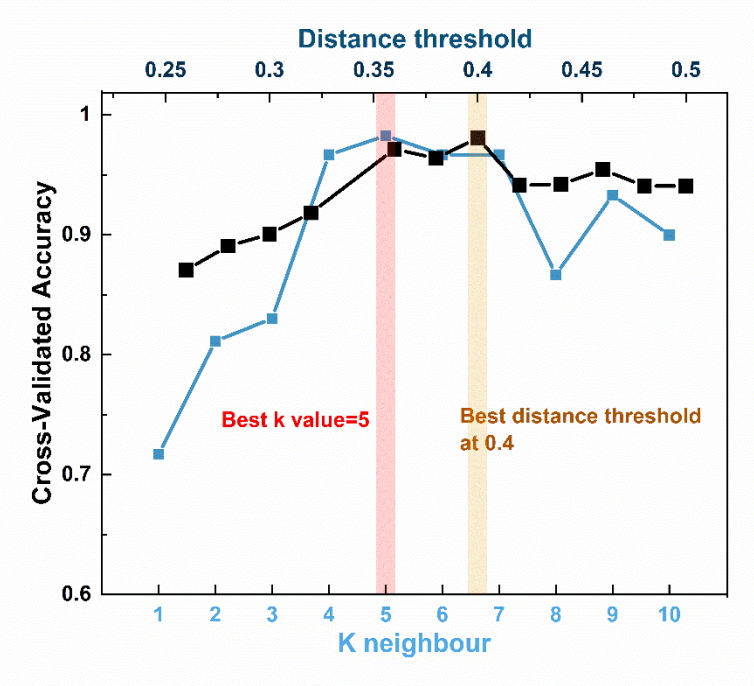

Figure 3.13 The 10-fold cross-validation test accuracy at different k values and distance Thresholds.

To evaluate the KNN model's predictive performance on new cases, especially across various impact energies, it was tested against three additional plates (i.e. Mesh 7, Mesh 8 and Mesh 9) with impact energies of 10 and 12 J applied at the centre and 15 J at the edge of the plates. The prediction results by the KNN model for the test (validation) group are shown in **Figure 3.14**, compared against the results predicted by the manual statistical approach using the fixed 1 std as the damage threshold. **Table 3.2** summarises the performance of the KNN model using the classical statistical framework of a confusion matrix [85], showing 3 false positives (FP = 3) and 0 false negative (FN = 0). From a risk mitigation perspective, it is preferable for the model to err on the side of false positive predictions rather than false negatives. False positive predictions, while potentially leading to unnecessary inspections, pose a lesser risk compared to the potential consequences of false negatives, which fail to detect the presence of damage and can result in catastrophic failure or outcomes. To facilitate result validation, the CT scan results were also converted into the same damage heatmap in **Figure 3.14**. For the test case of 10 J, both manual statistical and machine learning approaches give 100% agreement with the CT scan results in terms of damage location and size. This is expected as the manual statistical approach has already been proven in Section 3.3.2 for the impact energy of 10 J, while the KNN model was trained using datasets of the same impact energy level of 10 J. In the case of 12 J, both the manual

statistical approach and the KNN model overestimate the extent of damage, treating the undamaged LIG channels areas in close proximity to the impact zone as damaged. However, at the highest impact energy level of 15 J, the manual statistical approach underestimates the damage area resulting in two LIG channels with false negative, while the KNN model continues to slightly overestimate the damage area. Overall, the KNN model demonstrated greater reliability and consistency in damage area estimation across varying impact energies, especially in identifying damage in high-energy impact scenarios from the conservative perspective. The KNN model enhanced the accuracy by 3.7 %. However, further improvement was not feasible with limited training data because of the application constraints necessary to preserve the model's conservatism. Ensuring zero instances of damaged cases being misclassified as non-damaged is critical in composites structural monitoring and safety control.

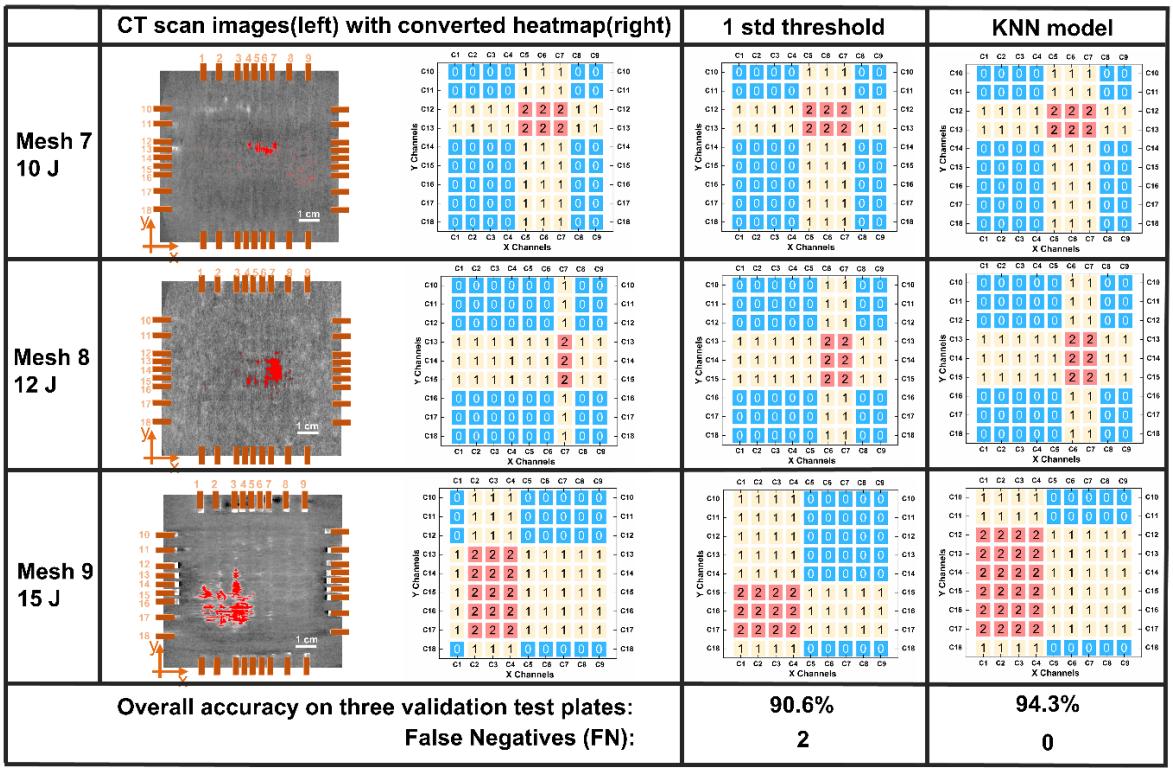

Figure 3.14 The three validation test plates after impact damage at different energies. First column - CT scan images with the actual damage area highlighted in red and converted heatmap based on the CT scan results; second column – prediction by the 1std threshold method; third column – prediction by the KNN model.

Figure 3.15 shows the data distribution of the training dataset and the prediction results for test (validation) datasets on the same plot. Each data point corresponds to one channel, and the erroneous prediction by the KNN model is highlighted in maroon (those data points with a cross). The KNN's strength lies in its ability to better handle individual outliers compared to a rigid threshold. As a result, KNN tends to establish localized thresholds that adapt to specific data

regions, rather than applying a global threshold across the entire dataset. In this study, the accuracy refers to how close a measured value is to the true value, while precision indicates the consistency of repeated measurements. This adaptive approach allows KNN to capture nuanced variations in new cases with higher accuracy. Overall, the K-nearest neighbours (KNN) model demonstrated a high level of predictive performance, with an impressive overall accuracy rate of 94.3%. The algorithm successfully identified all damaged channels. However, the model also incorrectly identified three healthy channels as damaged channels (false positive points in maroon colour). These were the borderline data points belonging to LIG channels with resistance changes close to the damage threshold value due to the greater impact energy compared to the training dataset.

Table 3.2 The confusion matrix result reporting true positives (TP), true negatives (TN), false positives (FP) and false negatives (FN) for the KNN model evaluation.

		Actual Value (based on X-ray CT results)	
		Positive (1)	**Negative (0)**
Predicted Value (by the KNN model)	**Positive (1)**	**TP:17** Correctly detect the presence of damage in the LIG channels	**FP:3** Incorrectly identify damage in the LIG channels when it is actually undamaged
	Negative (0)	**FN:0** Fail to detect the presence of damage in the LIG channels	**TN:33** Correctly identify the non-damaged LIG channels

The confusion matrix can be used to compute statistical evaluation metrics, such as recall and F1-score. It allows identification of the model's strengths and weaknesses, understanding of error patterns, and comparison between different models. The recall score, also known as sensitivity or true positive rate, measures the model's ability to correctly identify actual positive instances [86]. It quantifies the proportion of true positives (TP) that the model correctly classifies. The recall score is calculated as follows:

$$Recall = \frac{TP}{TP+FN} \qquad \text{Equation 3.2}$$

On the other hand, the F1-score represents the harmonic mean of the binary's model precision and recall. By considering both false positives (FP) and false negatives (FN), it provides a balanced evaluation of the model's performance. The F1-score is particularly useful when the class distribution is unbalanced [87]. It rewards models that simultaneously achieve high precision and recall, and penalises models with large disparities between precision and recall. The precision and F1 score are given by:

$$Percision = \frac{TP}{TP+FP} \qquad \text{Equation 3.3}$$

$$F1\ score = \frac{Precison \times Recall}{Precison+Recall} \qquad \text{Equation 3.4}$$

In this study, the recall rate and precision for the damaged channel are 1 and 0.85, respectively, while the F1-score is 0.919, which serves as additional validation of the model's high predictive performance.

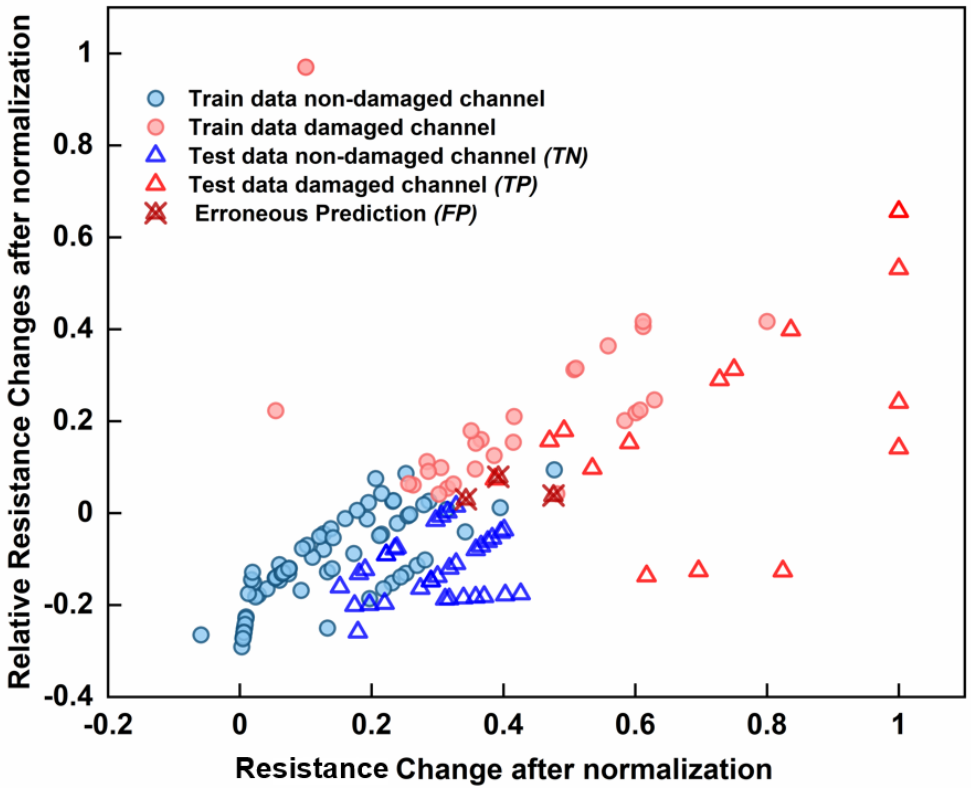

Figure 3.15 The data distribution of the resistance changes after scaling. Blue and red colour representing the non-damaged and damaged channels in both the training and validation datasets. Data points of erroneous prediction are highlighted in maroon.

3.4 Summary

Cork-derived LIG can be produced by an inexpensive commercially available low-power blue light laser engraving system. Compared to PI film, which is the substrate commonly used in the literature for LIG synthesis, the cork has less thermal deformation for larger area. LIG patterns and can integrate well with the epoxy resin matrices. By modifying the lasing parameters, LIG's morphology, graphitization quality, and electrical properties can be tailored according to the application requirements.

The mesh pattern of LIG was able to uniquely identify and estimate the impact damage size in a composite sandwich structure solely by monitoring the electrical resistance changes in a series

of intersecting horizontal and vertical LIG channels. The use of a machine learning algorithm such as the weighted KNN model reduces the reliance on human effort in manually sorting the resistance changes and subjective judgement in determining the damage status, especially when dealing with a large amount of data obtained from a huge composite structure or involving a complicated LIG pattern design. The trained KNN model was used to predict the damage severity of various impact energies and achieved an accuracy rate of 94.3%.

The sensing performance of the LIG mesh design and the accuracy of the KNN model prediction demonstrated a potential low-cost approach for monitoring structural damage in large-scale composite structures. The accuracy of the model can be improved further if more training data sets can be provided under various loading scenarios and damage severity. To enhance fault tolerance and assure structural safety in real-world applications, the model can be adjusted to be conservative depending on the damage tolerance level of the structure, for example by assigning all borderline data points to the ‘damaged’ category.

Chapter 4 Cork-derived LIG as an embedded strain sensor

This chapter investigates the cork-derived LIG as a strain sensor in a sandwich composite structure. The piezoresistive behaviour of LIG was examined across varying strain ranges, including cyclic and monotonic loading. Distinct sensitivity trends in the piezoresistive response were observed depending on the width-to-length of LIG patterns, enabling LIG pattern design tailored to specific operational requirements. A simplified mathematical model was developed to predict the piezoresistivity of LIG as a function of applied strain.

4.1 Introduction

Due to their inhomogeneous and laminated nature, the failure of composite structures is complex, exhibiting a wide variety of failure mechanisms such as matrix cracking, fibre debonding, delamination, and fibre breakage. Due to their high stiffness, FRP composites typically fail abruptly and catastrophically in a brittle manner without any noticeable deformation. The in-situ damage of composite materials can be detected using well-established techniques such as acoustic emission[14] and X-ray computed tomography [16], but they require expensive equipment and in some cases huge post-processing time. Different failure mechanisms and damage severity typically take place at different strain levels. Therefore, the strain values or strain changes can be used to monitor the structural health of FRP composites, if they can be measured in-situ and in real time.

Integration of the strain sensing elements within composite matrices offers several advantages compared to traditional strain gauges which are affixed to the surface. Firstly, the embedded LIG layer protects itself from external environmental factors such as temperature fluctuations, and humidity, which can introduce reading fluctuations. Secondly, the embedded LIG self-sensing composites eliminate the need for external adhesive bonding of strain sensors or gauges, making them ideal for inaccessible regions or structures requiring good surface finishing. The risk of sensor detachment under cyclic loading and long-term adhesive degradation are also reduced. Structural composites are designed to be stiff and typically operate within relatively low strain ranges (below 2%). Prior studies have demonstrated that LIG sensors provide exceptional sensitivity, achieving around 10 times higher gauge factor within low-strain range (approximately 0.2%) [40]. Their high sensitivity at low strain indicates the potential as early damage indicators, enabling preemptive measures to be carried out before severe structural degradation in composite structures. However, compared to PI paper-based LIG sensors which are derived from

loosely packed PI fibers and require more complex substrate fabrication. Cork paper exhibits comparable gas liberation while demonstrating reduced shape distortion when printed over large surfaces. Consequently, the strain-sensing capability of cork-LIG warrants further investigation.

This chapter further explores the same composite lay-up configuration discussed in Chapter 3, where cork-derived LIG is embedded as a core material within the composite sandwich structure, to assess its strain sensing performance in tensile test, including cyclic and monotonic loading. The piezoresistivie sensitivity of the LIG sensors with different channel widths were investigated experimentally. A two-dimensional Random Void Model was developed to describe the microcrack evolution in the LIG layer as a function of applied strain, enabling quantitative correlation between sensor sensitivity and applied strain.

4.2 Experimental setup

4.2.1 LIG and sandwich structure composite fabrication

This section describes the experimental procedures for composite sample preparation and the set-up of mechanical testing. The LIG was synthesised on the same 1 mm thick cork substrates; following the same laser treatment parameters, including power, speed, and number of scans, as discussed in **Section 3.2**. Two lasing passes (double scanning) are necessary to obtain high-quality LIG. Previous research has demonstrated that organic substrates are transformed to amorphous carbon via first-time laser scanning, and subsequently to graphene via second-time scanning [76, 88]. However, it can be challenging to ensure perfect overlap of the two lasing passes to have LIG with consistent quality for all the specimens, especially when this is done for narrow LIG strips or channels. To overcome the issue, the initial pass of laser scanning was first done over a wider area of length 120 mm and width 20 mm to produce amorphous carbon before the second lasing to produce the actual LIG channels of interest. The second pass of laser scanning created two narrow conductive LIG channels of fixed length L=120 mm but with different widths separated by a 4 mm gap, which served as the main sensing element, as depicted in **Figure 4.1 a**. The two-channel sensing element design was chosen to improve the overall robustness and stability of the sensor . Six LIG samples with three different channel widths (C = 3 mm, 4 mm and 5 mm), i.e. two samples for each width, were fabricated to compare their sensing sensitivity and performance.

Following the fabrication of LIG patterns on cork paper, the terminals of each pattern were connected to 0.1 mm thick copper strips, as illustrated in **Figure 4.1 b**. Subsequently, together with the cork paper substrate, they were individually inserted as the core material between two face sheets composed of glass fibre prepregs to form a sandwich composite, with the ends of the

copper strips left exposed to serve as the probing points for piezoresistivity measurement. Each face sheet was composed of six plies of S-913 glass fibre/epoxy prepreg (HexPly, Hexcel United States) arranged in a cross-ply configuration. The lay-ups were vacuum bagged and cured in the autoclave at 120°C (248°F) and 7 bar (101.5 psi) for 60 minutes. During the curing process, the 3D porous microstructure of the graphene sensing component and the cork substrate were infiltrated by the excess semi-cured epoxy resin from the prepreg under heat and pressure, allowing good integration between the different materials after the curing process. The final products were six straight-edged glass fibre sandwich composite samples (2.2 mm thick x 25 mm wide x 250 mm long) with embedded LIG channels serving as the strain sensing elements in the mid-thickness of the laminate. The 2-point method was chosen for LIG electrical resistance measurement of the LIG due to the relatively low contact resistance (on the order of around 100 Ω from the copper wires) compared to the high resistance of the embedded LIG (over 10 kΩ). The two-probe method ensured sufficient accuracy while simplifying both the experimental setup and data interpretation.

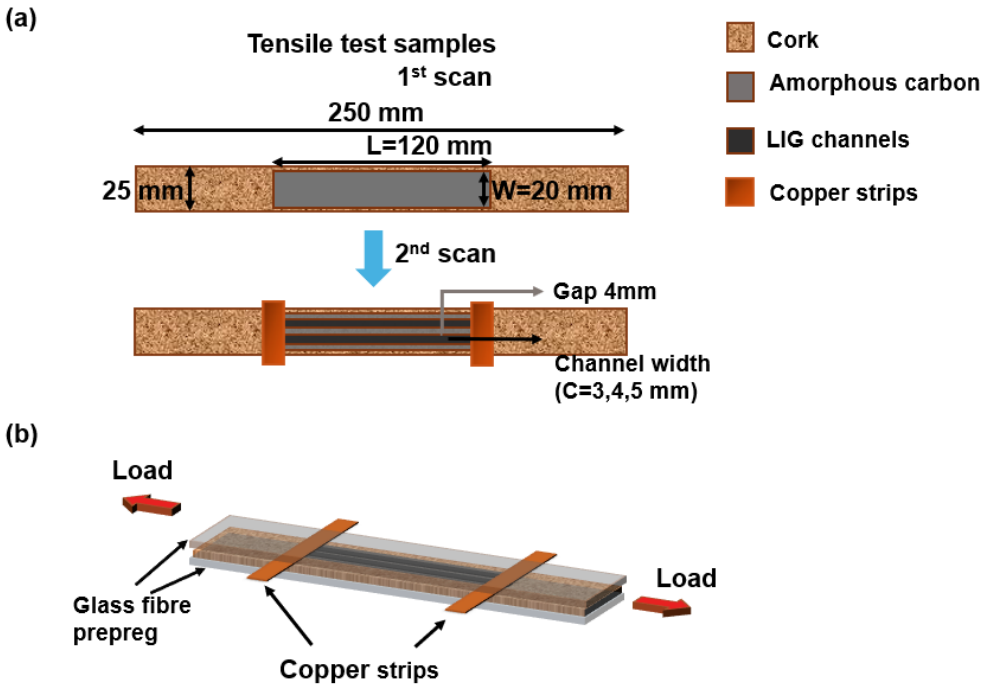

Figure 4.1 (a) Production of amorphous carbon on cork substrate after the first laser scan, and LIG channel after the second laser scan. (b) A sandwich composite sample with embedded LIG and extended and exposed copper strips serve as the probing point for piezoresistivity measurement.

4.2.2 Universal testing machine and Digital Image Correlation (DIC)

A total of six LIG sandwich composite samples (as described in Section 4.2.1) with three different LIG channel widths (i.e. two samples for each LIG channel width of 3 mm, 4 mm and 5 mm) were studied to investigate their strain sensing sensitivity under combined monotonic and cyclic tensile loading. The complete loading history for each composite sample is summarized in the test matrix in **Table 4.1**. The types of mechanical loading include low-load cyclic tensile loading (5 cycles up to 1.2 kN, or 0.08% strain), moderate-load cyclic tensile loading (5 cycles up to 8 kN, or 0.7% strain), and monotonic tensile loading up to 20 kN (or 1.8% strain). Given the small number of samples, the test matrix was designed to optimise the research outcomes such that the overall reliability of LIG as a strain sensor and their limitation over complex loading history can be assessed. They were tested in the load-controlled mode in a universal testing machine (Shimadzu AGX-50kNV) with a 50 kN load cell. The low-load and moderate-load cyclic loading were performed at a crosshead displacement rate of 0.2 mm/min and 1 mm/min respectively, while the monotonic tensile testing was performed at a crosshead displacement rate of 1 mm/min. In accordance with ASTM D3039, which recommends a displacement rate of 1–2 mm/min for polymer matrix composites to maintain quasi-static loading conditions, a testing speed of 1 mm/min was selected. This choice minimizes dynamic effects while allowing precise observation of defect evolution, such as crack propagation, without overshooting the critical strain range. The difference in loading rate did not contribute any strain rate effect as they were both considered quasi-static loading rates. A higher displacement rate was deliberately chosen for the high-load cyclic case such that it gave the same amount of data points for subsequent data processing. Before the actual loading, all the samples were preloaded to 1.2 kN (or 0.08% strain) in order to iron out any irregularity in the internal structure of the LIG and allow it to settle into a more stable configuration.

It is assumed that strain is uniform throughout the gauge section of the straight-edged samples. The strain was measured using non-contact digital extensometry. The digital extensometry was done using a calibrated stereo camera setup (Teledyne Flir 5 MP (2,448 × 2,048 pixels) monochromatic Blackfly S cameras) fitted with 50 mm focal length lenses at stereo angle 13.6°. Two radial markers with an initial separation distance of 50 mm were glued on the gauge section of each specimen to serve as the reference points. During tensile loading, the separation of the two markers were tracked by digital image correlation (DIC) principles using the commercial DIC software MatchID. Based on the displacements of both markers and their initial separation, engineering strain in the gauge section of the samples can be determined. The DIC workflow is depicted in **Figure 4.2 a**. The digital images were taken at 2 frames per second, with a spatial resolution of 23.5 pixels/mm. To investigate the piezoresistivity, a digital multimeter (Keysight, 2110) was connected to the copper strips of each sample to monitor the electrical resistance

variations during the tensile loading. A small current of 10 μA was applied by the multimeter to ensure no significant Joule heating in the LIG. The acquisition of load and DIC images was synchronised using a NI 4431 data acquisition system (DAQ), while synchronization with the real-time electrical resistance data was achieved based on the timestamp provided by the computers. The test equipment setup and mounted sample are shown in **Figure 4.2 b**.

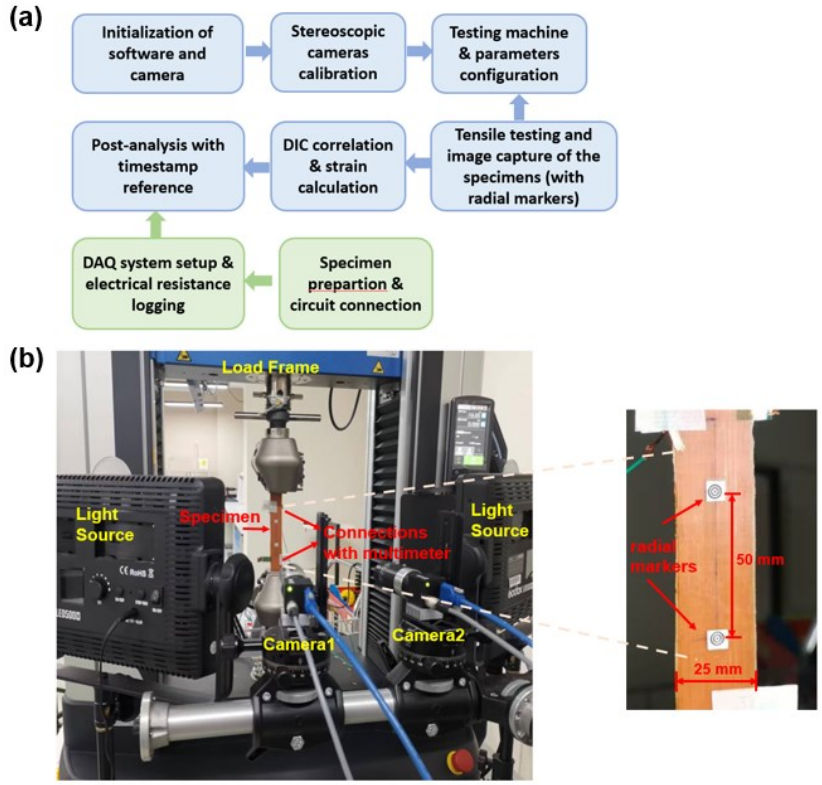

Figure 4.2 (a) The workflow of DIC and DAQ system with the cyclic loading test. (b) Full experimental setup together with sample with radial markers for digital extensometery.

Table 4.1 Mechanical loading history for each sandwich composite sample.

Sample no.	**LIG channel width (mm)**	**Mechanical loading (all in tension)** (same loading/unloading speed for all test 1 mm/min)
S1	3	Preloading to 1.2 kN →cyclic loading to 1.2 kN (5 cycles)→ monotonic loading to 20 kN
S2		Preloading to 1.2 kN → cyclic loading to 8 kN (5 cycles) → monotonic loading to 20 kN
S3	4	Preloading to 1.2 kN → cyclic loading to 1.2 kN (5 cycles) → monotonic loading to 20 kN
S4		Preloading to 1.2 kN → cyclic loading to 8 kN (5 cycles) → monotonic loading to 20 kN

S5	5	Preloading to 1.2 kN → cyclic loading to 1.2 kN (5 cycles) → monotonic loading to 20 kN
S6 (control sample)		Preloading to 1.2 kN → monotonic loading to 20 kN

4.3 Results and discussion

Experiments were conducted on samples featuring varying LIG channel widths under tensile tests. The sensing patterns observed across different LIG channel widths were systematically compared and analysed to assess the influence of LIG geometry, particularly the width-to-length ratio, on the sensor's performance.

4.3.1 In-situ strain sensing during low-load cyclic tensile test

Three samples with different LIG channel widths (i.e. Sample S1, S3 and S5 in **Table 4.1**) underwent cyclic tensile loading up to 1.2 kN for 5 cycles. **Figure 4.3 a-c** displays the applied load versus engineering strain measured using DIC for the three composite samples. The applied load exhibits a consistent linear relationship with strain for all the samples, regardless of the LIG channel widths. The results indicate that the samples were operating in the linear elastic regime and that their stiffness was unaffected by the width of the LIG channels, or the geometrical design of the LIG pattern. The figures also show a small degree of hysteresis phenomenon in the load-strain curves for all composite samples, with the loading and unloading cycles slightly deviating from one another, signifying a small amount of energy dissipation. This is typical behaviour of polymeric composites which exhibit viscoelastic properties [89, 90]. **Figure 4.3 d -f** show the relative change of electrical resistance ($\Delta R/R_0$) plotted against applied strain for the LIG channels with different widths for 5 loading cycles, where R_0 and ΔR are the initial (reference) resistance and the resistance change during loading respectively. The scatter plot employs five distinct colours to distinguish the data points of the five cycles. The scattering in data points of the electrical resistance signal is attributed to the noise in resistance measurement of each cycle, which is commonly seen in many sensors based on a carbon nanomaterials[57, 62]. Closer inspection of the data trajectories from Cycle 1 to Cycle 5 reveal a marginal slope increment, suggesting potential slight material degradation or rearrangement in the LIG microstructure following the low-load cyclic tests.

Overall, at low load, the data trend can be reasonably approximated using a linear fit, as evidenced by the high R-square values above 0.95 in **Figure 4.3**. This indicates that the LIG

structure remains stable after infiltration by the epoxy resin and integration well with the composite matrix. The experimental results align with the earlier observation from other researchers regarding the inherent mechanism of piezoresistivity of LIG microstructure. The application of a load to the 3D microstructure of the LIG leads to the formation and opening of microcracks within the porous conductive network of the LIG, as shown in Figure **4.4** [91]. It causes a reduction in the number of conductive contacts and an increase in electrical impedance. As the load and strain decrease in the unloading process, these microcracks are closed and the conductive networks are repaired or recovered. For small strain loading up to 0.08%, the mechanical damage or plastic deformation within the composite structure was negligible. Most of the microcracks were recoverable and no significant permanent separation within the LIG microstructure was expected. Therefore, the performance of LIG working as a strain sensor at a low load or strain level was found to be reversible and repeatable. For each loading and unloading cycle, a small degree of hysteresis could also be observed, indicating that there was a slight difference in piezoresistivity in the loading and unloading responses due to the time delay in stretching and relaxing of the porous microstructure of the LIG when it is embedded in the viscoelastic epoxy matrix.

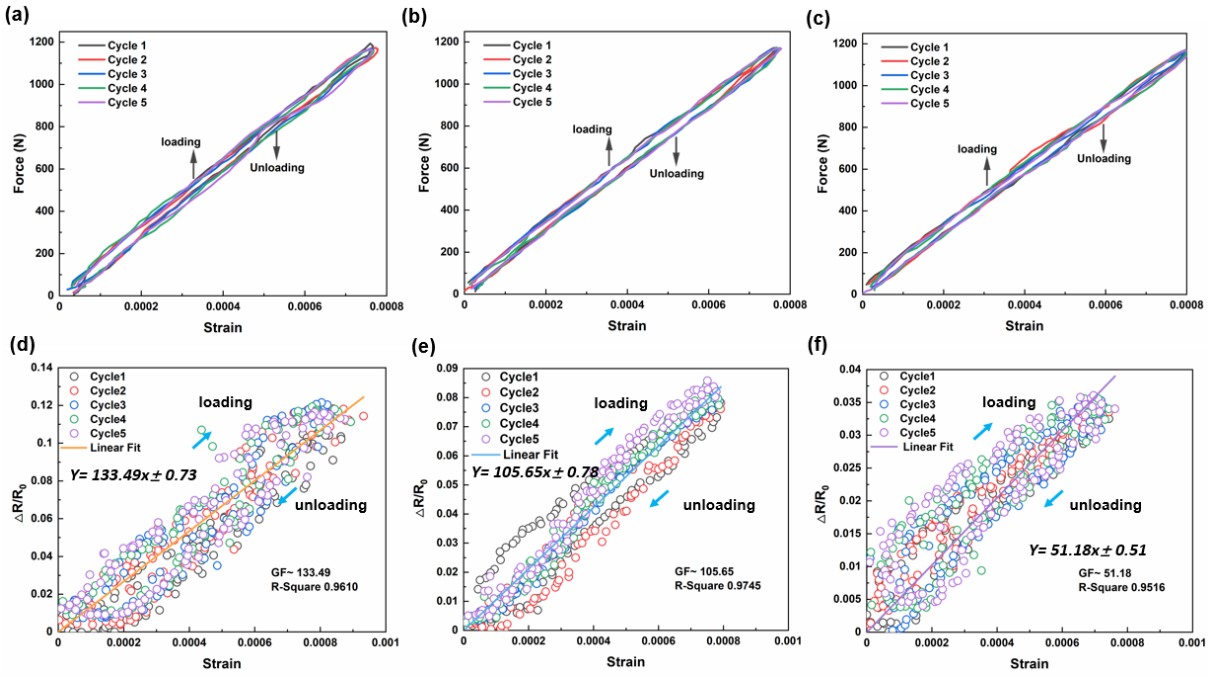

Figure 4.3 The cyclic tensile test results for samples of different LIG widths up to 1.2 kN for 5 load cycles. The applied force versus strain for LIG channel widths of (a) 3mm, (b) 4mm and (c) 5mm. The resistance changes versus strain for LIG channel widths of (d) 3mm, (e) 4 mm, and (f) 5mm. The linear curve fitting lines were added as $Y = aX \pm b$.

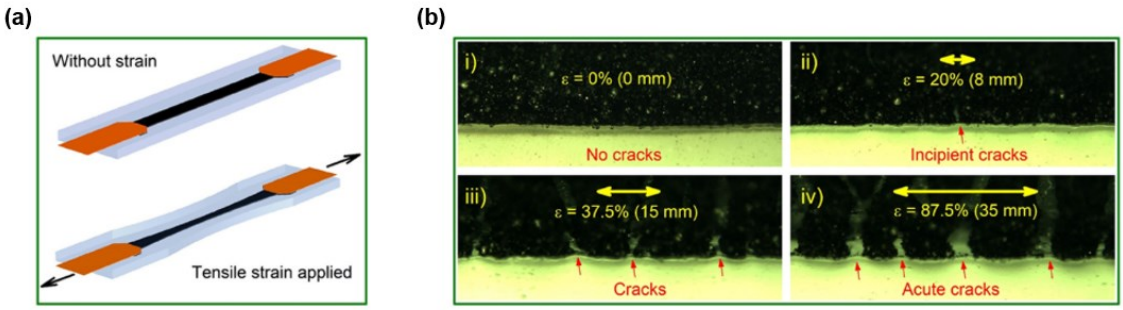

Figure 4.4 (a) Schematic illustration of the sensor under no strain and tensile strain conditions. (b) Optical images showing the formation of cracks at various applied strains [91].

The overall sensitivity of a piezoresistive sensor is measured by gauge factor (GF):

$$GF = \frac{\Delta R/R_0}{\varepsilon} \qquad \text{Equation 4.1}$$

where ε is the applied strain. The GF of a sensor can be simply obtained from the slope of the $\Delta R/R_0$ versus strain plot. In this study, the GF of the samples was calculated by averaging the slopes for all five load cycles. The best fit slopes depicted in the figures show the GF for different LIG channel widths ranging from 50 to 135, demonstrating a strong piezoresistive effect. It is much more sensitive than a metallic strain gauge typically having a GF of about 2 [92]. A narrower LIG channel exhibits higher GF, making it more sensitive to applied strain. This is due to reduced electrical connectivity and higher current density distribution in the narrower LIG channel. Defect distribution is similar in both one-time and two-time lased areas. When the defects propagate to or grow within the narrower channel upon loading, they cause more significant disruption to its electrical conductivity as there are fewer alternative conductive paths exist around the defects. This explains the results which indicate that a small variation of LIG channel width (from 3 mm to 5 mm) leads to a significant change in the GF values (from 133 to 51). The desired sensitivity of a LIG sensor is therefore tailorable by simply varying its channel width. The detailed schematic of conductive channel width and conductivity relationship will be displayed in Section 4.3.4.

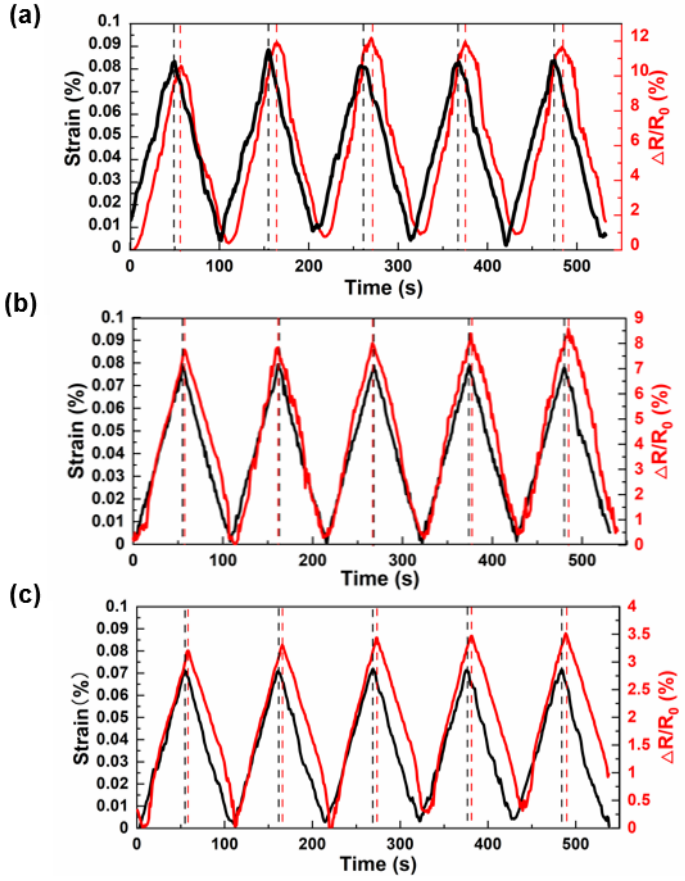

Figure 4.5 The cyclic test strain and electrical resistance change as a function of time at low load up to 1.2 kN, for LIG channel widths of (a) 3mm, (b) 4mm and (c) 5mm.

Figure 4.5 shows the variation of applied strain and electrical resistance change as a function of time for five loading cycles. Note that the preload cycles were excluded in **Figure 4.5**, so the residual strain and resistance change did not begin at zero. The responsiveness of the LIG strain sensor can be studied using peak shift analysis by tracking changes in electrical resistance in response to applied strain in the time domain. Peak shift can be calculated as follows [25, 93]:

$$peak\ shift\ (\%) = \frac{\Delta t}{t_p} \times 100 \qquad \text{Equation 4.2}$$

where Δt is the time delay between the peak of applied strain and the electrical resistance response, and t_p denotes the elapsed time from the initial point to the peak of the electrical resistance change response cycle. A high value of peak shift shows a slow response in strain sensing. **Figure 4.6 a** shows the peak shift for the LIG sensors with different channel widths for 5 load cycles up to 1.2 kN. These values were averaged from the five load cycles of each sample. The results show that the responsiveness of the LIG sensor is correlated to the LIG channel width; the wider the LIG channel, the shorter the time delay. This again can be explained by the fact that a wider LIG channel is less affected by the presence of defects and strain-induced disruption in the LIG network. A wider LIG channel has a proportionally wider intact and conductive network which can stretch (upon loading) and relax (upon unloading) more quickly in response to the

applied strain. **Figure 4.6 b** presents the peak shift percentage for 5 load cycles up to 1.2 kN, averaged among the three samples of different LIG widths. This can reveal the evolution of peak shift over the number of cycles and therefore the stability of sensing. The initial two cycles exhibit an increase in peak delay, before it transitions to a steady state where the microstructural rearrangement and interfacial reactions in the LIG network stabilize. The results in this section suggest that the LIG network can maintain consistent piezoresistive response, offering prospective applications in strain sensing and structural health monitoring at low strain levels. A narrower LIG channel is more sensitive to applied strain (higher GF) but is less responsive in time (higher time delay or peak shift).

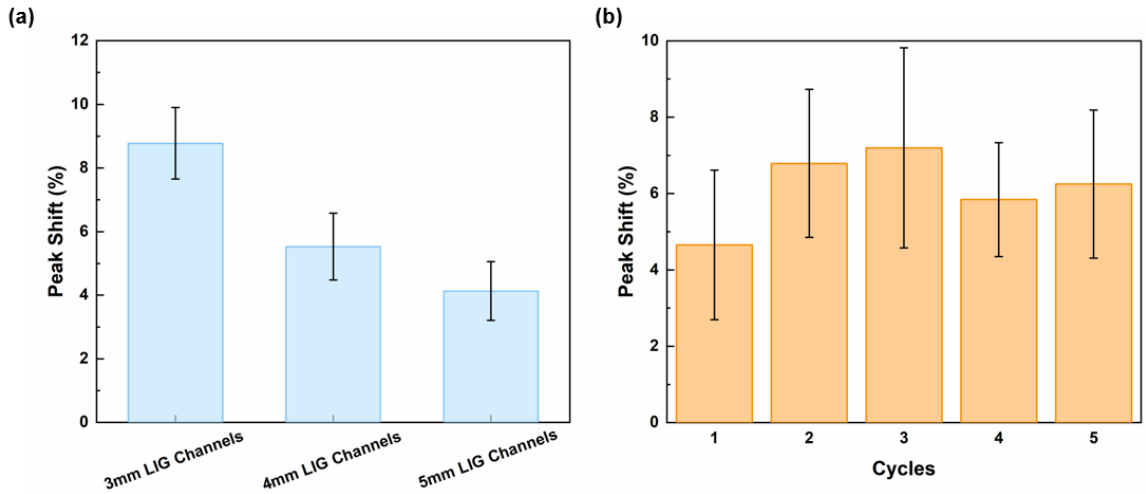

Figure 4.6 Peak shift analysis at low cyclic load (up to 1.2 kN). (a) Peak shift as a function of different LIG channel widths for 5 load cycles. (b) Peak shift as a function of number of load cycles, averaged for 3 LIG channel widths.

4.3.2 In-situ strain sensing during moderate-load cyclic tensile test

Two samples with LIG channel widths of 3 mm and 4 mm (Sample S2 and S4 in **Table 4.1**) were cyclic loaded at a moderate load for 5 cycles up to 8 kN (or 0.7% strain) to study the piezoresistivity at a higher load. The applied strain was still much lower than the tensile strain to failure of the S-glass fibre composite, which was measured to be 2% from initial testing. **Figure 4.7 a and 4.7 d** display the linear relationship between applied load and engineering strain for both samples, again revealing good consistency in the stiffness of the samples, indicating there was no significant damage in the host composite samples. However, the loading and unloading curves now exhibit a more obvious hysteresis effect compared to the previous low-strain loading depicted in **Figure 4.3**, which is expected for a viscoelastic reinforced polymeric composite.

Figures 4.7 b and **4.7 e** show the relationship between relative electrical resistance change and applied strain for the two samples with 3 mm and 4 mm LIG channel width respectively. The data

trend is bilinear, with a distinctive knee in the sensing response around 0.2% strain, as highlighted by the yellow line in the figures. The knee at 0.2% strain suggests the onset of significant alteration in the microstructure of the LIG, potentially caused by the development of irreversible microcracks. This is supported by the upward drift in the hysteresis loops seen after every loading and unloading cycle, showing an increase in gauge factor or sensing sensitivity, equivalent to a reduced effective channel width due to the presence of defects and microcracks. Additionally, a closer inspection revealed that there was increasing initial resistance after each cycle, as depicted in **Figure 4.7 c** and **4.7 f**. The increase in initial resistance after each cycle is greater for LIG channel width of 3 mm than that of 4 mm, again highlighting the sensitivity of narrower channel to defects and microcracks in the porous LIG network. The presence of increasing residual strain upon unloading after each load cycle as measured independently by DIC, despite it is small (in the order of 0.1% - 0.6%), suggests the occurrence of non-visible micro-damage in the host composite, possibly initiated after 0.2% strain, which could also contribute to the irreversible LIG network modifications during the tensile cyclic loading. At a higher load, it is also likely that the LIG detaches partially from the cork substrate following the formation of microcracks in the host composite or the cork substrate, resulting in increasing initial electrical resistance reading after each cycle. The observed trend of increasing initial resistance and strain in each cycle is consistent with the findings seen in the case of carbon nanotubes (CNTs) covering composites [94], recycled carbon fibre reinforced composites [93]and graphene nanoplates doping composites during cyclic loading [12, 95].

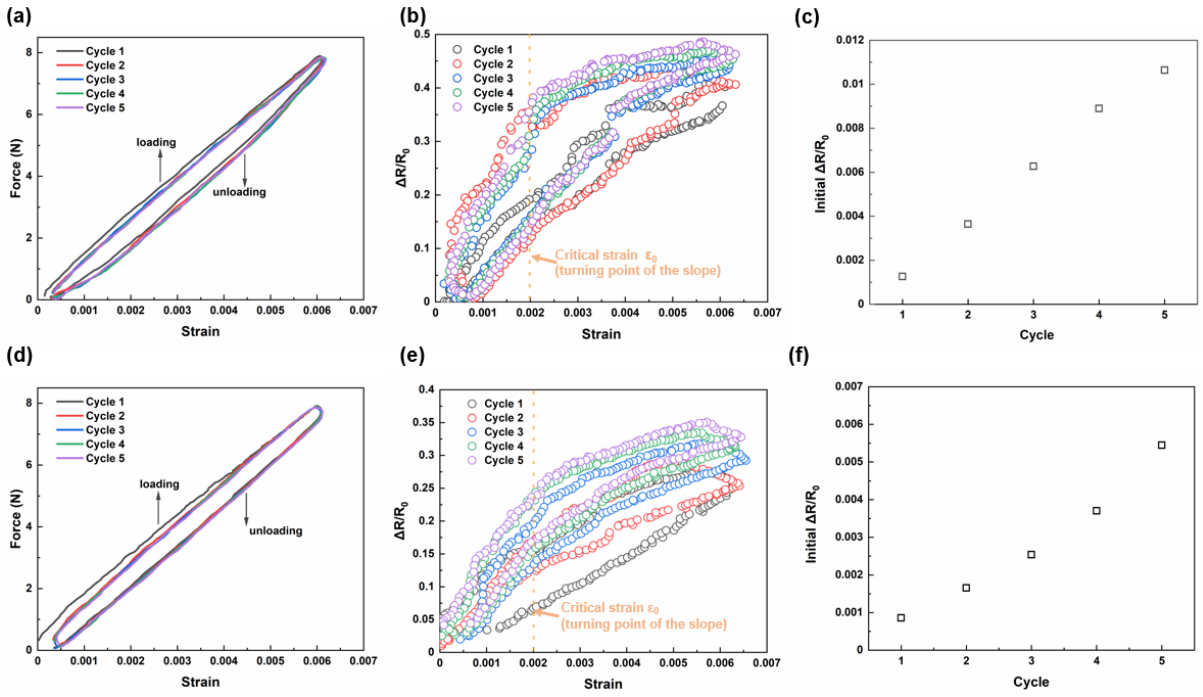

Figure 4.7 The cyclic tensile test response for 3 and 4 mm wide LIG samples up to 8 kN for 5 load cycles. The applied force versus strain for LIG channels of (a) 3mm-width, (d) 4mm-width. The cyclic tensile test electrical resistance response for the (b) 3 mm wide and (e) 4mm wide

LIG sample at 8000 N. The initial strain and resistance at the beginning of each cycle for the (c) 3 mm-width and (f) 4 mm-width.

4.3.3 In-situ strain sensing during monotonic tensile test

All the six composite samples in **Table 4.1** were subjected to monotonic tensile loading up to a high load of 20 kN (or 1.8% strain) after the low-load and moderate-load cyclic loading, except for Sample 6 which has no prior cyclic loading history. This allows assessment of sensing performance and reusability of the LIG samples at high loads before ultimate failure point after they have experienced low and moderate loading. The scatter plot in **Figure 4.8** presents the relative change in electrical resistance ($\Delta R/R_0$) measurement as a function of applied strain for all six samples. The reference electrical resistance R_0 was reset using the electrical resistance of the samples after the cyclic loading but before the monotonic tensile loading. A few key observations can be made from **Figure 4.8**. Firstly, the general trend of resistance variation exhibits a non-linear quadratic relationship with applied strain, with higher sensing sensitivity at higher strain. This is attributed to more intensive damage being developed in the LIG network at high load, which significantly reduces the conductivity of the LIG. Secondly, regardless of the previous loading history, there is good repeatability in sensing performance between the samples with the same LIG channel width at high load.

This is because the initial damage developed at low or moderate load was overshadowed by the more intensive damage developed at high load, which has a dominating effect on the sensor sensitivity. Thirdly, the sensitivity of the LIG is affected by the width of the LIG channel, with a narrower LIG channel being more sensitive to applied strain at high load. It again highlights the strong influence of damage development and crack density at high load on a narrower LIG channel. The effect is particularly pronounced for the LIG channel width of 3 mm whose data get noisier at high load. A simple phenomenological model is developed in the next section to describe the piezoresistivity of LIG sensor of different width as a function of applied strain.

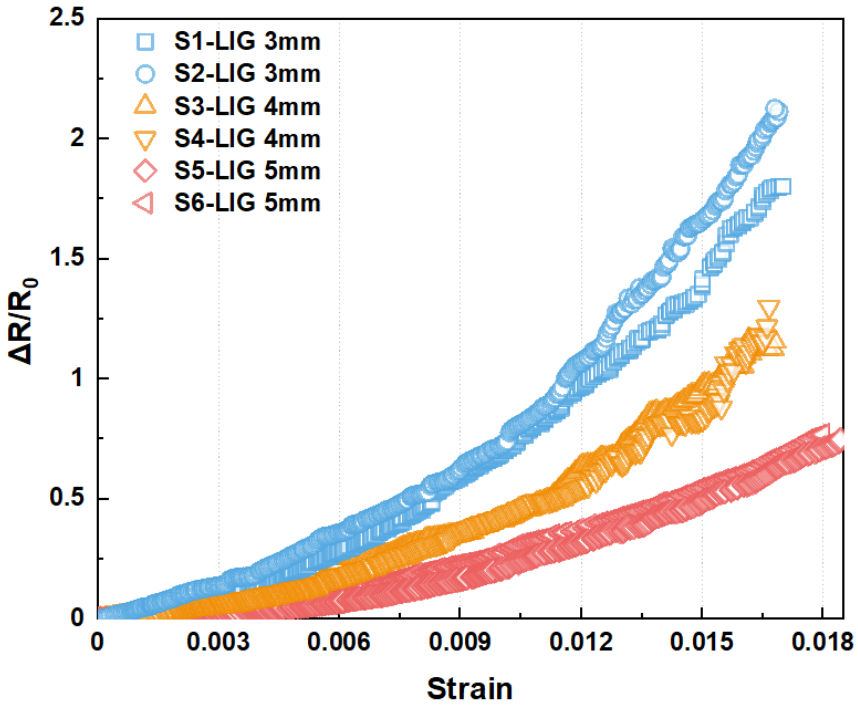

Figure 4.8 The electrical resistance changes versus applied strain for all samples with LIG channel widths of 3 mm, 4 mm and 5 mm under monotonic tensile loading.

4.3.4 Modelling of piezoresistive LIG sensors of different widths

4.3.4.1 Mechanism of piezoresistive LIG strain sensor

Despite the simplicity of the LIG pattern geometry employed in the tensile test, the combination of the geometrical change of the LIG following the host composite and the resulting development of microcracks in the LIG structure poses a complex modeling challenge. In previous studies, percolation theory and effective medium approximations were commonly employed to elucidate the interplay of microcracks, volume deformation, and electrical conductivity [96, 97]. The coupled piezoresistive behaviour results from the fact that the electrical conductivity and geometric change of the material are directly influenced by each other. For instance, elongation causes the percolation threshold to rise, which causes the electrical conductivity to drop more quickly[98]. The percolation threshold is defined as the critical concentration of conductive particles in the composite matrix where a continuous conductive path emerges. Near this threshold, the localized conductive paths form without spanning the entire material, leading to intermediate conductivity.

In this study, the behaviour of a porous graphene network under strain is explained using a combined random void model and percolation pathway framework[99]. The development of microcracks can be considered as strain-induced voids in a deformed volume, and can be

described by the Weibull distribution [99, 100]. Below the critical strain 0.2% as shown in **Figure 4.3**, the majority of LIG network maintains its conductive pathways. Any microcracks or voids that have formed remain sparse, causing only a gradual linear increase in resistivity with applied strain. Beyond the critical strain 0.2%, the density of voids and cracks increases significantly, disrupting the percolation pathways and leading to a quick rise in resistivity. The LIG network transitions to a state where the conductive pathways are increasingly fragmented [101] .Therefore, the piezoresistivity relationship becomes dominated by the exponential growth of void density at high load which follows the Weibull distribution [102]. In the following, a simplified phenomenological model is proposed to describe the piezoresistivity of LIG under applied strain, considering the geometrical change of the LIG and the Weibull distribution of strain-induced defects or microcracks.

4.3.4.2 Geometry of LIG and random void model

For the geometric part, it is assumed that the porous LIG infiltrated with epoxy resin is a homogeneous material having a rectangular cross-section with a width of C and a thickness of D. The dimensions of the LIG-cork-epoxy model are shown in **Figure 4.9 a**. Considering the Poisson's effect, there is contraction of the material in the transverse directions (i.e. ΔC in the channel width direction and ΔD in thickness direction) when it is loaded in tension in the longitudinal direction, as related by the Poisson's ratio v:

$$\frac{\Delta C}{C} = \frac{\Delta D}{D} = -v\varepsilon \qquad \text{Equation 4.3}$$

The total unloaded cross-sectional area of the LIG channel is given by S = *2C*×*D*. Following the applied longitudinal strain, ε, the new cross-sectional area *S(ε)* as be written as a function of ε:

$$S(\varepsilon) = 2C \times (1 - v\varepsilon) \times D \times (1 - v\varepsilon) = S(1 - v\varepsilon)^2 \qquad \text{Equation 4.4}$$

while the new length *L(ε)* of the LIG channel is:

$$L(\varepsilon) = L(1 + \varepsilon) \qquad \text{Equation 4.5}$$

where L is the unloaded length of the LIG channel (L = 120 mm is a fixed parameter in this study). An assumption is made that only the channels that went through the second lasing (dark grey region in **Figure 4.9 a**) are conductive. This assumption is justifiable due to the substantial reduction in sheet resistance from MΩ/sq to kΩ/sq following the second lasing. The non-dimensional width-to-length ratio C_w for the LIG channels is defined by:

$$C_w = \frac{2C}{L} \qquad \text{Equation 4.6}$$

For the electrical resistivity part, the LIG exhibits a pronounced piezoresistive effect, as evidenced by its high gauge factor (GF) value. This indicates that the effective resistivity of the LIG is highly sensitive to applied strain, undergoing significant changes in response to mechanical deformation. It is assumed that the LIG channels are very thin in thickness compared to the cork substrate that they do not affect the overall structural integrity of the cork substrate nor the composite as a whole. Regardless of the LIG channel width, the LIG-cork layers in all the composite samples have the same strength and therefore have the same initial defect density and distribution. As the epoxy resin forms a continuous matrix that infiltrate the porous cork-LIG substrate and the resin has significantly higher stiffness than cork, it governs the overall mechanical response [103]. Upon further loading, the damage or microcracks propagate in the cork substrate at the same rate and cut through the conductive LIG network, changing the effective resistivity of the LIG. As depicted in **Figure 4.9 b**, a constant damage or crack density growth rate has a detrimental effect on the LIG channel with a smaller width as the proportion of intact LIG network over the channel width is reduced. Without considering the quantum effects and to reduce the number of variables, the resistivity of the LIG channel under strain is modelled simply based on the exponential relationship between crack density and strain, as described by the Weibull distribution [102]. The resistivity of the LIG channel is also proposed to be inversely proportional to the square of width-to-length ratio. Therefore, the resistivity ρ_ε of the LIG under applied strain ε can be expressed as follows:

$$\frac{\rho_\varepsilon}{\rho_0} = \frac{A\varepsilon}{C_w{}^2\left(\exp\left(-\frac{\varepsilon}{\varepsilon_0}\right)^t\right)} + 1 \qquad \text{Equation 4.7}$$

where ρ_0 represent the unloaded initial resistivity of the LIG. ε_0 is the characteristic or reference strain of the material, and in this case, it is taken as the critical strain of the LIG when the material damage starts to have a significant effect on the resistivity, which can be determined from the knee of the $\Delta R/R_0 - \varepsilon$ curves in **Figure 4.7**. A and t are non-dimensional material-specific parameters related to the combined electromechanical properties of the composite matrix and the LIG network, which are associated with the LIG network structure, the initial defect density in the material, the crack growth rate in the material and their influence on material's conductivity. The numerical value of t is typically close to 1, but within the range of 1 to 2 [104].

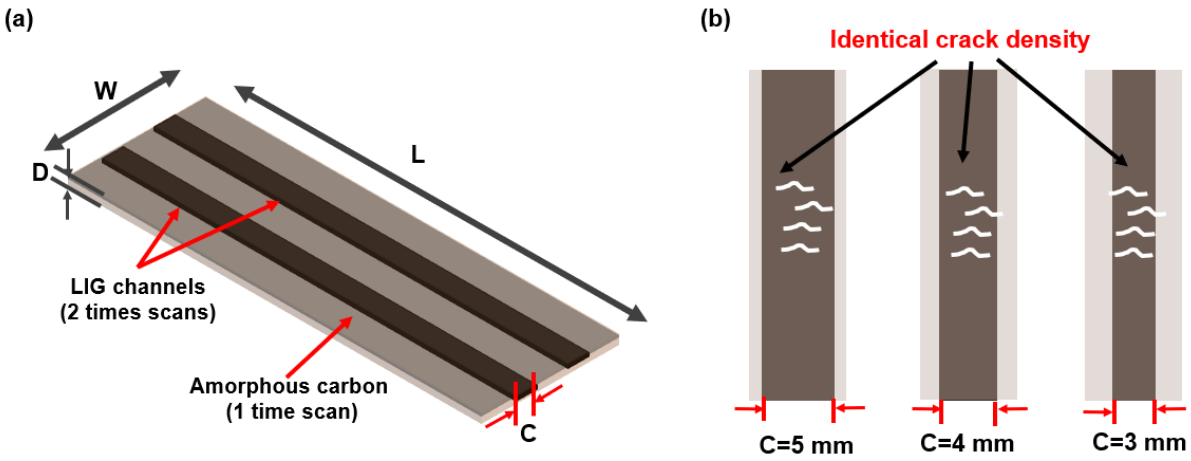

Figure 4.9 (a) Dimensions of the LIG-cork layer in the sandwich composite. (b) A schematic illustrating the effect of identical crack conditions on different LIG channel widths.

The initial electrical resistance of an unstrained material is given by the classical electrical resistance equation:

$$R_0 = \rho_0 \frac{L}{S} \qquad \text{Equation 4.8}$$

If the material is piezoresistive, taking into account both geometric changes and strain-induced damage in the material, its electrical resistance can be rewritten as a function of ε:

$$R(\varepsilon) = \rho(\varepsilon) \frac{L(\varepsilon)}{S(\varepsilon)} \qquad \text{Equation 4.9}$$

Combining Equation 4.7 to Equation 4.9 on the geometric and resistivity change, the relative change in electrical resistance of the LIG becomes:

$$\frac{\Delta R}{R_0} = \frac{R(\varepsilon) - R_0}{R_0} = \left(\frac{A\varepsilon}{{C_w}^2 \left(\exp\left(-\frac{\varepsilon}{\varepsilon_0} \right)^t \right)} + 1 \right) \times \left[\frac{1+\varepsilon}{(1-v\varepsilon)^2} \right] - 1 \qquad \text{Equation 4.10}$$

When the applied strain ε is small (it is smaller than 0.02 in this study), by applying the Taylor series expansion and neglecting the higher-order terms, Equation 4.10 can be simplified into a quadratic function of ε:

$$\frac{\Delta R}{R_0} = \left(\frac{A}{{C_w}^2} + 2v + 1 \right) \varepsilon + \left(\frac{At}{\varepsilon_0 {C_w}^2} + \frac{(2v+1)A}{{C_w}^2} + 3v^2 + 2v \right) \varepsilon^2 + O(\varepsilon^3) \qquad \text{Equation 4.11}$$

The porous LIG network is fragile and has negligible stiffness. Since the voids in the LIG structure and the cork substrate are infiltrated with epoxy resin, the LIG-cork layer is assumed to share the same mechanical properties as the epoxy resin. In the above quadratic equation, v is taken to be that of the epoxy resin (v = 0.38). The material constant A and t can be determined empirically by fitting this quadratic equation to the experimental results using a generic optimization algorithm.

4.3.4.3 Model fitting with experimental data

The experimental dataset of the two samples with LIG channel width of 4 mm (C_w = 1/15) was used to find the best-fit parameters for A and t. The R-squared value was employed as the metric to evaluate how well the model fits the experimental data. Following the grid search method [83] by maximizing the average mean coefficients of determination, A and t are found to be 0.0284 and 1.06 respectively, with high R-squared values above 0.98.

For independent validation purposes, the parameters are reused in Equation 4.11 to plot against the datasets of samples with LIG channel widths of 3 mm (C_w = 1/20) and 5 mm (C_w = 1/12), as shown in **Figure 4.10**. The averaged R-squared values obtained for the samples with LIG channel widths of 3 mm and 5 mm are above 0.95, showing a good description of the experimental data. These high R-squared values substantiate the suitability of the quadratic approximation for capturing the resistance change as a function of applied strain and the LIG channel width.

The resistance change model above the critical threshold (0.2% strain) cannot be applied to strains below as defect growth is negligible in this range. At these low strains (0 tp 0.2% strain), the piezoresistive response remains predominantly linear, as shown in **Figure 4.3**. This research excluded this strain range from analysis because the composites do not experience failure at such minimal deformation, making strain monitoring below 0.2% strain unnecessary. The proposed phenomenological model can be used to estimate the strain-sensing sensitivity of LIG with different width-to-length ratios, especially for strain values above 0.2% where the response is highly non-linear and the influence of damage development in the LIG becomes significant. The model can serve as an essential sensor design tool for calibrating the LIG sensors and inform the design of LIG sensor whose gauge factor can be tailored for various applications by simply modifying the LIG sensor geometry.

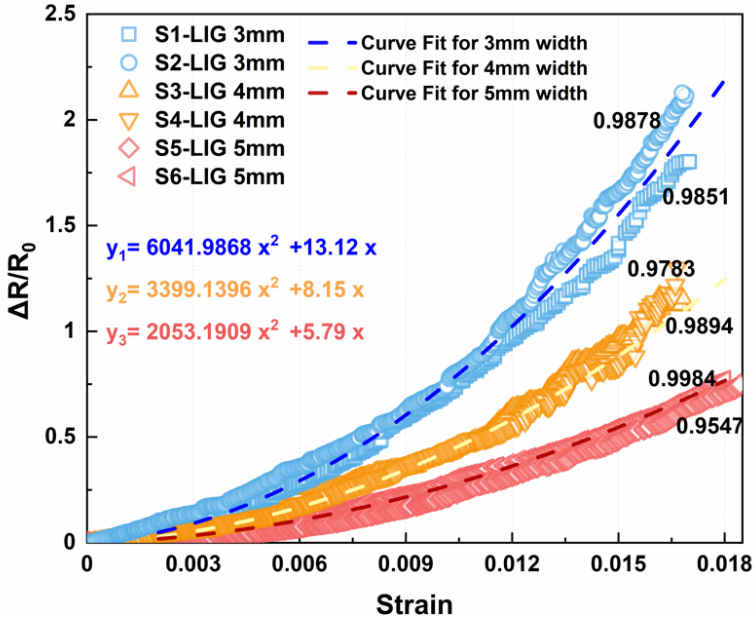

Figure 4.10 The curve fitting result for electrical resistance changes versus applied strain with LIG channel widths of 3 mm, 4 mm and 5 mm. The experimental data is represented in a scatter plot, with the curve fitting depicted by dotted lines. The numerical value next to each dataset shows the corresponding R-squared value of the curve fitting.

4.4 Summary

This chapter investigates the piezoresistivity of a cork-derived LIG of different widths when embedded within a glass fibre reinforced composite. The LIG is cheap to synthesise and it can be easily integrated with conventional composite manufacturing processes such as a prepreg system in vacuum bagging and autoclave. The finding in this work demonstrates the potential for LIG to be used as a low-cost and functional strain sensor up to 1.8% strain, which is near to the failure strain of most fibre-reinforced composites (around 2%). The electrical resistance of the LIG was measured as the monitoring parameter using an inexpensive digital multimeter and its changes were tracked as a function of applied strain. The following concluding remarks can be made:

(1) For low-load cyclic tensile loading (up to 0.08% strain for 5 cycles), the LIG exhibited stable and consistent electrical responses where its electrical resistance varies linearly with applied strain. The effect of piezoresistivity was more pronounced (i.e. more sensitive to strain) for a narrow LIG channel, but it is less responsive in time compared to a wider LIG channel. It demonstrates its capability to measure small strains, with a higher gauge factor of around 50-133 in contrast to conventional metallic strain gauges. The intrinsic viscoelastic characteristics of epoxy composites result in a slightly delayed response in electrical resistance measurements. No significant physical change or damage in the LIG conductive network was observed.

(2) For moderate-load cyclic tensile loading (up to 0.7% strain for 5 cycles), the $\Delta R/R_0 - \varepsilon$ curves showed a bilinear relationship, with a knee at 0.2% strain signifying the onset of physical change or damage in the LIG network. The damage accumulated after each load cycle, which altered the piezoresistivity of the LIG. However, no damage is detected in the host composite.

(3) For monotonic tensile loading (up to 1.8% strain), the damage development in the LIG network plays an important role in its piezoresistivity, especially for strain higher than 0.7%. The piezoresistivity can be approximated using a quadratic function, which can be derived using a model of random voids with a Weibull distribution. The model enables the prediction of piezoresistivity of LIG as a function of its geometry and the applied strain, which can serve as a useful tool for the design of LIG strain sensors for structural health monitoring.

Chapter 5 Paper-derived LIG as a surface strain sensor

This chapter investigates the strain sensing performance of LIG when positioned on the surface of the host composite. The LIG was synthesised on a brown paper substrate pre-attached on the composite surface following the resin infusion process. The characterization of the LIG microstructure and its electrical properties are firstly evaluated. By subjecting the samples to four-point bending, the strain sensing performance of the LIG sensor in tension and compression are separately assessed.

5.1 Introduction

Resistance strain gauges, typically constructed from metallic foil, have been applied on the composite surface for strain measurement. This method offers a standardized, straightforward, and reliable approach, making it a widely adopted non-destructive technique in industry. They are capable of measuring minute changes in resistance corresponding to strain but require connection to external instrumentation amplification such as a Wheatstone bridge. External strain gauges also require meticulous manual surface preparation for bonding to the host material and are susceptible to debonding after long-term usage due to adhesive degradation failure.

To address the aforementioned limitations of strain gauges, the integration of conductive nanoparticles, particularly graphene-based materials, provides a promising solution. Their direct integration into composites eliminates the need for external bonding and reduces reliance on skill-dependent manual labour [105]. Prior studies have shown that uniform dispersion of graphene within the matrix facilitates the formation of an efficient conductive network and provides effective strain response [12]. The advent of LIG technology introduces a novel methodology for directly patterning customized graphene geometries onto composite surfaces, instead of adding graphene nanoparticles within the matrix to form conductive network for strain and damage detection [106]. This innovation enables the fabrication of smart sensing composites at reduced costs by eliminating the necessity for uniform nanoparticles dispersion [106] which is challenging to achieve via physical or chemical dispersion processes. Secondly, LIG strain sensors on composite surfaces also offer exceptional design flexibility due to the direct laser conversion process, enabling seamless integration even on surfaces of complex geometry without additional bonding. Furthermore, LIG on the composite surface opens possibilities for environmental sensing, such as moisture or chemical detection, offering the potential to develop multifunctional smart sensing composites. This capability enhances the versatility and application scope of LIG-integrated materials.

In this chapter, a novel one-step laser patterning on post-cure epoxy resin composite plates to synthesise LIG is presented. It demonstrates an alternative LIG sensor synthesis process on resin infused composite using dry fibre reinforcement fabrics, another common composite manufacturing process which is different from the one described in Chapter 3 and 4 using composite prepregs. The brown paper substrate was selected due to its higher laser energy absorption efficiency and lower reflectivity compared to white [107]. Brown paper was used as the LIG substrate precursor which was laid down on the top and bottom surfaces of the reinforcement fibre sheets before the resin infusion. By printing a thin layer of LIG on the composite surface, the structural integrity of the composite laminate is unaffected. The laser parameters for achieving high-quality LIG with desirable conductivity were determined through systematic structural and morphological characterizations. The performance of LIG as a surface strain sensor on the host composite was assessed using four-point bending. The four-point bending test was chosen over the uniaxial tensile test discussed in Chapter 4, as it allows the application of tensile and compressive strain using the same specimen geometry and test fixture. The required specimen size is also smaller, allowing more test samples to be prepared from the same composite laminate for in-depth investigation. A simple physical model was developed based on the elongation of LIG line pattern gaps, which act as self-organized microcracks and are governed by the connection and disconnection states of the LIG network.

5.2 Experiment

5.2.1 Composite fabrication

The composite plate utilised in this research was fabricated using the vacuum bagging infusion (VBI) method. Ten layers of plain-weave E-class glass fibre sheet ((areal density 270 g/m^2, ply thickness 0.2 mm) were laid up with two sheets of brown paper (0.15mm, thickness) added as the top and bottom surfaces to achieve a symmetrical lay-up. A symmetrical composite lay-up is essential to avoid laminate bending upon cooling down after the exothermic resin curing process. The configuration of the plates and the VBI method is illustrated in **Figure 5.1 a**. Epoxy resin (EpoxAmite) with 103 slow hardener having a 100:29 weight ratio of components A and B in a vacuum bag. The natural lignin fibres in the brown paper are permeable to epoxy resin. Hence the brown paper was easily wet through by the epoxy resin and integrated well with the rest of the composite plate during the resin infusion process. The entire plate was left to cure at room temperature (approximately 25°C) for 24 hours, allowing the epoxy resin to polymerize and solidify. After curing, the vacuum bag was removed, and the composite plate was cut to the required dimension for bending test. The thickness of the cured plate was 2.3 $\pm$ 0.05 mm.

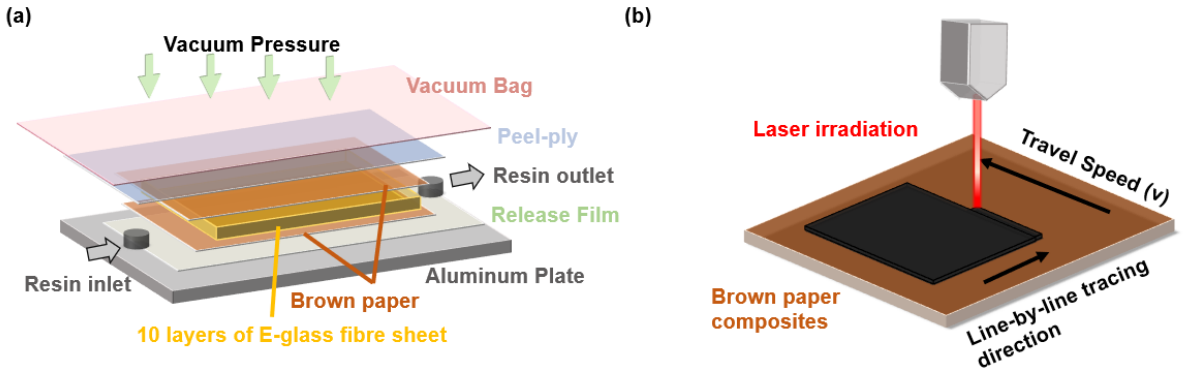

Figure 5.1 (a) The schematic of the brown paper composite fabrication process and layup. (b) The direct LIG synthesis on the brown paper on the surface of composite.

5.2.2 LIG synthesis and characterisation

Before laser treatment, the composite surface was wiped with isopropyl alcohol and dried at room temperature. The laser irradiation on the brown paper on the composite surface was processed by a commercial CO_2 laser engraver unit (ShenHui, G690) with a power range from 8 to 12 W and an engraving speed range from 20 mm/s to 80mm/s. The laser system employed in this chapter differs from the previous chapter, as the experiment required a higher power output. The epoxy resin layer coats the upper surface of the paper substrate, requiring higher energy to penetrate and debond its chemical bonds compared to untreated natural materials. The resin-infused brown paper offers the flame-retardant properties necessary for laser irradiation which is not available in dry brown paper. The laser irradiation was performed unidirectionally line by line, with a line gap of 0.2 mm and a laser pulse per unit area of 400 dot per inch (dpi). The communication between the laser unit and the PC is done via the RDwork V.8 control software. The first-time lasing was set at a default focus length of 6.75 mm of the laser engraver. Previous research has shown that multiple times lasing and the z-axis defocus technique improve the capability of the precursor to transition from amorphous carbon to a graphite structure [76]. The defocusing method fixing the focus height at 2.4 mm was employed for the subsequent laser scanning. **Figure 5.1 b** illustrates the LIG synthesis on the composite surfaces. It should be noted that variation in the power, speed and focus distance can be used to adjust the microstructure and electrical conductivity of the resulting LIG patterns. In this study, only two parameters for LIG synthesis were investigated, i.e. laser power and scanning speed.

To determine the optimal laser parameters for subsequent LIG pattern design, the morphology and electrical characteristics of the LIG were firstly investigated. Square-shaped (10 mm× 10 mm) LIG patterns were lased for sheet resistance measurement and characterization. All laser treatments were processed under normal room conditions. Silver conductive paint was applied on the opposite edges of the LIG pattern to facilitate copper wire connection for electrical

resistance measurement. The surface resistance of the LIG electrodes was measured by a digital multimeter (Keysight, 2110) after built the silver paint connections to prevent disruption of the delicate LIG structure. The cross-section morphology was observed by an optical microscope. The surface microstructure of LIG was investigated via field emission scanning electron microscopy (SEM, HITACHI SU8000). Horiba LabRAM Soleil Raman spectroscope was employed with a 532 nm excitation laser to determine the carbonization and defect level of the LIG.

5.2.3 Cyclic and monotonic strain sensing setup

The optimal lasing parameters determined in Section 5.2.2 were used to fabricate composite samples for subsequent four-point bending tests. Nineteen straight-edged samples of dimension 18×100 mm was cut from the composite plate fabricated in Section 5.2.1. Three distinct LIG geometries of the same width but different lengths were engraved in the centre of these samples, i.e. 8×8 mm, 8×16 mm, and 8×24 mm, as depicted in **Figure 5.2 a**. **Figure 5.2 b** gives comparison of the orientation configurations for both the paper-derived LIG sensors presented in this chapter and the cork-derived LIG sensors from Chapter 4. Transversely engraved LIG means the LIG is engraved line-by-line perpendicular to the direction of the mechanical straining. The longitudinal engraved LIG means the LIG is engraved line-by-line in the same direction as the mechanical straining. The 2-point method was chosen for LIG electrical resistance measurement of the LIG due to the relatively low contact resistance (on the order of around 100 Ω) compared to the high resistance of the embedded LIG (3 to11 kΩ). After the laser treatment, UV resin (Ning, AMA-Glue) was applied to the LIG surface to function as a protective encapsulation layer. The UV resin was cured after 60 seconds of UV irradiation and encapsulated the LIG fragile microstructure, preventing the LIG from detaching from the composite surface.

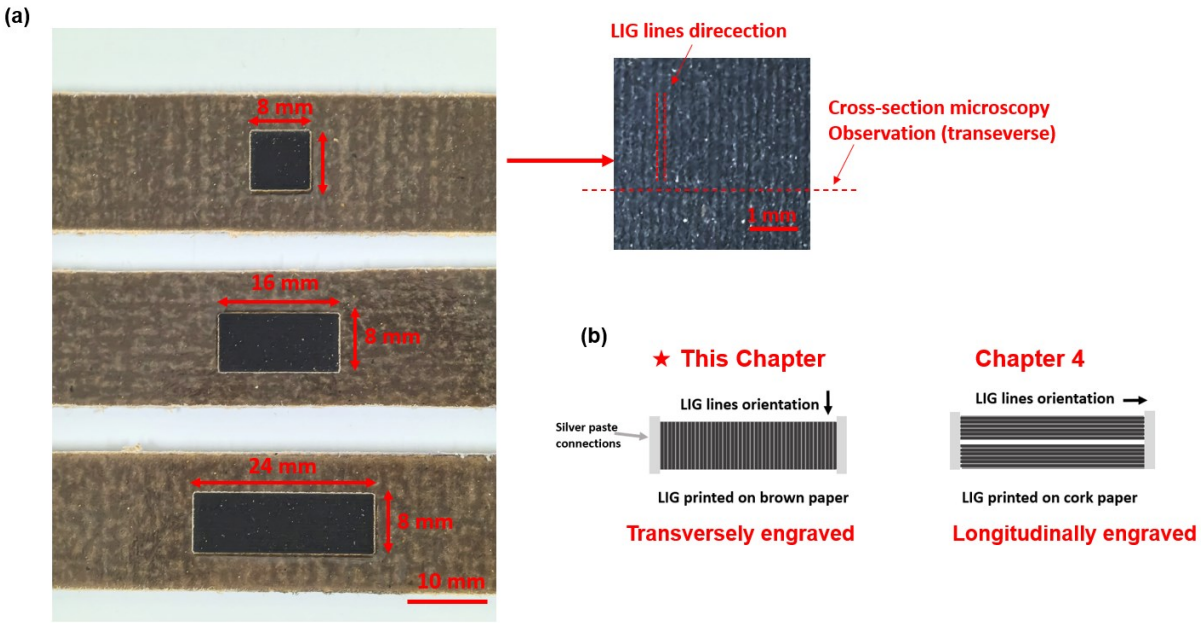

Figure 5.2 The dimensions of the LIG printed on the surface of brown paper composites. (a) Three different dimensions have been shown with the zoom in LIG printed transversely. (b) The comparison of orientations for paper-derived LIG and cork-derived LIG.

All the bending test samples were loaded in the load-controlled mode using the four-point bending test fixture mounted on the universal testing machine (SHIMADZU AGX-V50kN, with a 50 kN load cell). **Figure 5.3** illustrates the schematic of the four-point bending test setup subjecting the LIG on the surface to tensile strain if it is on the supporting side of the sample, and compressive strain if it is on the loading side of the sample. The separation distance of the support rollers was 70 mm, while the distance between the loading rollers was 35 mm. The samples were subjected to the cyclic and monotonic four-point bending load following the loading history shown in **Table 5.1**. The bending tests conducted were divided into three test groups. There were at least 2 samples being repeated for each test within the test groups. Test Group 1 investigated the difference in sensing performance of the LIG for tensile and compressive strain under cyclic bending at low strain (up to about 0.6%). Due to the fragile nature of the LIG sample surface, flipping it to print on the opposite side for compression sensing would compromise the structural integrity of the LIG; therefore, the compression and tension response are not measured on the same sample. Test Group 2 investigated the effect of LIG length on its sensing performance for tensile strain under cyclic bending at low strain (up to about 0.6%). Note that the samples S8, S9 and S10 in Test Group 2 had the same LIG geometry and were subjected to the same cyclic loading as the samples S1 and S2 in Test Group 1. They were remanufactured so that their lasing and testing could be run together with the rest of samples in Test Group 2 on the same day (i.e. one day for lasing and encapsulation and the next day for cyclic bending testing) in order to eliminate external factors such as material aging when comparing the results. All cyclic tests of samples in Group 1 and 2 were conducted for 10 cycles up to 200 N or strain about 0.6%), which was approximately 35% of the ultimate failure load of the samples. Lastly, Test Group 3 looked into the sensing performance of the LIG sensor for monotonic tensile strain up to the ultimate failure of the samples. Before testing, a preconditioning cycle up to 200 N (same magnitude as the subsequent cyclic load) was implemented for all cyclic tests to facilitate the removal of irregularities and stabilisation of the internal structure of the LIG, the electrical resistance after preloading was measured to be used as the initial electrical resistance values. For monotonic bending tests, two preload cycles were applied up to 150 N—a lower load than that used in cyclic testing to prevent microdamage to the LIG structure. The same crosshead displacement rate of 1 mm/min was applied for all tests, including loading and unloading.

During loading, the electrical resistance reading was recorded by a digital multimeter (Keysight, 2110), a small current of 10 μA was applied by the multimeter to ensure no significant Joule heating in the LIG. The KI-tool software at the sampling rate of 10 Hz, synchronised with the load

data acquired by the universal testing machine using the time stamp provided by the PCs. In four-point bending, the region of samples between the loading rollers experiences uniform bending moment. The strain(ε) seen by the LIG on the surface of the sample is uniform as well and assumed to follow equation 5.1:

$$\varepsilon = \frac{\sigma}{E} = \frac{3F(L_l - L_u)}{2bd^2E} \qquad \text{Equation 5.1}$$

Where F is the applied load, L_l and L_s represent the loading and support span lengths, respectively, while b and d denote the sample width and thickness. The flexural modulus E was determined via a three-point bending test using a spare specimen, following the standard bending equation:

$$E = \frac{FL^3}{4bd^3\delta} \qquad \text{Equation 5.2}$$

Where F, L, b, and d retain the above defined meanings, and δ represents the midspan deflection distance.

Table 5.1 Test matrix showing the geometry and loading history for all samples in three test Groups.

Test group	**Sample no.**	**LIG dimension, length × width (mm)**	**Length-to-width ratio**	**Mechanical loading (same loading speed for all test at 1mm/min)**
Group 1	S1, S2	16 × 8	2:1	Preloading 1 cycle(200N)→ cyclic loading to 200 N (10 cycles) - tension
	S3, S4			Preloading 1 cycle (200N)→ cyclic loading to 200 N (10 cycles) - compression
Group 2	S5, S6, S7	8 × 8	1:1	Preloading 1 cycle (200N)→ cyclic loading to 200N (10 cycles) - tension
	S8, S9, S10	16 × 8	2:1	Preloading 1 cycle (200N)→ cyclic loading to 200N (10 cycles) - tension
	S11, S12, S13	24 × 8	3:1	Preloading 1 cycle (200N)→ cyclic loading to 200N (10 cycles) - tension
Group 3	S14, S15	8 × 8	1:1	Preloading 2 cycles (150N) → monotonic loading to failure
	S16, S17	16 × 8	2:1	
	S18, S19	24 × 8	3:1	

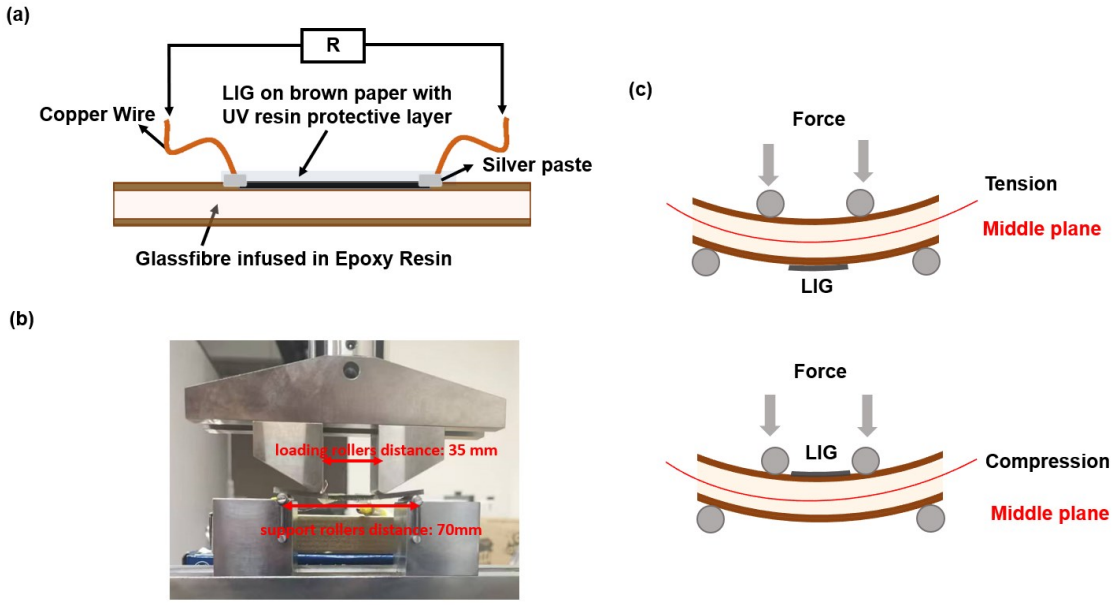

Figure 5.3 A composite sample with LIG on the surface in a four-point bending test. (a) The 2-point electrical connections for in-situ resistance measurement. (b) The four-point bending test fixture. (c) The strain (tensile or compressive) seen by the surface LIG sensor is determined by how it is position in the four-point bending.

5.3 Results and discussion

5.3.1 Characterization of paper-derived LIG

The characterisation of paper-derived LIG can be divided into structural and morphological analyses. Prior to detailed spectrometry characterisation, visual observation was made to narrow down the range of lasing power and speed being investigated. Insufficient power (lower than 8 W) fails to induce carbonization, while excessive power (higher than 12 W) makes the LIG too flaky and it easily peels off from the brown paper surface layer. **Figure 5.4** illustrates the LIG quality after 1 to 3 laser scans at power energy between 8 W and 12 W taken using a high-resolution camera. The results indicate that, compared to a single scan, a second scan enhances carbonization, yielding a darker and more uniform LIG structure. However, a third scan leads to LIG exfoliation due to weakened adhesion between the LIG and the brown paper substrate after further carbonization. It could be easily blown away by the cooling fan in the laser head module, exposing the underlying glass fibre woven texture. Consequently, a two-time laser scan was found to be optimal and was selected for subsequent investigation.

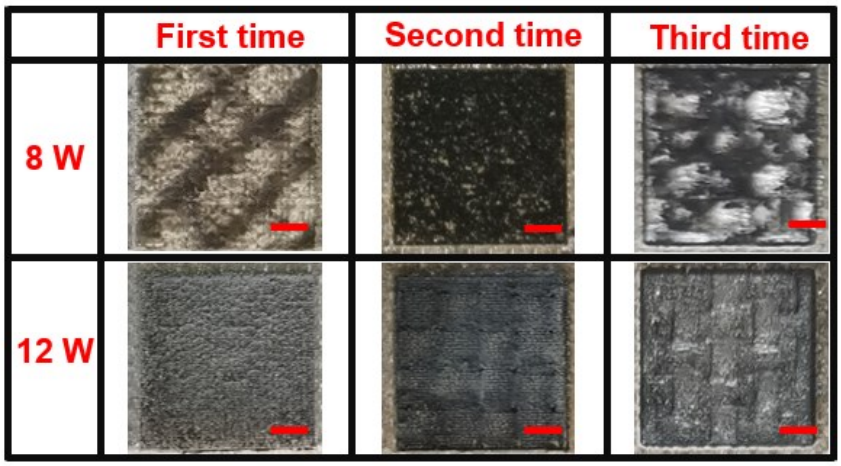

Figure 5.4 Photographs showing the appearance of LIG on the surface of the composite after laser treatment following 1 to 3 lasing scans at minimum power 8 W and maximum power 12 W (scale bar equal to 2 mm).

For further comparative analysis of the LIG quality, a quantitative parameter is introduced combining laser power and lasing speed. Line Energy Density (LED) is a crucial parameter in laser processing, defined as the ratio between laser power and lasing speed which indicates the amount of laser energy deposited per unit length along the path of the laser beam as follows:

$$\text{LED } (J/mm) = \frac{Laser\ Power\ (W)}{lasing\ Speed\ (mm/s)} \qquad \text{Equation 5.3}$$

Using LED value as an indicator for line-by-line printed LIG synthesis allows for the systematic study of the relationship between energy input and process outcomes. This equation differs from Chapter 3 because the laser defocusing method was employed in this chapter, requiring calculation of line energy density rather than area energy density. This adjustment is required because defocusing alters the laser's focal radius, consequently changing the irradiation area. **Figure 5.5 a** displays the LED for all combinations of laser speed and power within the preset range. Laser parameters within the green outlined region consistently generate dark grey graphitic structures with minimal visible defects which shown as reduced exposure of the underlying brown paper substrate. **Figure 5.5 b** illustrates the empirical relationship between sheet resistance and LED values. The average sheet resistance was obtained by averaging readings for three different samples under the same laser configuration. Overall, the sheet resistance of the LIG is inversely proportional to LED, or it can be described as an exponential decay with LED. This correlation indicates that at low LED values (below 0.15 J/mm), small increases in LED result in substantial reductions in resistivity. However, as LED values increased beyond 0.16 J/mm, the improvement in electrical conductivity became less pronounced and reached an asymptotic value. The large uncertainty or error bar at LED = 0.2 J/mm is attributed to the high power at 12 W power that penetrates deeper into brown paper causing the LIG to easily detach from the

composites compared to the lower power setting. Higher laser power induces LIG detachment from the glass fibre composite substrate, causing instability. This occurs because elevated energy generates a thicker layer of fragile LIG which penetrate the whole paper layer, resulting in increased electrical resistance fluctuations. The large error bars reflect this resistance variability. However, at 0.2 J/mm in **Figure 5.5 b**, no significant resistance change was observed, as the values represent averaged measurements from nine samples processed at 8, 10, and 12 W with varying laser speeds. The weak LIG-substrate adhesion becomes particularly evident at higher LED energy densities (0.2 J/mm). For instance, samples processed at 60 mm/s with 12 W power show greater electrical resistance variations compared to those processed at 50 mm/s with 10 W power. This demonstrates that higher lasing speeds at equivalent energy densities increase the likelihood of LIG delamination. As a result, the ideal range of LED that can generate LIG with consistent electrical conductivity for strain sensing is between, 0.16 J/mm to 2 J/mm.

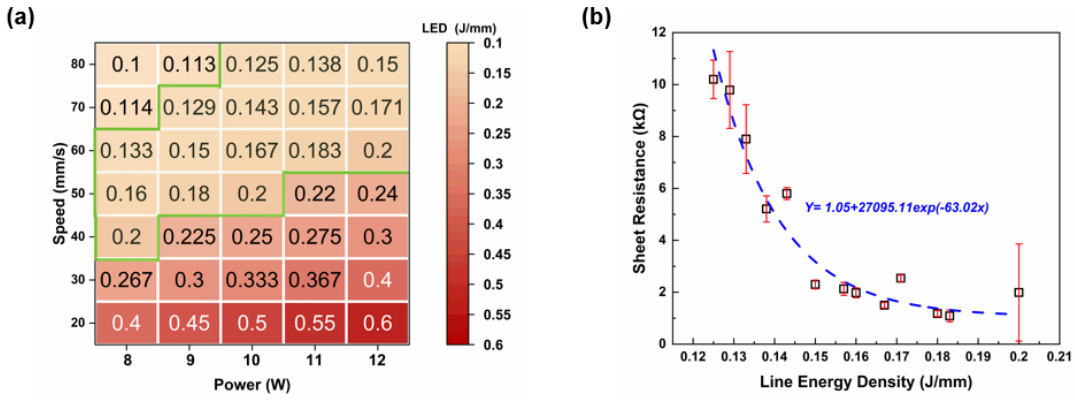

Figure 5.5 (a) The lasing energy density map as a function of lasing power and speed. (b) The sheet resistance measurement of LIG having an exponential decay with LED.

To refine the optimal LIG laser parameters from the previously identified range of LED values, Raman spectroscopy and SEM characterization were performed across five distinct LED values.

5.3.1.1 Raman spectroscopy

Raman spectroscopy is an indispensable approach for identifying and analysing the structure of all graphitic materials. The intensity ratio of D peak and G peak reflects defects or disorder in the resultant graphene structure. The Raman spectra were not collected for the epoxy resin substrate in this study, as previous research has already established its flat spectral baseline without characteristic peaks [108].Within the LED value range from 0.125 to 0.2 J/mm, five samples were selected at regular intervals for Raman spectroscopy. **Figure 5.6 a** compares the five representative Raman spectra of LIG samples after two-time lasing and **Figure 5.6 b** show the intensity peaks' ratios of different laser LED values. Both the lowest intensity of I_D/I_G ratio and the highest intensity of I_{2D}/I_G ratio are achieved at LED= 0.167 J/mm, which indicate the creation of the

least structural defect and less stacking order of graphene materials among the five samples. As the LED reaches 0.18 J/mm, more structural defects appear which can be read from the increasing I_D/I_G ratio, demonstrating that higher LED does not continuously enhance the quality of LIG when the energy reach ideal stage. Consequently, the optimal LED value was found to be between 0.16 and 0.18 J/mm.

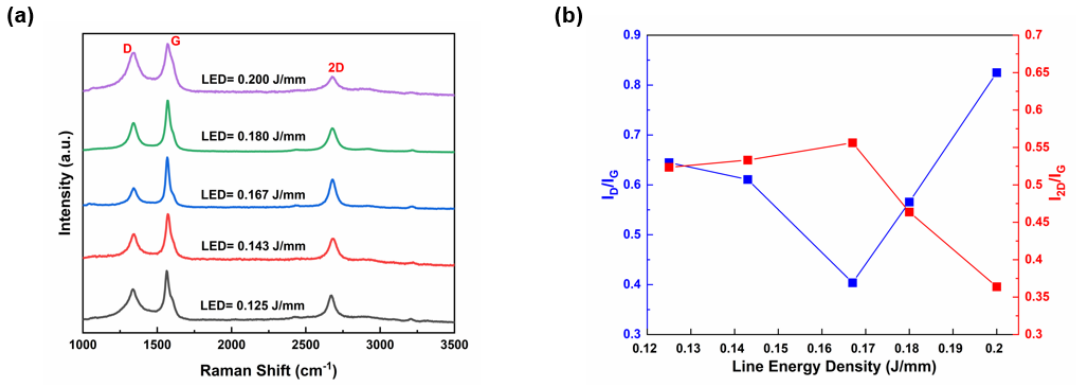

Figure 5.6 The Raman spectrum results of LIG samples processed under two-time-lasing. (a) Five LIG samples from LED range 0.125 to 0.2 J/mm. (d) I_D/I_G and I_{2D}/I_G ratios of the peaks at five different LED values.

5.3.1.2 SEM

The morphology of the LIG obtained at various LED values was investigated using SEM. **Figure 5.7** depicts the paper-derived LIG structure obtained at LED values ranging from 0.167 J/mm to 0.2 J/mm. **Figure 5.7 a-c** displays the LIG structure engraved using the line-by-line approach viewed from the top. The sample with a lower LED value (LED = 0.167 J/mm) as shown in **Figure 5.7 a** appears to have a more even porous structure, with no visible glass fibre exposed, giving more stable electrical resistance readings. As the LED value increases (**Figure 5.7 b and c**), the laser occasionally burns through the brown paper exposing the glass fibres underneath as indicated in the yellow dashed box, which becomes defect zones and give instability to the electrical resistance measurement. The magnified view in **Figure 5.7 d-f** provides a closer look at the growth of the LIG structure. In **Figure 5.7 d**, the porous LIG microstructure of LED = 0.167 J/mm is fuzzier and appears to be in the form of villi, indicating a higher level crystallisation of graphene at lower energy fluence. On the other hand, **Figure 5.7 e and f** show that the LIG obtained at higher LED values (0.18 and 0.2 J/mm) is more agglomerated and has more voids. The reduced degree of graphene crystallisation is consistent with the Raman spectral analysis (**Figure 5.6 a**), as evidenced by the broader and less intense 2D peak compared to the sample prepared at a lower laser energy density (LED) of 0.167 J/mm. This suggests increased structural disorder or defects at higher LED conditions. Therefore, the LED setting at 0.167 J/mm represents an optimal value, giving more high-quality graphene, a uniform LIG morphology, and stable electrical conductivity.

Therefore, the brown paper LIG composites will be fabricated at LED = 0.167 J/mm for the following section.

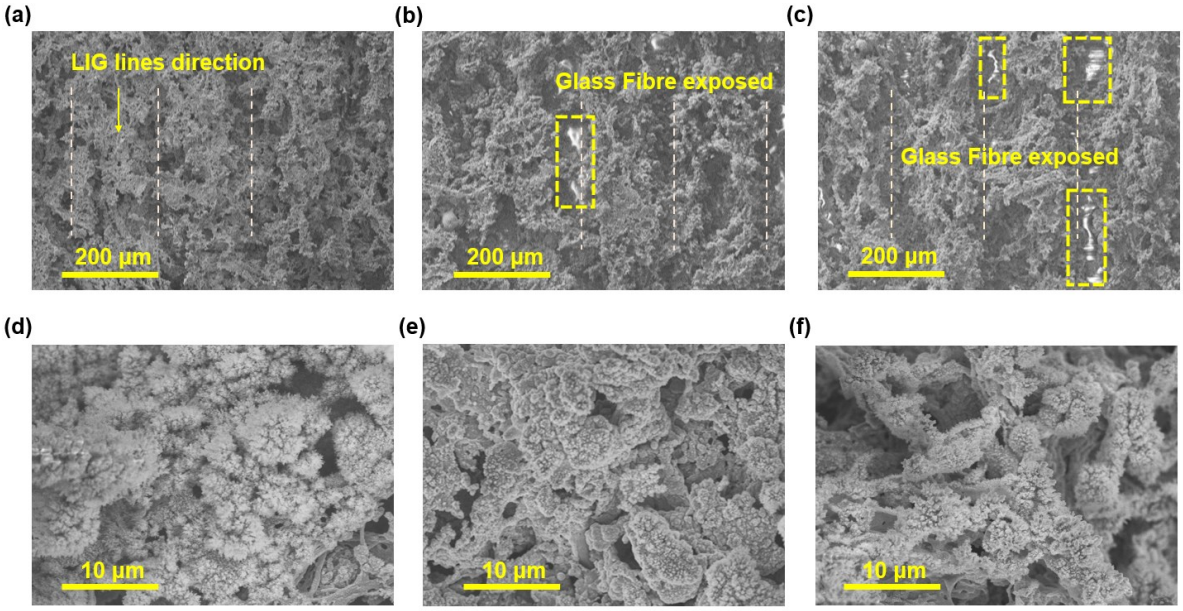

Figure 5.7 The SEM images of laser-scanned brown paper composite surface. (a-c) The LIG lines patterns following the line-by-line engraving approach at LED = 0.167, 0.18, and 0.2J/mm (left to right). (d-f) The detailed LIG microstructure of the conductive frame at energy LED 0.167, 0.18, and 0.2 J/mm (left to right).

5.3.1.3 Microscope inspection

The cross-sectional morphology of the LIG (LED 0.167 J/mm) on the composite surface was inspected to provide insights into the LIG sensor's working mechanism and also to show the adherence of the LIG to the brown paper substrate. The transversely printed LIG pattern functions based on principles of established crack-based sensors [66, 109]. The microcracks in between the graphene lines disrupt the current path. When strain is applied, cracks widen, increasing electrical resistance. The remaining bridges (intact conductive regions) between cracks dominate electron transport. Higher strain further separates cracks and will exponentially raise the electrical resistance. This mechanism enables highly sensitive strain detection which is distinct from the geometric elongation model discussed in Chapter 4. **Figure 5.8** illustrates the cross-section of the LIG sensing layer viewed under the microscope, after it was encapsulated in resin and subsequent surface polishing using SiC foils of grade 320, 600 and 1000 followed by polishing in diamond slurry of particle sizes 9, 6, 3 and 1 µm. The cross-section was taken at transverse direction (see **Figure 5.2**, cross-section cut for the microscope observation) and shown in **Figure 5.8 a**. The printed LIG lines aligns on the composite surface with the remained brown paper substrate beneath. **Figure 5.8 b** shows the magnified region at the outer edge of LIG engraving, where the height of the LIG lines can be compared to the thickness of the unlased

brown paper. The lasing process transformed half of the brown paper thickness into parallel lines of LIG with a semi-circular cross-section. The laser did not reach the load-bearing reinforcement glass fibre layer and therefore did not compromise the structural integrity of the composites. The profile of the LIG lines followed the Gaussian distributed laser intensity, and they appear as semi-circular electrodes with a radius of approximately 100 µm, which is consistent with the lasing line density setting at 0.2 mm/lines. The interstitial regions between LIG lines contain fewer conductive materials, making them prone to microcrack formation under strain. These separated LIG segments function as conductive microchannels, establishing a crack-bridge sensing mechanism. As strain-induced microcracks propagate between LIG microchannels, the global electrical resistance of the sensor changes dynamically. This principle elaborates the sensitivity of transversely oriented LIG structures, differing from the horizontal two-point conductivity measurements presented in Chapter 4 [66, 109]. **Figure 5.8 c** depicts the zoom-in view of the LIG lines, where the semi-circular LIG will produce microcracks under strain.

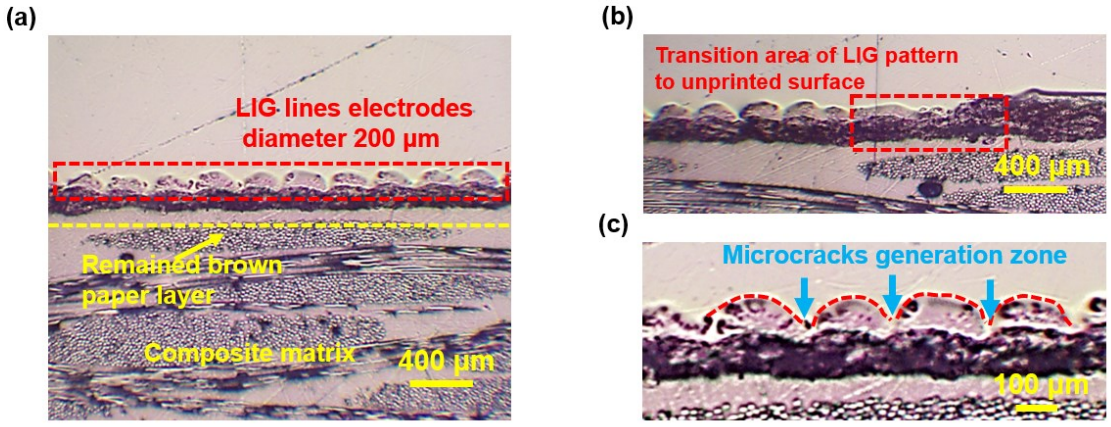

Figure 5.8 The optical microscope image showing the cross-section of the brown-paper derived LIG composite. (a) The LIG lines synthesised on the composite surface with a semi circular cross-section. (b) The LIG lines at the edge of laser engraving area. (c) The microcracks generation zone between LIG lines.

5.3.2 Test results of cyclic four-point bending

Figure 5.9 a illustrates the mechanical straining (tensile or compressive) of Group 1 samples in four-point bending, depending on how they are positioned (with the LIG pattern facing down or up) in the bending jig. Cyclic loading under low strain conditions was conducted to evaluate the sensitivity of the LIG sensors to compressive and tensile, prior to detailed investigation of the geometric influence of LIG strain sensing.

Samples S1~S4 with 8×16 mm rectangular LIG pattern as mentioned in **Table 5.1** were loaded cyclically from 0 to 200 N (or about 0.6% strain), staying below 35% of the composite failure load.

The composite strain was calculated as the ratio of stress to the elastic modulus, which was determined via preliminary 3-point bending tests. A preload cycle was applied to all samples to stabilize the LIG sensing element and reconfigure the conductive pathways, ensuring more consistent and reliable electrical responses in subsequent measurement cycles. The electrical resistance value before the first preload cycle was considered as the initial electrical resistance (R_0). The average initial electrical resistance of samples S1-S4 was 6.4 ± 0.43 kΩ. For the LIG under tension (samples S1 and S2), the resistance change exhibited a clear linear relationship with strain during loading, successfully tracking the maximum loading peaks, as shown in **Figure 5.9 b** and **5.9 c**. The results are repeatable for the two samples. However, resistance reading at the unloading and loading transition phases at the end of each cycle was much noisier, potentially caused by the stick-slip effect due to the non-linear contact or entanglement between the LIG porous microstructures when they were brought closer together upon unloading. Overall, the LIG is very responsive in sensing tensile strain, where the microcracks between LIG lines separate and therefore increase electrical resistances. In practice, the noisy response at the unloading stage is not of major concern as it happens at very low strain value (less than 0.25%) where damage in a composite structure is not expected to take place. It is also noticeable that it takes about 2-3 loading cycles (including the preloading cycle) for the LIG's strain response to stabilise and become more regular. A gradual reduction in the resistance change range was observed from the first to the tenth cycle after preload. This indicates the LIG system attains a metastable state after initial stabilization which is characteristic of most nanomaterial-based strain sensors[93]. Beyond the preload cycle, the following cycles induced negligible structural alterations, allowing the conductive pathways to revert to their original configuration.

Figure 5.9 d and e shows the response of LIG lines on the compression side in bending for two samples (S3 and S4). For samples under tension, the cyclic peaks stabilize after the fourth and fifth cycles in **Figures 5.9a** and **5.9b**, respectively. However, fluctuations persist at the bottom of each cycle. Therefore, only the first cycle was excluded as a preloading cycle in the following analysis, which aligns with established methodologies in other research and facilitates direct comparison of sensing performance metrics [53, 57]. The LIG sensor exhibited greater noise in sensing compressive strain compared to tension strain. During the initial preload cycle under compression, the electrical resistance of LIG increased due to internal rearrangement, stabilizing at higher values before subsequent loading cycles. In the following cycles, the LIG exhibited a linear decrease in resistance as compressive loading increased, accompanied by small fluctuations within each cycle. The preload cycle elevated the initial resistance after unloading by approximately 3– 4%. The electrical resistance changes in subsequent cycles varied within a range of 3– 7%. The observation aligns with prior research on LIG composites under compression[53], which demonstrated enhanced conductive contacts and consequently

increased conductivity. While the paper-derived LIG sensor can effectively detect transition between compressive strains in unloading and loading, it exhibited a less consistent and irregular response. The complexity of compression strain sensing can be attributed to non-linear contact within the porous LIG microstructure, where complicated mechanical interaction can take place such as stick-slip effect, microscopic crumpling and buckling which can cause microscale LIG folding and wrinkling, resulting in permanent or temporary deformation of the LIG microstructure. Although the LIG lines are encapsulated by the UV resin, the internal LIG conductive network not reachable by the resin is still porous which is especially prone to localized material instabilities during compressive loading. This causes a gradual drift in initial resistance observed after each compression cycle, indicating incomplete recovery of the LIG conductive path. Due to the complexity and irregularity in compressive strain sensing, the following work focusses on the influence of LIG geometry on tensile strain sensing only.

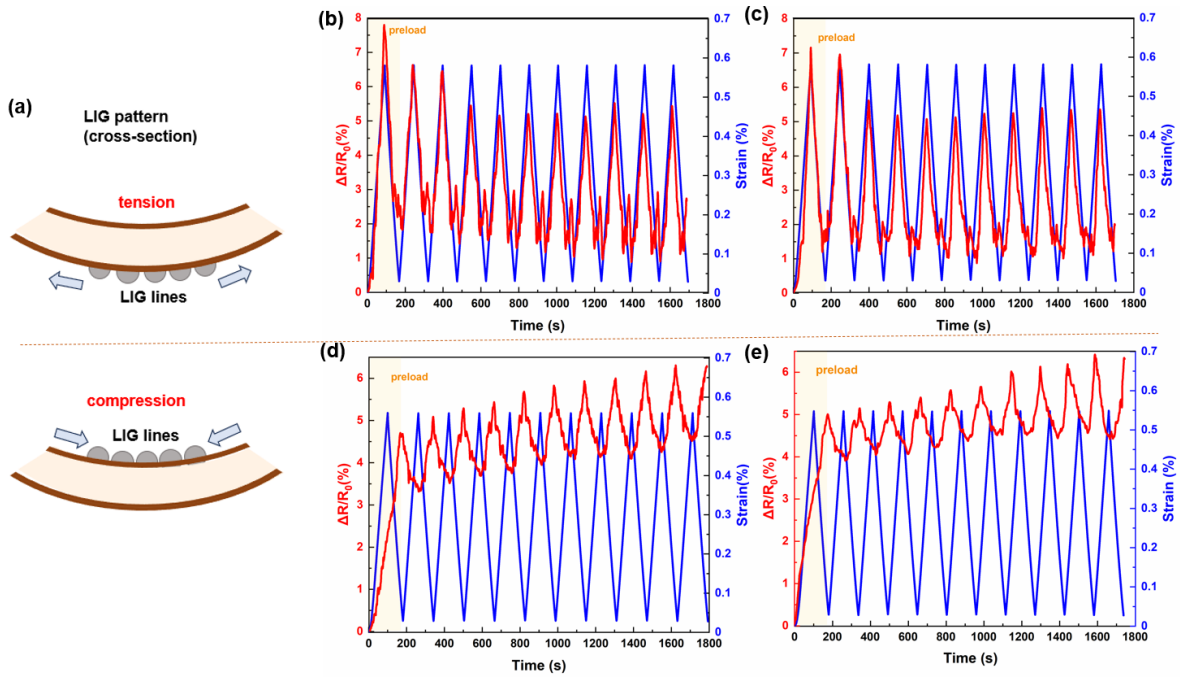

Figure 5.9 The cyclic four-point bending test results for tension and compression under 200N maximum load. (a) A schematic showing the LIG lines seeing tension or compression strains depending on how they are positioned and bent in four-point bending. (b, c) Sample S1 and S2: electrical resistance changes versus bending tensile strain for 11 cycles. (d, e) Sample S3 and S4: electrical resistance changes versus bending compressive strain for 11 cycles.

The results of Test Group 1 demonstrate the tensile strain sensing capability of LIG sensors, it remains unclear the influence of the LIG sensor geometry on sensing sensitivity at low cyclic strain up to 0.6%. Conventional strain gauges typically exhibit improved sensing performance with increased length, as longer dimensions yield higher baseline electrical resistance [110]. To maintain compactness in local strain measurement, these gauges are often designed in serpentine or zigzag patterns. In contrast, printed LIG strain sensors operate via crack

propagation, meaning their sensitivity depends on crack dynamics rather than baseline resistance. For samples under tension, the cyclic peaks stabilize after the fourth and fifth cycles in **Figures 5.9a** and **5.9b**, respectively due to inherent differences in LIG structural rearrangement. However, fluctuations persist at the bottom of each cycle. Therefore, only the first cycle was excluded as a preloading cycle in the following analysis, which can be observed from other research [57, 111]. To explore this, the samples in Test Group 2 (three samples of three different length-to-width ratios 1:1. 2:1, 3:1) were tested under cyclic loading as detailed in **Table 5.1**. Therefore, the electrical resistance value achieved after preloading served as the reference initial resistance (R_0') for better quantifying subsequent resistance changes. The initial resistance (R_0') values of the LIG scale were found to scale linearly with their length: 8 mm-LIG exhibited an average of 3.2 ± 0.27 kΩ, 16 mm-LIG and 24 mm-LIG showed progressively higher averages of 6.75 ± 0.39 kΩ and 10.16 ± 0.51 kΩ, respectively.

Before investigating the length influence of cyclic four-point bending tests, a control specimen (24 mm × 8 mm) was subjected to electrical measurements under zero mechanical load for 3000 seconds in **Figure 5.10**. This baseline assessment confirmed the absence of significant signal drift in the measurement system, thereby verifying its stability before mechanical loading applied. In general, all three geometric configurations demonstrate good cyclic sensing capability, capable of capturing the peaks and troughs of the cyclic loading. **Figure 5.11 a** reveals a highly repeatable sensing pattern among the three LIG samples (S5-S7) with 8 mm length. They take one cycle after the preloading cycle to exhibit a more consistent and regular sensing response to strain. However, the signal at the peaks of strain looks more irregular compared to the troughs of strain during the load reversal. **Figure 5.11 b** illustrates the test results for the three LIG samples (S8-S10) with 16 mm length. The sensing responses are consistent with the test results of samples S1 and S2, indicating good repeatability in the sensing responses despite the they were samples of different batches. After the second cycle, the resistance change signal capturing the strain peaks was cleaner, but it was noisier at the strain troughs compared to the LIG samples of 8 mm long shown in **Figure 5.11 a**. **Figure 5.11 c** depicts the test results for LIG samples (S11-S13) with 24 mm length. The resistance change signal is much noisier compared to the shorter LIG samples, with upward drifting baseline and peak resistance values after each load cycle. After the first cycle, the overall resistance changes drift upward from 4% to 6%, indicating reduced stability for the longest LIG geometry in the cyclic test.

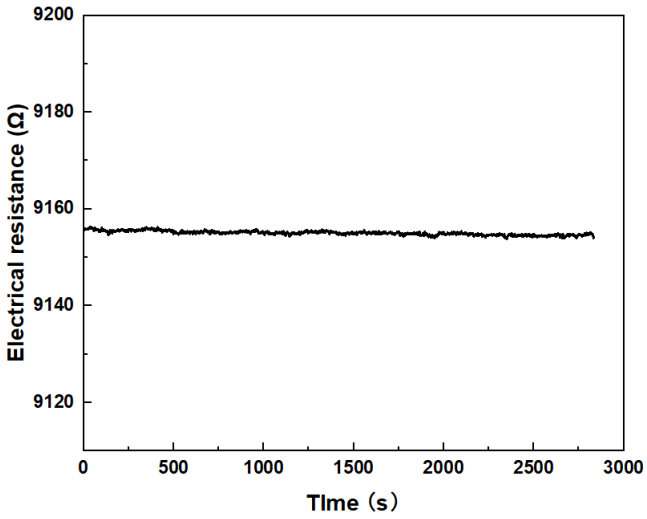

Figure 5.10 The electrical resistance recording of the control sample over 3000 seconds.

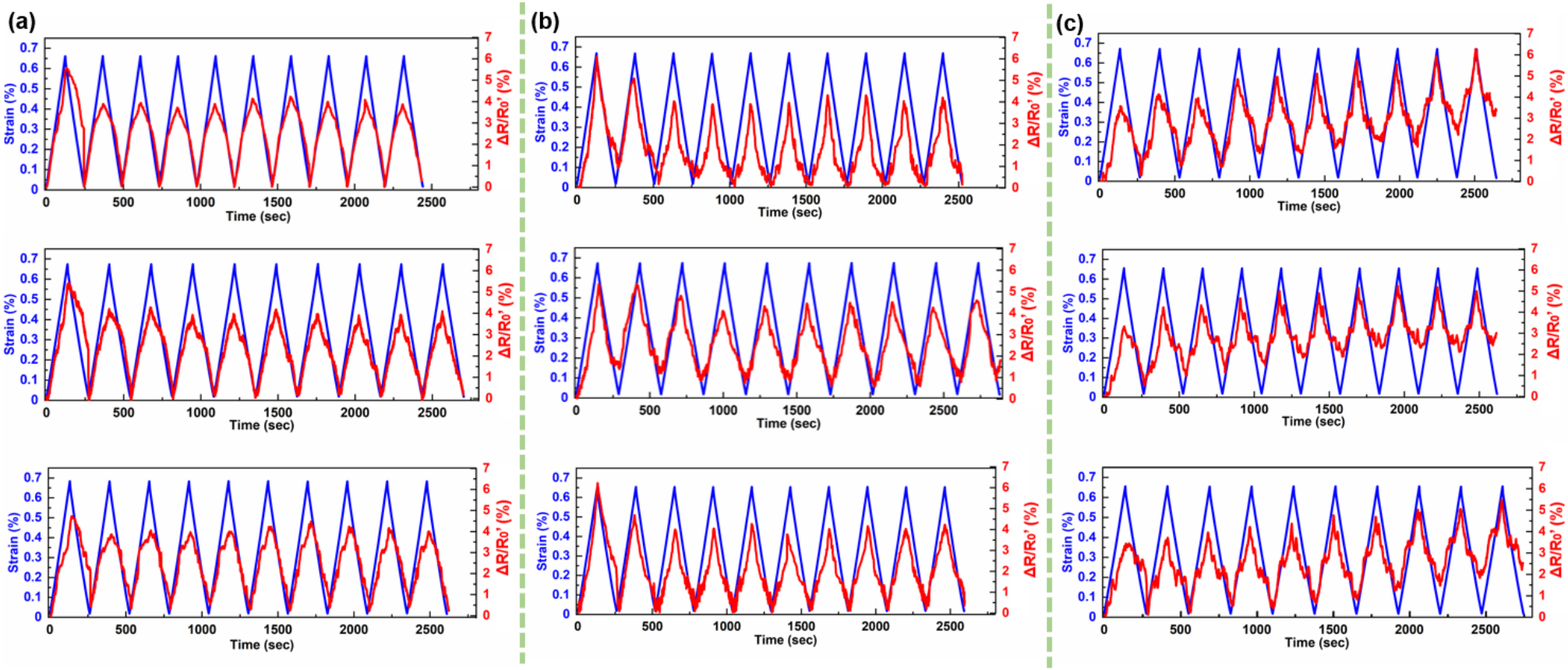

Figure 5.11 The electrical resistance changes of different LIG geometrics under applied tensile strain in four-point bending test for 10 cycles up to 200 N, excluding the preload cycle. (a) Three LIG samples S5, S6, S7 of dimensions 8 x 8 mm. (b) Three LIG samples S8, S9, S10 of dimensions 16 x 8 mm. (c) Three LIG samples S11, S12, S13 of dimensions 24 x 8 mm.

The difference in the strain sensing responses observed in the LIG samples of different lengths can be explained using the size effect on material strength[112]. In this case, a longer LIG sensor leads to a higher probability of encountering more defects or weak points of lower strength in its porous microstructure, due to increased complexity and potential of variations. On close inspection, a snag in the resistance change signal can be observed during the loading phase for each cycle for all samples as shown in **Figure 5.11**. For clarity, the resistance change graph of one LIG sample of each length in **Figure 5.11** is reproduced and enlarged in **Figure 5.12**. The snag in the sensing response potentially indicates microcracks opening at the defect sites in the LIG, causing fluctuations in the resistance reading. Considering only the first loading cycle, the strain value at which the snag happens decreases with the length of the LIG sensor. It happens at about 0.25%, 0.15% and 0.075% strain for the LIG of 8 mm, 16 mm and 24 mm long respectively. A line can be drawn joining the snag points for all subsequent loading cycles for each sample to evaluate their stability in recurrence. For the LIG of 8 mm long, the snag point is smoother and the snag line is relatively flat, suggesting that there were fewer microcrack opening events in it and the microcracks were recoverable upon unloading. On the other hand, for the LIG of 24 mm long, there are more rough snag points along the loading curve and the snag line drifts upward together with the baseline resistance after every load cycle. These are indicators that there were more microcracks in the longer LIG which interacted in a more complicated way, and that they were not fully recoverable causing irreversible rearrangement in the LIG microstructure and therefore a permanent increase in the baseline resistance values. Under cyclic loading, repeated mechanical stress induces the accumulation of microcracks in the LIG network which disrupts conductive pathways. This effect becomes more pronounced in longer LIG sensors due to their extended percolation networks, which provide more potential sites for microcrack formation, dislocations, or contact point failures. Concurrently, cyclic strain generates lattice defects in graphene (e.g., vacancies and dislocations), increasing charge carrier scattering and contributing to resistance drift.

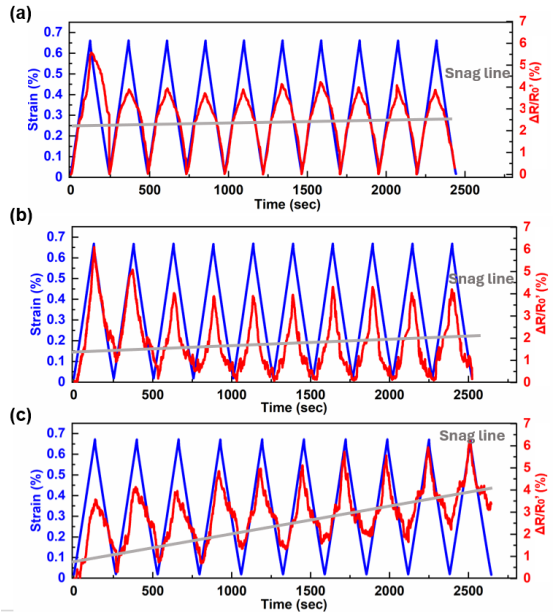

Figure 5.12. The electrical resistance change signal for three LIG lengths, with a snag line (in grey) connecting all the snag points for all cycles observed during the loading. (a) LIG length of 8 mm. (b) LIG length of 16 mm.(c) LIG length of 24 mm.

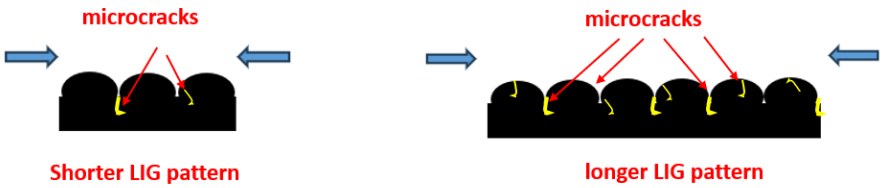

Figure 5.13 The schematic that longer LIG structures exhibit more defects and microcracks arranged in series giving a bumpier response, especially in the unloading stages.

Referring to **Figure 5.11** and **Figure 5.12**, the resistance changes curves of the LIG sensors during the unloading phase, regardless of their length, are always noisier compared to the loading phase. The LIG sensors have a nonuniform microstructure and consist of many microcracks opening from defects under loading (**Figure 5.13**). During unloading, especially near the end of the unloading phase, they can interact and make contact in a non-linear fashion (e.g. friction, stick-slip effect, etc.) giving fluctuation (snag points) in the reading. As illustrated in **Figure 5.13**, both short and long LIG possess the same crack or defect distribution, but they show different amount of crack interaction or dynamics. The shorter LIG exhibited fewer microcracks and weaker interactions along the conductive path, resulting in a smoother unloading response compared to the longer. For the longer LIG (e.g. the 24 mm long LIG), the snag points shown in **Figure 5.11** and **Figure 5.12** happened more frequently in the unloading curve compared to the shorter LIG, highlighting that there were active complex interactions of the microcracks during unloading. Additionally, bending introduces uniform strain on each printed LIG line, while LIG deformation further contributes to variations in resistance response. However, resin-infused LIG exhibits

greater stiffness after resin infusion. Since the total LIG thickness was around 100 μm, minor deformations play a subcritical role compared to strain-induced microcrack effects.

The strain sensing sensitivity of the LIG sensors is similar regardless of their length, having a similar gauge factor (the average GF for 8 mm is 7.01, 16 mm is 7.07 and 24 mm is 7.16). These results confirm that the gauge factor (GF) of a sensor remains independent of its length as the crack distribution is identical. The slight GF increase observed can be attributed to the slightly more defects in the longer LIG pattern. The LIG on brown paper composites responses are approximately linear at low strain. They are responsive and able to capture strain reversal in real time (peak shift values for LIG sensor of 8 mm, 16 mm and 24 mm long are 0.16%, 1.29%, 2.95% respectively). This is because LIG are placed on the host composite free surface which is less affected by the viscoelastic response of the composite. However, a shorter LIG sensor tends to give a clean and consistent sensing response for low to moderate cyclic loading and is therefore preferable.

5.3.3 Monotonic four-point bending

5.3.3.1 Experiment results for monotonic test

In Test Group 3, the same LIG sensors of different length-to-width ratio were also evaluated for their sensing performance under monotonic four-point bending until failure. Learning from the results in Section 5.3.2, the samples were preloaded for 2 cycles up to 150 N prior to the monotonic loading to stabilise the LIG response. The resistance values after preloading served as reference initial resistance (R_0') for different LIG lengths: 8mm-LIG exhibited an average of 3.07 kΩ, 16mm-LIG and 24mm-LIG showed averages of 6.62 kΩ and 10.38 kΩ. The resistance changes as a function of applied strain for the six LIG samples (S14-S19) are presented in **Figure 5.14**. They do not show distinctive responses for the LIG sensors of different lengths, unlike the results shown in Chapter 4 (**Figure 4.9**) where the piezoresistivity of the LIG sensor is strongly dependent on its width. The longer LIG sensor on brown paper composites does not improve the strain-sensing sensitivity. The overall resistance change across the full range of applied strain exhibits non-linear behaviour, with the slope of resistance change accelerating significantly as the composites approach failure.

The response can be divided into two distinct stages, characterized by their slope. In stage 1 (strain ε = 0%–0.2%), the gauge factor of the LIG strain sensor is around 10.24, found using a linear fit averaging over the responses of all samples. During this stage, the LIG shows linear increase in resistance with applied strain up to a transitional point about 0.2% strain. The presence of the transitional point is consistent with the knee point seen in **Figure 4.6** in Chapter 4. After the

transitional strain, irreversible microcracks start to develop exponentially and generate a corresponding sensing response.

All the samples failed by localised buckling of the surface ply on the compression side, as indicated by the sharp load drop in the plot. It is typical for a woven fabric composite to fail by compressive buckling in a bending test due to fibre waviness in the woven architecture. Therefore, there are no compression results presents as the data were noisy and not stable. Prior to the sample failure at the maximum load after 1.4% strain, the LIG resistance change curve displays a kink around 1.2% to 1.4% strain (highlighted by red boxes in the inset of **Figure 5.14**), followed by a sharp surge marking the final measurable stage for the electrical resistance. The timing of the kink in resistance change varies slightly between different samples due to material variability in the woven glass fabrics and slight thickness variation across the samples. However, the general trend of resistance changes is consistent among samples.

After the kink, the resistance change abruptly increases from 20% to over 30%, exceeding the preset measurement upper bound of 1 MΩ of the digital multimeter, suggesting that the LIG sensor has transitioned to a near non-conductive state. If the LIG sensors are calibrated appropriately, a measurement upper limit or a kink in the signal can potentially be used as a warning indicator against imminent structure failure. Note that the LIG sensor was placed on the tensile side of the samples, while the ultimate failure in buckling happens on the compressive side. This demonstrates that in bending load cases, it is not necessary to place the LIG sensor on the compressive side where failure is expected to happen. In pure bending, the compressive strain is correlated to the tensile strain. It is more sensible to put the LIG sensor on the tensile side as it shows better sensing performance with tensile strains. The results underscore the capability of LIG to function as a strain sensor as well as a warning indicator before composite failure, emphasizing the sensor's potential in structural health monitoring.

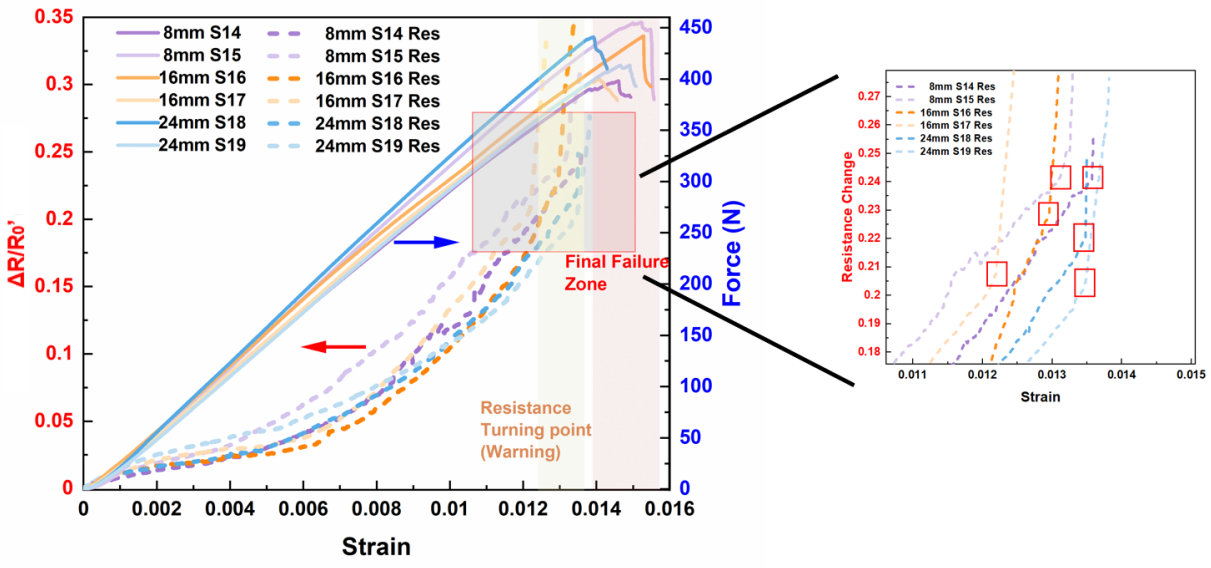

Figure 5.14 The force (solid lines) and $\Delta R/R_0$' (dash lines) of LIG composite samples versus surface tensile strain during monotonic bending. The orange and red zones mark the regions where the resistance changes increase sharply and the final failure. The kink in the resistance change signal of each LIG sample is indicated within the red boxes in the inset.

5.3.3.2 Crack modelling for monotonic test

To quantitatively explain the resistance changes of the transversely engraved LIG, a simplified physical model based on crack-bridging theory[104, 109] is developed in this section. Firstly, the fundamental strain-induced crack expansion is assumed to follow an exponential relationship, as expressed in Equation 5.4 for $\varepsilon \geq 0.2\%$:

$$L(\varepsilon) = L_0 \cdot exp(k\varepsilon) \qquad \text{Equation 5.4}$$

In this expression, $L(\varepsilon)$ represents the microcracks length under strain ε, L_0 denotes the original microcracks length at the transitional point (literature reference value: 3 μm) [66], and k is a non-dimensional material-dependent growth factor that quantifies the growing rate of the microcracks in between LIG lines. A strain-dependent growth factor $\alpha(\varepsilon)$ serves as a critical parameter in quantifying the efficacy of residual conductive pathways that bridge the existing microcracks[113, 114]. Therefore, this mathematical model for the piezoresistivity of the LIG effectively captures the dual mechanisms of the progressive widening of existing microcracks and the formation of new microcracks, as formulated in Equation 5.5:

$$R(\varepsilon) = R_t \left[1 + \alpha(\varepsilon) \cdot \left(\frac{L(\varepsilon) - L_0}{h_e}\right)\right] \qquad \text{Equation 5.5}$$

Here the R_t and $R(\varepsilon)$ represent the resistance value at the transitional point (average value 1.0205 R_0' based on linear fitting in stage 1) and strained LIG's electrical resistance respectively. h_e denotes the effective thickness of the conductive layer, calculated from the cross-sectional image of the LIG lines (**Figure 5.8**) by transforming the semicircular area into an equivalent rectangular area as described in Equation 5.6. The average radius of LIG electrodes is around 100 μm estimated from **Figure 5.8 a**. To convert the microcracks elongation into a dimensionless quantity, the incremental microcracks expansion is normalised by dividing it by the effective conductive layer thickness h_e[115]. This formulation assumes a linear relationship between strain (ε) and the increase in bridging resistivity, providing the simplest representation of crack-bridging behaviour, as expressed in Equation 5.7, where a_0 is a non-dimensional, empirically determined parameter. This formulation incorporates both the material properties and geometric parameters of the LIG pattern. By substituting the values, the relative change in electrical resistance can be expressed by Equation 5.8:

$$h_e = \frac{semi-circular\ area}{bottom\ length} = \frac{\frac{1}{2}\pi r^2}{2r} = 76.62\ \mu m \qquad \text{Equation 5.6}$$

$$\alpha(\varepsilon) = a_0\,\varepsilon \qquad \text{Equation 5.7}$$

$$\frac{\Delta R}{R_0'} = \frac{R(\varepsilon)-R_0'}{R_0'} = 1.0205 \cdot \left[1 + \alpha(\varepsilon) \cdot \left(\frac{L(\varepsilon)-L_0}{h_e}\right)\right] - 1$$

$$= a_0 \cdot \varepsilon \cdot \left(\frac{3 \cdot exp(k * \varepsilon) - 3}{75.08}\right) + 0.0205 \qquad \text{Equation 5.8}$$

Model fitting was conducted using the experimental data of the six LIG samples with different LIG lengths in **Section 5.3.3.1**. The coefficient of determination (R^2) was employed to assess the model's fitting accuracy in describing the electromechanical sensing response as shown in **Figure 5.15**. The R^2 value serves as a preliminary indicator of data linearity, quantifying how closely the measured response follows a linear trend. However, it should be noted that R^2 does not directly reflect the magnitude of nonlinearity errors in the sensor's output. The optimal parameters for a_0 and k were determined through the implementation of the grid search optimization method from the Python scikit-learn package [83]. The model demonstrated a good agreement with experimental observations using the optimised parameters a_0 = 150 and k = 96.12. The average R^2 values achieved for the responses in Stage 2 for sample S14 to S19 are all above 0.94. The coefficient of determination (R^2) for each sample is explicitly labelled using the corresponding colour in **Figure 5.15**. Beyond Stage 2, in Stage 3, the microcrack growth becomes unstable and the prediction by Equation 5.8 breaks down.

Overall, the crack-based model successfully captured the exponential but stable growth of microcracks in LIG in Stage 2, which significantly increases the resistivity. There is irreversible alteration of the LIG conductive network. The model correlates the rate of microcrack growth to the applied strain in the LIG sensor, providing a theoretical basis for predicting LIG sensing performance under higher load before the unstable Stage 3.

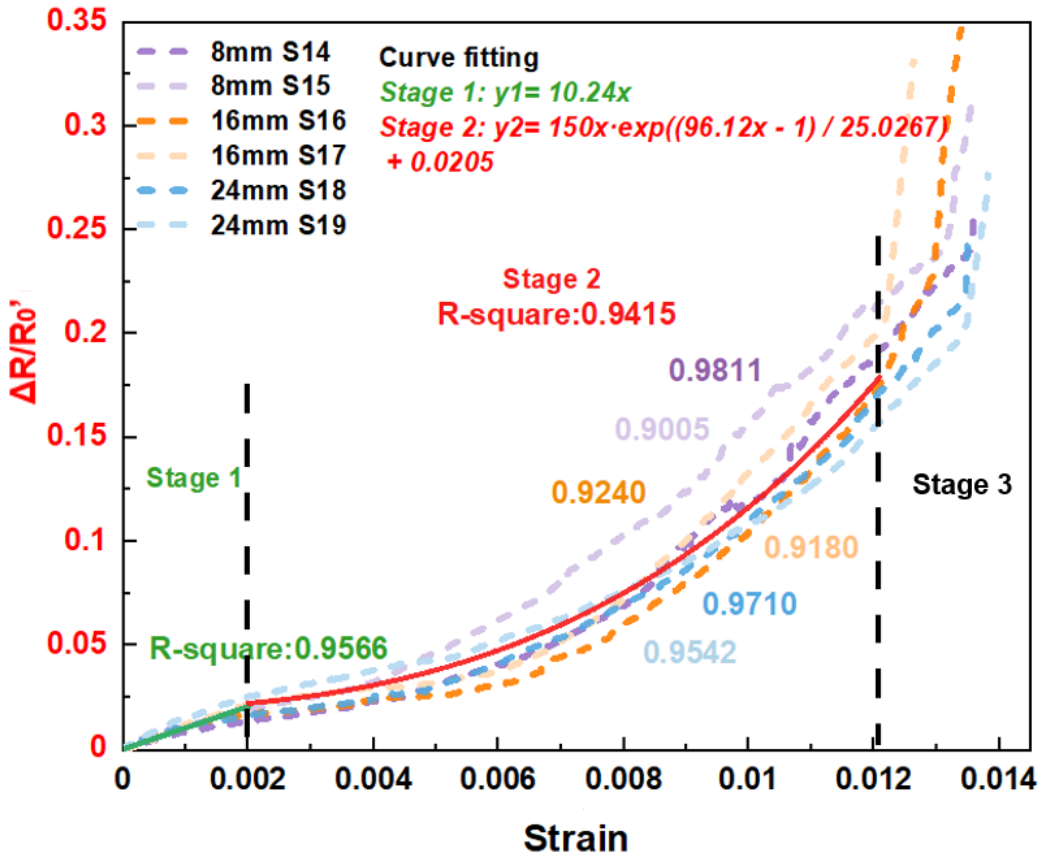

Figure 5.15 The resistance changes and loading force versus strain (dot lines) for LIG brown paper composite samples S14-S19, subjected to monotonic four-point bending tests under tension. The curve fitting results for the two stages (solid lines), where the slope represents the gauge factor.

5.4 Summary

This chapter presents a convenient method to engrave sensors directly on the surface of composite structures via a commercial laser engraver unit. Brown paper was added as the surface ply on the glass fibre-reinforced composite to serve as a substrate for synthesising LIG sensors. The lasing parameters have been optimised through Raman Spectrum and SEM characterisations before the test sample fabrication. Cyclic four-point bending test was performed to introduce the LIG sensors to tensile or compressive strain on the surface. More consistent sensing patterns were observed for the tensile strain than the compressive strain. This can be attributed to the more complex mechanical interactions between the microstructural features in the porous LIG during compression. The study of the influence of sensor length on the LIG strain sensing performance also reveals that a shorter sensor is desirable as it gives a cleaner sensing response.

Extending the investigation to monotonic loading in bending up to failure shows that the length of LIG sensor does not influence its sensing sensitivity. They all exhibited non-linear behaviour across the entire sensing range, consistent with the sensing trends seen in the cork-derived LIG discussed in Chapter 4. A crack-bridge model was developed using the geometric parameters of LIG lines to describe the piezoresistive behaviour of sensors made of transversely engraved LIG lines. The model is different from the random void model presented in Chapter 4 which was used to describe the piezoresistivity of longitudinally engraved LIG lines.

The application of the LIG sensor as a potential warning indicator against composite ultimate failure was also briefly discussed. The printed LIG adds negligible weight and requires no additional adhesion, enabling direct printing on composite surfaces for monitoring cyclic strain (below 35%). By tracking its resistance change using a simple instrumentation setup, the LIG has again demonstrated its potential as a low-cost surface strain sensor in structural health monitoring which can be mass produced through the use of a renewable brown paper precursor attached on a structure.

Chapter 6 Paper-derived LIG for moisture uptake and volatile solvents sensing

This chapter aims to explore other potential sensing applications for paper-derived LIG as a surface sensor on composite structures. Since composite structures can be exposed to environmental agents in real-world scenarios, this chapter focuses on the investigation of moisture and hazardous chemical sensing. This demonstrates the potential for developing multifunctional sensor for LIG-based smart composites.

6.1 Introduction

Graphenic materials, with superior electrical properties and distinctive atomic structures, have emerged as potential materials for extensive applications ranging from small wearable sensors to large-scale civil engineering components [24, 116]. Previous research reveals that graphene exhibits rapid reaction in electrical conductivity when subjected to external stimuli [68], including fluctuations in humidity [67] , and variations in atmospheric gases and pH levels[69]. However, the majority of graphene electrochemical and liquid sensors have been investigated as smart flexible devices. Chapter 5 demonstrated that by embedding the brown paper substrate during the resin infusion process, LIG can be conveniently engraved on the composite surface. This achievement enables the integration of graphene sensing elements directly on structural materials, opening new possibilities for environmental monitoring applications. The LIG sensor , for instance, can detect moisture uptake in composite structures which can lead to structural degradation, or hazardous solvents leakage before it leads to health and safety issues, thereby minimizing response delays and enabling pre-emptive interventions.

Literature review in Chapter 2 has discussed that LIG nanostructures can effectively detect liquid droplets and humidity variations. However, most research concentrated on LIG derived from PI-based materials, which primarily serve as standalone sensors. The investigations focused on monitoring the exposure to environmental agents of the host composite materials remain unexplored. For instance, although most fibre-reinforced composites (FRCs) exhibit good chemical resistance and resistant to water due to their highly cross-linked molecular matrix, extended exposure to humid environments or hazardous solvents can result in significant matrix degradation[117]. Moreover, flammable liquids leakage like acetone and isopropyl alcohol (IPA) on the surface of composites poses an additional fire hazard.

This chapter proposes an integrated LIG sensor on the composite surface with moisture and microvolume liquid sensing ability. This research addresses a research gap in composite

structural health monitoring such that detection can be made in real-time, in contrast to conventional methodologies that rely on laboratory-based techniques. For example, moisture uptake measurement of composite samples is typically done using the gravimetric analysis[118], where the change in mass of the samples is measured over time when exposed to a controlled moisture environment. It requires small sample sizes and may not represent the actual moisture state of the entire composite structure. In the first part, the microvolume droplet test using volatile solvents is performed on the LIG sensor to assess its sensitivity and responsiveness to volatile solvents in real-time. This is to simulate cases where the LIG is used as a leak detection sensor on a hazardous solvents storage tank made from composite materials. In the second part, the sensing capability of LIG for moisture uptake in the host composite is explored. The results are useful to understand the effect of moisture exposure to the baseline resistance of LIG sensor when it is not encapsulated on the host composite surface.

6.2 Experiment

6.2.1 Sample fabrication and LIG synthesis

The E-glass fabric composite plate with brown paper as the surface was fabricated following the identical procedures described in **Section 5.2.** It was then cut into square specimens (microvolume liquid test:25 mm× 25 mm, moisture test: 36 mm× 36 mm) using a diamond cutter. Laser irradiation of the brown paper composite was processed by a commercial CO_2 laser unit at 10 W power and 60 mm/s speed with two-time lasing at focus lengths of 6.75 mm and subsequently 2.4 mm. These were the same optimal lasing parameters determined from the Raman spectrum and electrical resistance characterisation discussed in Section 5.3, which will not be elaborated in this chapter. All laser treatments were processed under normal room conditions. The square shaped (12 mm× 12 mm) LIG patterns were lased on both liquid sensing (6 specimens) and moisture uptake sensing (6 specimens) as shown in **Figure 6.1 a**. Silver conductive paint was applied on the opposite edges of the LIG pattern and cured in oven at 60°C for 15 minutes for resistance measurement. The LIG was left exposed without encapsulation.

6.2.2 Volatile solvents dropping test setup

The square pattern LIG depicted in **Figure 6.1a** was extended on top of the silver conductive paint at both ends by the copper foil for in-situ electrical resistance measurement in the liquid drop test as shown in **Figure 6.1 b**. Laboratory grade acetone (99.5% Lab Alley) and isopropyl alcohol (99.8% IPA, Bubble Three), which are both volatile and flammable chemicals were chosen as the stimuli. The high evaporation rate of these chemicals enables the recovery of the LIG after being

exposed to them to be observed in a short period of time. A 3 µL microvolume of liquid was deposited in the centre of the LIG pattern using a pipette gun. **Figure 6.1 c** depicts the configuration of liquid drop sensing on the composite surface. Three samples each for both acetone (Sample 1-3) and IPA (Sample 4-6) were test and the electrical resistance values were recorded by the digital multimeter (Keysight, 2110) with KI Tool software.

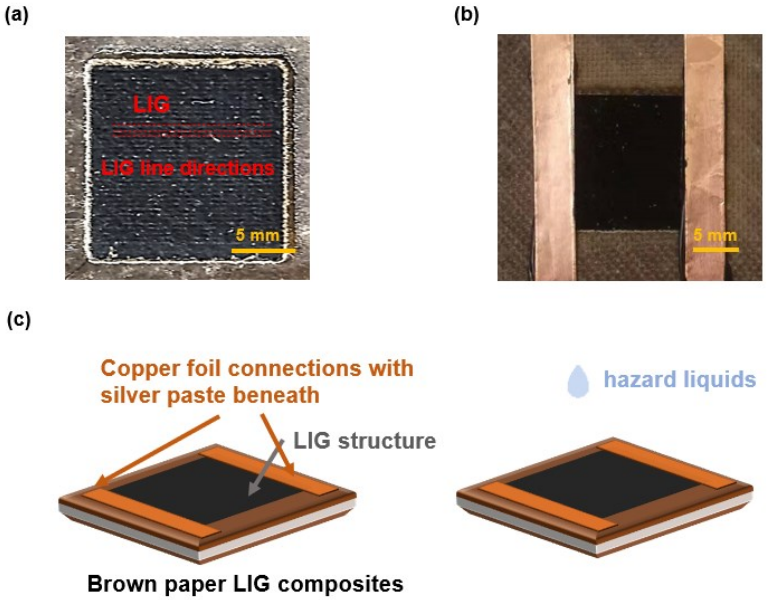

Figure 6.1 The specimen and experiment design for the volatile solvent's droplet sensing. (a) The optical image of LIG square pattern printed on brown paper on the surface of composite samples. (b) The LIG square pattern with copper foil extension as connections. (c) The schematic of the volatile solvent's droplet sensing experiment.

6.2.3 Moisture uptake test setup

Six specimens with silver paste connections were dried in an oven at 50°C for 4 hours before being exposed to moisture as depicted in **Figure 6.2 a**. The low temperature setting was chosen to minimise the thermal stress on the composite. Their dry weight and electrical resistance were measured immediately after removed from the oven. The samples were placed in an enclosed glass chamber at 80 ± 5% relative humidity (RH) and room temperature (~25°C) to replicate the humid working conditions for composites, as shown in **Figure 6.2 b**. The RH was controlled by placing a glass of distilled water in the chamber throughout the test to ensure there was always constant amount of water vapour in the surrounding of the samples. The stable RH in the chamber was confirmed by monitoring the read-out from the hygrometer placed next to the samples. Precise HR was not required in this test as the main goal was to seek correlation between the amount of moisture uptake and the change in electrical resistance of the LIG. The moisture uptake by the composite samples was determined using the gravimetric method by measuring

their weight gain as a function of exposure time using an electronic analytical balance (LICHEN FA2004) with readability up to 0.1 mg. Immediately after they were weighed, the electrical resistance of the samples were probed on the silver paint on both ends using a digital multimeter (Keysight, 2110), with three times measurements for each sample for averaging. The sample weight and the electrical resistance were taken periodically for 1 week, with reduced frequency as the time passed. Since the LIG was not encapsulated, the samples were handled very carefully to avoid physical contact with the fragile LIG which can disrupt its microstructure.

To investigate the reusability of the LIG sensor for subsequent cycles of moisture uptake, the same samples were immediately dried in an oven at 50°C for four hours, before they were exposed to moisture for the next 7 days following the same procedures described in the previous paragraph. Two additional rounds of moisture absorption and desorption were conducted.

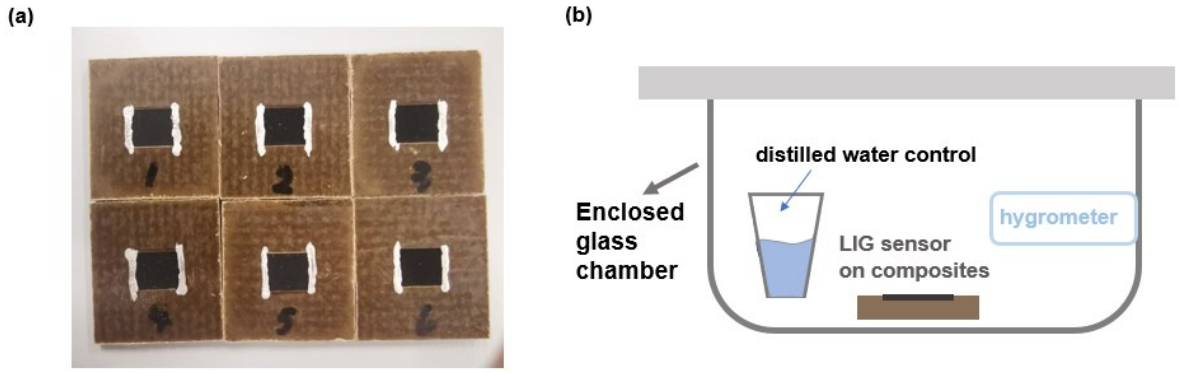

Figure 6.2 The specimens and experiment design for LIG moisture sensing. (a) LIG printed on brown paper composite with sliver pastes connections. (b) The schematic of the LIG composite moisture absorption sensing in the enclosed chamber.

To understand the physical change in the LIG microstructure before and after exposed to moisture, two additional LIG samples (Sample A and B) of size 8 mm x 8 mm were purposely fabricated and sent for viewing using field emission scanning electron microscopy (SEM, HITACHI SU8000). To obtain the 'before' images, the two samples were first dried in the oven for 2 hours at 60℃, after which they were viewed immediately in SEM. A square inspection window (5 mm× 5 mm) was selected for each sample which exhibits unique identifiable microstructural features (e.g. trenches or creases) such that the same sites could be revisited after 10 days of moisture exposure. The samples were left untouched for 10 days in the same glass chamber and viewed again in SEM for the 'after' images. The SEM images were post-processed using Fiji software [119] for analysis. The image registration was performed by linear stack alignment function to reorientate and relocate the same sites in the 'before' and 'after' images. 5 % of the pixels along the edges were excluded and cropped from all images.

6.3 Results and discussion

6.3.1 Resistive response to volatile solvents

The real-time changes in electrical resistance of three LIG samples in response to acetone and IPA liquid droplets of volume 3 µL were presented in **Figure 6.3**. The responses were consistent among the LIG samples tested for acetone and IPA respectively, giving unique signatures that one can use to identify these volatile chemicals. Upon contact with the LIG sensor, the acetone droplet rapidly spreads across the surface due to wetting effects, inducing an immediate and sharp increase in electrical resistance in **Figure 6.3 a**. This response originates from two concurrent mechanisms: (1) disruption of conductive pathways as the liquid physically separates the graphene flakes, and (2) localized charge redistribution caused by dipole interactions between acetone molecules and the LIG surface. The combined effect creates a transient barrier to charge carrier transport, manifesting as the observed resistance surge [11]. In the second phase, the rapid evaporation of acetone molecules from the LIG surface caused the resistance to decline almost exponentially approaching the initial baseline value. However, the new resistance value remains at a slightly elevated value compared to the initial baseline due to the irreversible rearrangement of the LIG conductive network by the liquid acetone that has completely evaporated. The slight disparity of resistance change reading among the different samples and the recovery dynamics of resistance reading was caused by the variability in effective wetted area by the droplet (causing different evaporation rates), and the variability in localised surface defects or irregularities in the LIG structure (creating charge puddles that can impede charge carrier transport).

Figure 6.3 b illustrates the resistance change of IPA droplet on the LIG surface. In contrast to liquid acetone, it exhibited a gradual decrease in resistance, followed by a gradual recovery curve. The increase in conductivity of the LIG resulted from the fact that IPA is a polar solvent [120]. The IPA droplet can lead to increase in the carrier concentration and its intercalation among the graphene layers. The whole process was more gradual due to its slower rate of evaporation compared to acetone, leading to a longer period for the electric reorganisation in LIG.

Overall, the three samples under the same laser settings demonstrate high repeatability of LIG sensing performance for both acetone and IPA droplets. Their characteristic signal of relative resistance change can be used to detect the presence of these two volatile chemicals. The test can be extended to other volatile chemicals or liquids with their signature signals documented to make the LIG a low-cost liquid sensor. Different liquids interact with the LIG differently at the microscale level. The signals for different chemicals can be distinguished by comparing the

amplitude, frequency, and duration of the waveform. In this case, acetone exhibits an approximate 8% resistance increase while IPA demonstrates a 2.5% resistance decrease.

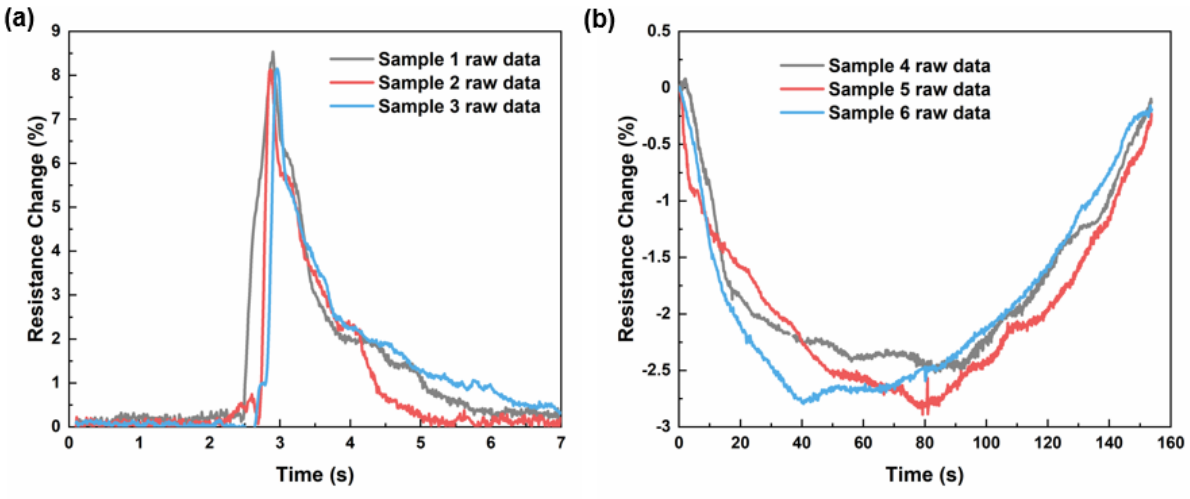

Figure 6.3 The volatile liquid droplet sensing results. (a)The acetone liquids sensing results on Sample 1 -3. (b) The IPA liquids sensing results on Sample 4 -6.

6.3.2 LIG electrical resistance change versus water uptake

The ability to sense water absorption in FRCs is crucial due to the detrimental effects of moisture ingress on mechanical properties and durability of composites[121, 122]. The moisture uptake of the LIG samples given in terms of percentage of weight gain (averaged for 6 samples) is plotted against resistance change up to 7 days in **Figure 6.4**. The relative weight gain ($\Delta W/W_0$) and electrical resistance change ($\Delta R/R_0$) were calculated by dividing the change of weight (ΔW) and electrical resistance (ΔR) measured at preselected intervals with the initial weight (W_0) and electrical resistance (R_0) immediately taken after they were dried in the oven. The results indicate a strong linear correlation between electrical resistance variations and weight gain. The measured weight gain (~0.5% after 7 days) was found to be significantly lower than the results obtained in different water exposure conditions by other researchers for fibre-reinforced composite materials. For example, composite samples in fully submerged test conditions typically achieved 1.2-1.6% weight gain [123]. A prolonged exposure more than 3 months in increased temperature (322 K) environments gave weight gain around 1%. This reduced magnitude reflects early equilibrium attainment without water submersion, where moisture penetration becomes limited at sustained high humidity around 80% RH. This behaviour therefore represents realistic moisture uptake of composite materials in a humid (rather than extremely wet) environment.

The yellow dashed line represents the linear fit for weight gains and resistance changes, yielding a high R-squared value exceeding 0.98. Note that the weight gain was measured for the whole

composite including the LIG sensing layer, while the resistance change was measured only for the LIG layer. The linear correlation shows that the resistance change in the LIG layer is reflective of the water content in the host composite and that it can be exploited to monitor moisture uptake. Despite the fact that stacked graphene layers show hydrophobic properties [41] , the defect sites in the porous LIG and oxygen-containing functional groups from the composite matrix on which the LIG is synthesised can act as local hydrophilic sites, attracting water molecules to form clusters that disrupt electron mobility [124]. The water molecules that trapped in the LIG network can also scatter the charge carriers which reduces the mean free path, resulting in the increase of electrical resistance which been illustrated in **Figure 6.5**.

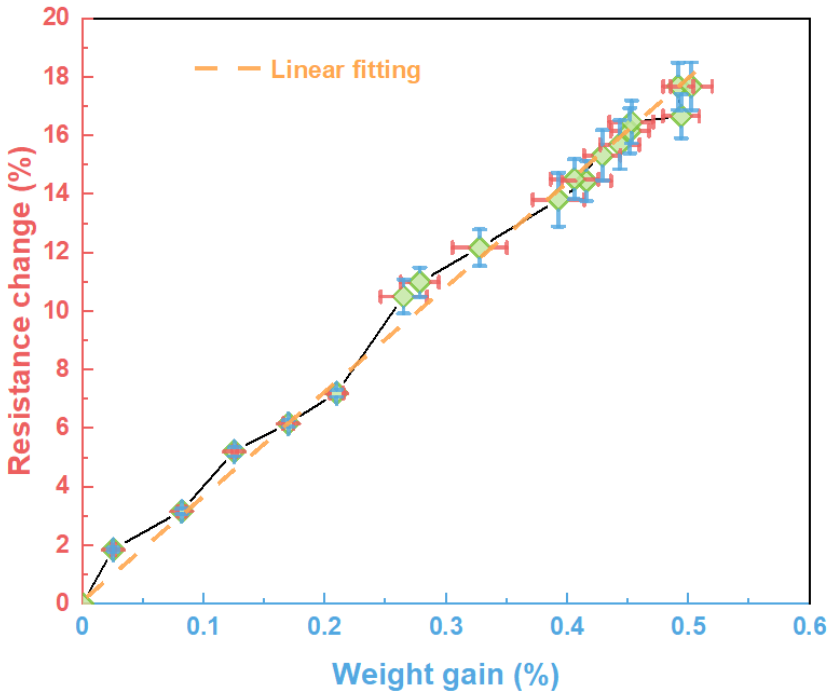

Figure 6.4 The linear correlation between moisture absorption up to 7 days of the composite samples (averaged for 6 samples) in percentage of weight gain and the electrical resistance changes of the LIG.

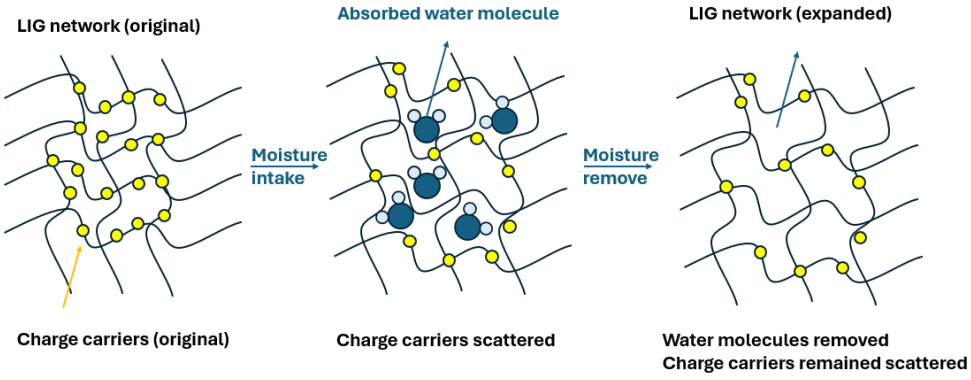

Figure 6.5 The schematic of water molecules trapped in the LIG network during the moisture intake and the LIG network after moisture desorption.

6.3.3 Subsequent test of moisture absorption and desorption

Moisture can penetrate polymeric composite materials by diffusive or capillary processes. The Fickian diffusion was commonly used to describe water absorption in thin plates [125]. The Fickian diffusion approximation for water absorption in composites at the early stage can be expressed by:

$$\frac{M_t}{M\infty} \approx \left(\frac{4}{h}\right)\sqrt{\frac{Dt}{\pi}} \qquad \text{Equation 6.1}$$

where h denotes the composite thickness while D represents the constant diffusion coefficient. The variable t corresponds to the time elapsed after exposing the composite to a moisture-conditioned environment. M_t refers to the measured composite mass gain at time t, whereas M_∞ signifies the saturated mass gain at equilibrium. In Equation 6.1, the relative mass (or weight) gain is proportional to the square root of time, with the rest of the parameters being constant.

This section discusses the average response of LIG to three rounds of moisture absorption in six composite samples. The results are shown in **Figure 6.6**. A two-stage absorption process has been observed for all three rounds. In the initial stage, the composite samples exhibit Fickian behaviour over the first 24-hour period where weight gain is linearly proportional to square root of time. In this stage, free water molecules penetrate the composite's microporous structure and voids, particularly at fibre-matrix interfaces.

In the second stage, the weight gains observed in the three rounds of moisture uptake follow the Langmuir model which documented for epoxy matrix systems [118, 126]. The Langmuir model comes in different variants, but all converge on describing a gradual moisture uptake rate before approaching moisture equilibrium. The reduction in absorption rate is attributed to the bound water molecules and their hydrogen-bonding interactions with the polymer network. The extended plateau region in the absorption curve reflects the equilibrium between water trapping and de-trapping processes after 7 days (or $\sqrt{t}$ =12.96 $hr^{0.5}$). The good correlation between the weight gain and resistance change curves again confirms that the resistive response of the LIG layer is reflective of the moisture uptake in the host composite.

The subsequent drying and re-exposure of the LIG to moisture produced notable results. After the first oven drying, the resistance of the LIG pattern did not fully recover to its initial value, suggesting there were permanent structural changes in the porous network upon moisture removal. This could be attributed to irreversible expansion of the LIG microstructure due to the ingress of water as shown in **Figure 6.5**. This irreversibility provided the LIG sensor with a memory of the previous moisture exposure history of the composite. It is worth mentioning that the weight of the samples was not able to return fully to its original value as well but experienced a small gain

of about 0.05%. The heating might not be sufficiently long to remove the bound water that was trapped deep within the composite samples.

The same findings were observed in the subsequent rounds of moisture exposure. In the second and third rounds, the LIG could still exhibit its moisture sensing capability; however, a diminished range of resistance changes or sensitivity was observed. This suggests that after every round of moisture exposure, the freedom for the porous LIG to displace became smaller, and there was less amount of defective LIG microstructure that could break freely to trap water molecules. Uncertainty analysis of the experimental data in **Figure 6.6** reveals that the standard deviation (shown by the error bars in the figure) of the resistance measurement increased with time during the first cycle of moisture exposure, and that the increase in standard deviation is more obvious in the first cycle and compared with the subsequent cycles. This observation corroborates the hypothesis that there are unstable microstructures in the pristine LIG. There is more scope for them to rearrange in the early stage and that gives them high responsiveness when exposed to stimuli such as moisture. The scope for rearrangement becomes less over time causing it to become less responsive. At the same time, the structural disorder in the LIG can grow over time causing fluctuation in the read-out, but in the long term it slows down to a steady state. Therefore, the results suggest two competing mechanisms, i.e. the moisture uptake sensing ability of the LIG relies on the mobility of the LIG microstructures, but inevitably the water molecules give structural disorder to the LIG. This indirectly highlights the importance of encapsulating the LIG sensor to stabilise its fragile microstructure and suppress the grow of structural disorder in a more controlled manner for sensing purposes such as strain sensing, which has been done in the work in Chapter 5.

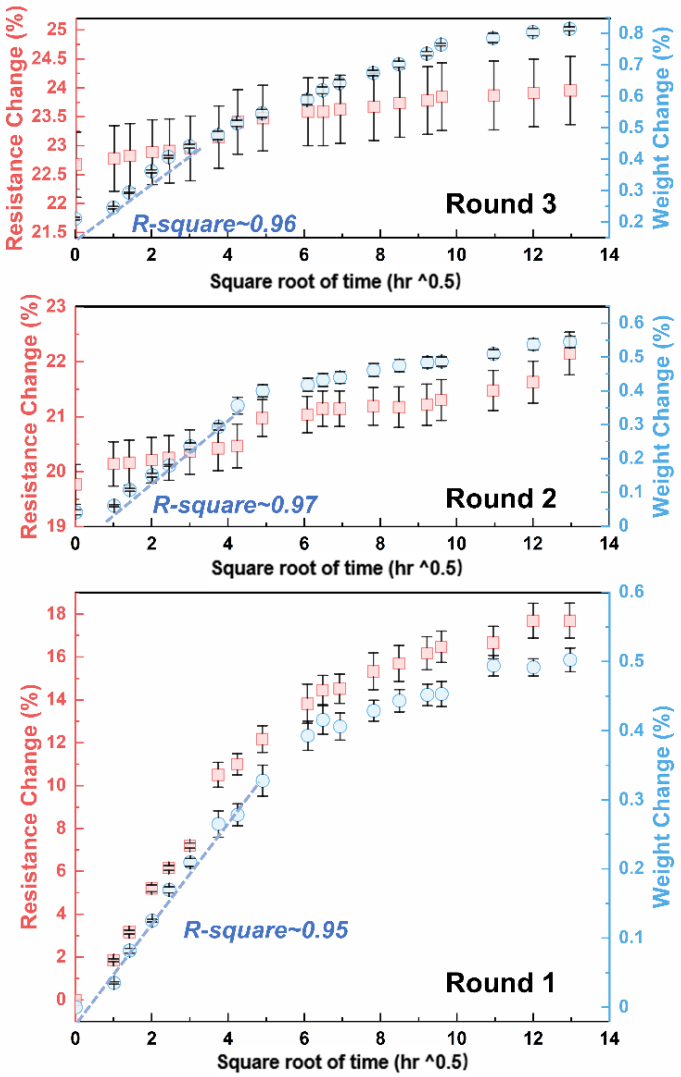

Figure 6.6 The resistance changes and weight gains are plotted against square root of exposure time for three rounds of moisture absorption in the composite samples.

6.3.4 SEM inspection of LIG microstructure change on moisture exposure

Due to the heterogeneous structure of the LIG composites and lack of empirical data, multiphysics simulation of the LIG interacting with the water molecules to understand the underlying mechanism is challenging. As an alternative approach, visual inspections of the microstructural change in the LIG before and after moisture exposure through SEM was conducted to qualitatively verify the hypothesis discussed in **Section 6.3.3**. The morphological changes before and after moisture exposure for 10 days for five predetermined regions across two LIG samples were identified and highlighted in the following. Five scanning regions from Sample A and Sample B are depicted in **Figure 6.7**.

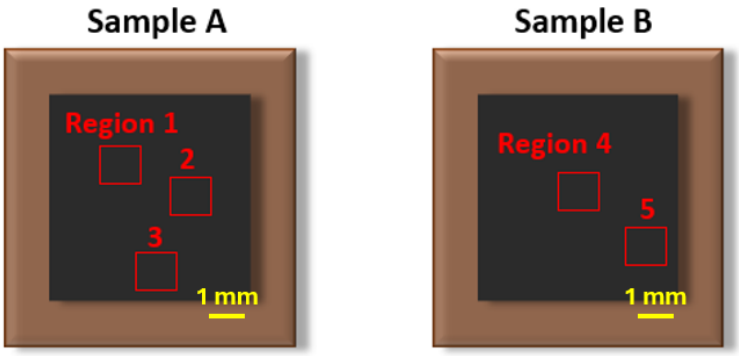

Figure 6.7 The schematic of the locations of scan Region 1-5 on Sample A and Sample B.

In Region 1 of Sample A (centre area in the square pattern, **Figure 6.8 a**), the LIG structure exhibits a distinct ridge feature extending diagonally from bottom left to top right. Following moisture exposure (**Figure 6.8 b**), SEM imaging reveals localized overcharging spots, manifested as bright, blurred parts, despite it was taken using the same SEM settings (e.g. voltage and magnification). The overcharging effect in SEM arises when the electron beam causes excessive charge accumulation on non-conductive or poorly conductive samples. Although LIG is inherently conductive, overcharging still occur under specific conditions. For instance, defective or oxidized regions in graphene can exhibit insulating behavior, leading to localized charge accumulation. This effect is more obvious after moisture absorption, where graphene undergoes structural expansion, generating additional defects and partial detachment from the substrate. As a result, charge dissipation becomes less efficient, exacerbating the overcharging phenomenon. This phenomenon results from decreased conductivity due to water absorption, causing electron beam charge accumulation in less conductive areas. This is true for all images taken for samples exposed to moisture. The observed overcharging correlates with the resistance increase measurements reported in previous **sections 6.3.3**, providing evidence of moisture-induced structural rearrangement.

The selected LIG regions highlighted in the yellow dashed boxes provide some visual evidence of structural transformation before and after moisture exposure. Comparing Boxes 1, 2, and 3 between the images, the originally hollow pores disappear as the underlying graphene layers swell upward, filling the pores. Conversely, Box 4 demonstrates the opposite phenomenon, where new pores are formed. These morphological changes can be attributed to two simultaneous mechanisms: (1) water molecules disrupting the carbon π-conjugated structure and expanding interlayer spacing through hydrogen bonding and capillary infiltration, and (2) localized stress concentrations causing non-uniform structural rearrangements [127]. Upon removal of the water molecules, the graphene skeleton retains these modified features because the van der Waals forces between the now-separated layers create energy barriers that prevent full recovery to the original LIG network. This permanent deformation is commonly observed in

other porous materials like cellulose fibres, where wet-induced swelling leads to irreversible structural changes that persist even after drying [128].

In Region 2 of Sample A (centre area in the square pattern, **Figure 6.9 a**), the LIG structure is characterized by a bifurcated opening (highlight in red). Comparative analysis reveals similar structural adjustments in **Figure 6.9 b** across the highlighted boxes: Box 1 exhibits pore contraction, Boxes 2 and 3 demonstrate upward growth of subsurface layers resulting in pore occlusion, and Box 4 displays new pore formation. The entire bifurcated opening region (highlighted in red) exhibited upward directional expansion. These observations collectively indicate moisture-induced morphological reorganization of the LIG architecture, where localised swelling and stress redistribution drive irreversible pore closure and reformation.

Region 3 of Sample A (**Figure 6.10 a**) was taken near the edge of the square LIG pattern, identifiable by the irregular feature in the upper left quadrant (highlighted in red). Comparative analysis of pore morphology in **Figure 6.10 b** reveals similar findings to previous Region 1 and 2: (1) Box 1 demonstrates progressive pore contraction which reduces the pore dimension, (2) Box 2 undergoes structural collapse followed by secondary pore formation, and (3) Box 3 shows upward migration of subsurface material leading to pore occlusion. This shows that structural rearrangement happens commonly across the whole surface of LIG, including the regions near to the edges.

SEM images of Region 4 of Sample B (centre area in the square pattern, in **Figure 6. 11**) provide further corroborating evidence to complement the findings from Sample A. Notably, this sample exhibits more pronounced overcharging effects following moisture exposure compared to Sample A. The pore morphology changes in the highlighted regions are similar to those observed in Sample 1. (1) Box 1 reveals upward migration of subsurface LIG material resulting in complete pore occlusion; (2) Boxes 2 and 3 display pore expansion.

Region 5 of Sample B (**Figure 6.12**), positioned near the edge of the square LIG pattern, demonstrates both pore closure and expansion. **Figure 6.12 b** reveals widespread overcharging effects, with the regions in yellow boxes showing characteristic morphological changes after moisture exposure: (1) Boxes 1 and 2 exhibited upward swelling of subsurface layers leading to pore closure, while (2) Box 3 displays modest pore enlargement.

The displacement and transformation of the LIG structure offer it exceptional moisture sensitivity in a fresh and pristine LIG. SEM characterization confirms irreversible structural modifications in the LIG after moisture exposure, which permanently elevates its electrical resistance values. These morphological changes captured through sequential SEM imaging, provide the explanation to the memory effect of moisture exposure history observed in the experiment.

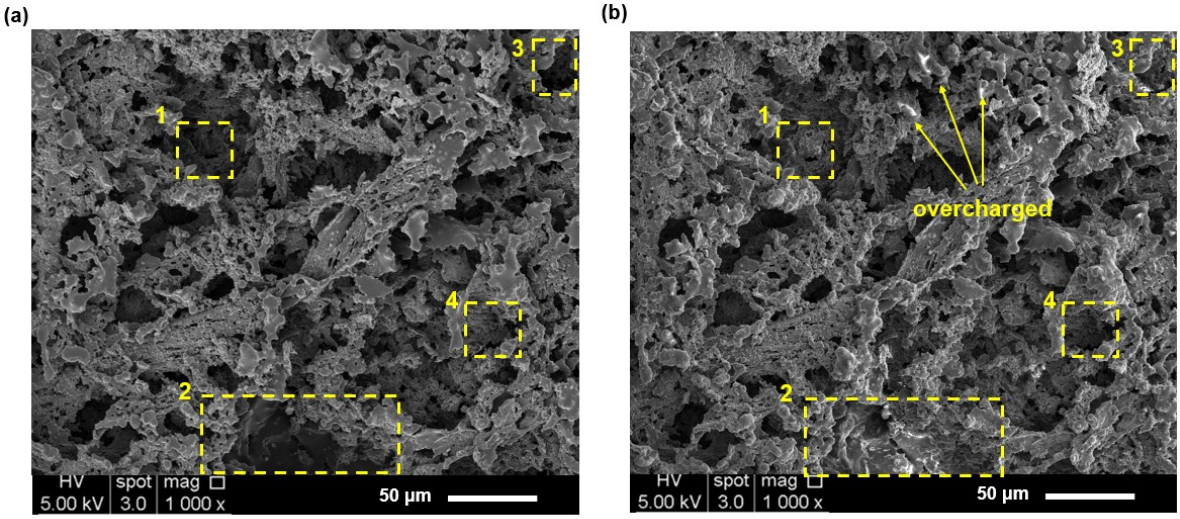

Figure 6.8 The SEM images comparison of Sample A Region 1. (a) The SEM image before and (b) after moisture exposure for 10 days.

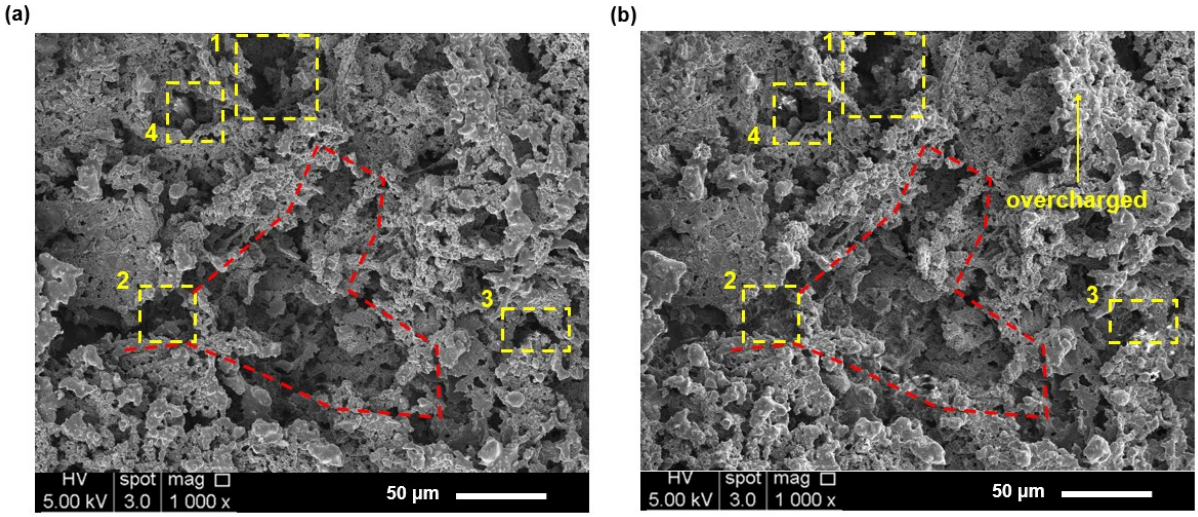

Figure 6.9 The SEM images comparison of Sample A Region 2. (a) The SEM image before and (b) after moisture exposure for 10 days.

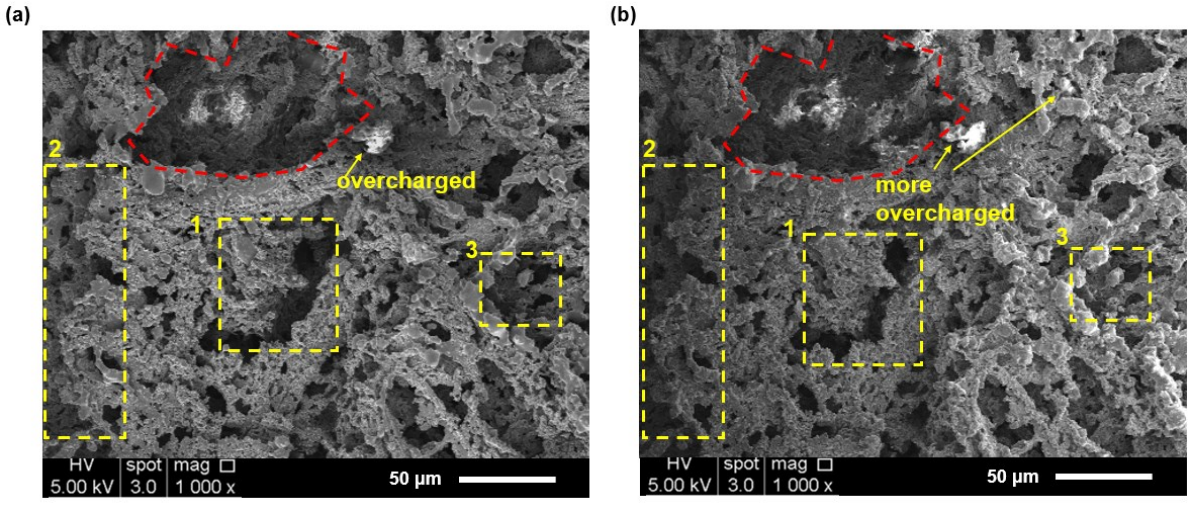

Figure 6.10 The SEM images comparison of Sample A Region 3. (a) The SEM image before and(b) after moisture exposure for 10 days.

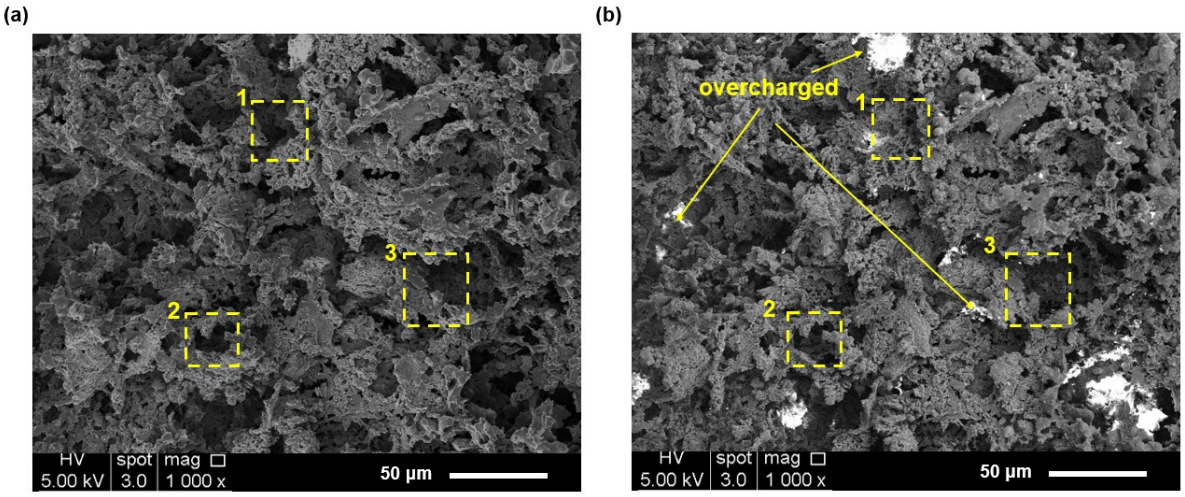

Figure 6.11 The SEM images comparison of Sample B Region 4. (a) The SEM image before and (b) after moisture exposure for 10 days.

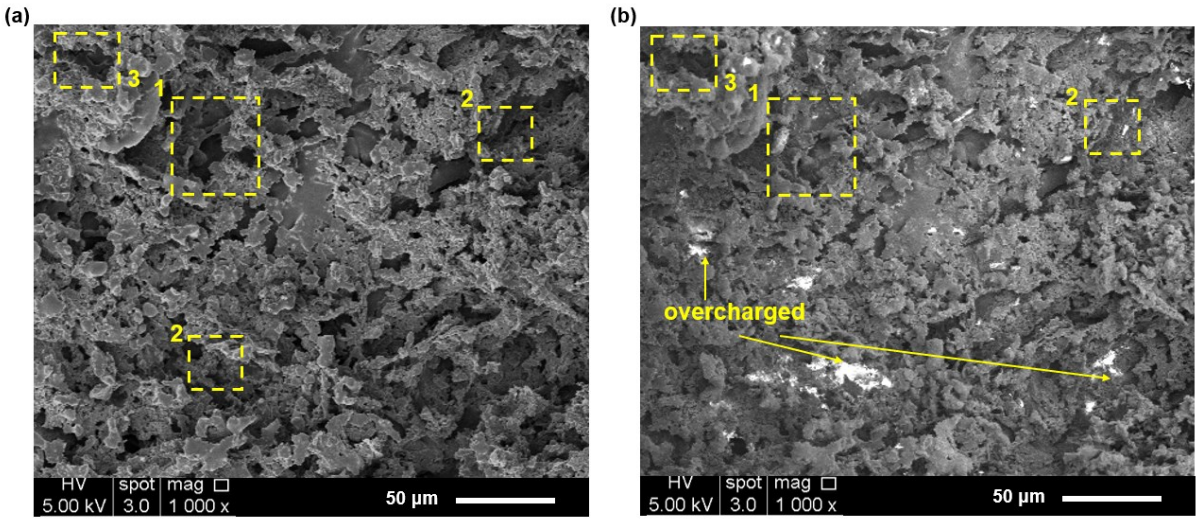

Figure 6.12 The SEM images comparison of Sample B Region 5. (a) The SEM image before and(b) after moisture exposure for 10 days.

6.4 Summary

This chapter investigates the additional functionality of paper-derived LIG on the composite surface for volatile liquid and moisture uptake sensing. The liquid sensing performance has been proven through two volatile chemicals, i.e. acetone and IPA, which give unique signature in the response. On the other hand, the moisture uptake sensing results shows high consistency among six samples, where the electrical resistance change exhibits a linear relationship with the moisture content in the samples. In sequential water absorption–desorption tests, the LIG sensors retained their sensing capability for up to three cycles. However, there are irreversible

changes in the LIG structure when exposed to moisture, leading to a permanent increase in electrical resistance with reduced sensitivity and more noise in the signal. This provides the LIG sensor the 'memory' for the ageing history of the host structure, which can be explored further.

This chapter extends the scope of LIG-based structural health monitoring beyond mechanical sensing (e.g., strain and impact sensing) to include environmental sensing. Future investigations could employ molecular dynamics simulations to model water interactions with the graphene lattice, particularly the capillary-driven filling of micropores. Such studies would help quantify moisture-induced changes in the LIG properties and establish predictive metrics for LIG sensing performance degradation. Moreover, further study could focus on optimising the morphology and geometry of LIG nanostructures to attain customised response sensitivities for diverse sensing applications.

Continuous resistance signal variations were recorded to enable subsequent analysis and differentiation between solvents. For the composite moisture uptake test, the water absorption was monitored until weight saturation, while simultaneously examining the correlation between LIG resistance changes and composite weight gain. To further characterize the material, the analysed LIG nanostructure changes was analysed by comparing SEM images of the same sample region before and after water absorption. Porosity was quantified as a key parameter to assess the expansion behaviour of the porous structure. Finally, the reusability of the LIG moisture sensor was evaluated by testing its sequential sensing performance. The multifunctional sensing ability of the LIG derived directly from the composite surface demonstrates significant potential for applications in monitoring moisture uptake and the possibility of organic solvent leaks for composite materials.

Chapter 7 Conclusions and future work

This chapter provides a summary of the findings from all experimental and modelling work conducted in this PhD project. Additionally, potential future work to enhance the design of LIG self-sensing composites, along with related publications, is presented.

7.1 Conclusions

This thesis investigates the potential of LIG sensor for structural health monitoring applications. By integrating LIG with conventional composite materials, self-sensing composites can be manufactured at a low cost while allowing customizable pattern designs with different sensitivity to serve different applications. Depending on application requirements, the LIG can be

embedded within the host composite or placed on the surface, with or without encapsulation. These distinct LIG configurations were developed, tested and their performance evaluated.

The LIG sensors fabricated on cork substrates demonstrate superior damage localization capability compared to previous aramid fiber-based LIG systems [54]. Furthermore, the cork-LIG composites exhibit significantly higher gauge factors (50-133) for strain sensing than LIG transferred from polyimide to silicone or composite prepreg substrates [66]. In contrast, paper-derived LIG sensors show more consistent cyclic strain sensing performance when fabricated with shorter lengths. These sensors display characteristic multi-stage strain response behavior, transitioning from linear to exponential resistance-strain relationships. A comprehensive performance comparison of LIG sensor strain sensing is presented in **Figure 7.1**. Both configurations in this PhD thesis operate within relatively low strain ranges while demonstrating high gauge factors. This performance aligns with the design goals of monitoring structural changes and providing early warning before composite failure.

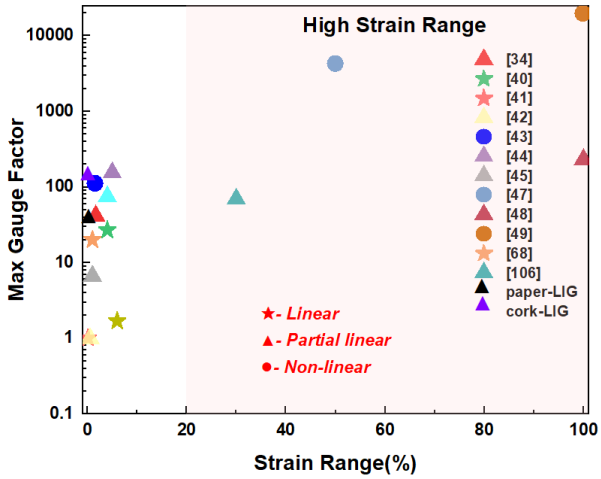

Figure 7.1 The comparison of the strain sensing between the paper and cork LIG from this thesis and with other research designs.

This thesis has addressed the following objectives:

1) *To characterise and optimise the synthesis of LIG for integration with fibre-reinforced composite materials*.

   A systematic characterisation methodology was developed. Two low-cost and sustainable substrates, i.e. cork paper and brown paper, were selected for LIG synthesis, in which laser power and scanning speed served as the primary lasing parameters for optimising the LIG quality. The LIG was characterised by visual and microscopic inspection, sheet resistance measurements, Raman spectroscopy and SEM. The optimal lasing parameters were selected to meet the following three criteria:

(1) Minimal structural defects. (2) Good LIG pattern continuity. (3) High electrical conductivity.

It was also demonstrated that the LIG can be directly integrated with or engraved on the host composite structures fabricated via conventional composite manufacturing methods such as vacuum-assisted resin infusion and vacuum bagging in an autoclave, without needing adhesives or an intermediate LIG pattern transfer step.

2) *To assess the sensing performances of LIG in composites for different applications*.

For cork-derived LIG in impact sensing application: A mesh LIG pattern was laser-engraved on cork paper and embedded as a core material within a glass fibre composite sandwich structure before it was subjected to drop-weight impact testing. The LIG channels were arranged in a mesh design and its capability in damage localisation and size estimation through measurement of their electrical resistance changes was successfully demonstrated.

For cork-derived LIG in strain sensing application: The piezoresistive behaviour of the cork-derived LIG in the composite sandwich structure was systematically examined. Cyclic tensile testing revealed distinct sensing characteristics below and above the critical strain of 0.2%. At low strains (below 0.2%), the LIG demonstrated a stable and linear resistance-strain relationship with excellent repeatability. Beyond 0.2% strain, there is microstructural change and damage development in the LIG network which modify its piezoresistivity. The piezoresistive effect exhibited greater sensitivity (with gauge factor as high as 133) in a narrow LIG sensor compared to conventional metallic strain gauges, enabling detection of subtle strains (<0.08%). However, a narrow LIG sensor demonstrated a slower response compared to a wider LIG sensor. This trade-off between strain sensitivity and temporal response highlights the design flexibility of LIG-based sensors for different measurement requirements.

For paper-derived LIG in strain sensing application: LIG can be engraved directly on the brown paper surface layer laid on the top of a glass fibre-reinforced composite, demonstrating a convenient way to integrate the LIG sensor on the host composite surface. The LIG lines were engraved in the transverse direction line by line on the composite samples to serve as crack-based resistors. Cyclic four-point bending tests were conducted to evaluate the performance of LIG sensors on both the tensile and compressive surfaces. The sensors exhibited more consistent strain responses under tensile loading compared to compression, due to complex microstructural interactions within the LIG network during compressive deformation.

Further investigation examined the effect of LIG sensor length on strain sensing performance. Shorter sensors demonstrated cleaner response signals at low strain levels during cyclic testing, while longer sensors are noisier especially when transitioning between the loading and unloading phases. Monotonic bending tests to failure revealed that sensor length did not affect the sensitivity over a larger strain range. All sensor dimensions exhibit a characteristic resistance surge before composite failure, demonstrating their potential use as warning indicators against catastrophic composite failure. The study confirmed LIG's viability as a cost-effective surface strain sensor.

For paper-derived LIG in environmental sensing application: This study investigated the environmental sensing capabilities of exposed LIG on brown paper composite surfaces. The LIG sensors demonstrated distinct and rapid responses to microvolume droplets of volatile solvents, in particular acetone and isopropanol (IPA). In the moisture uptake sensing test, the electrical resistance change in the LIG can be linearly correlated to the moisture uptake in the host composite. Irreversible microstructural displacement of the LIG caused by the water molecules was observed, resulting monotonic increase in electrical resistance in the subsequent water absorption-desorption cycles. The sensitivity of the LIG to moisture exposure decreases over time with noisier read-outs. This finding underscores the importance of encapsulating the LIG sensor for sensing stability.

3) *To develop simple mathematical models/algorithms for LIG sensor design and application*.

Using empirical data, a KNN classification model and two mathematical models are developed for the LIG sensors in various sensing applications.

KNN model for impact sensing: A KNN model was developed and trained using the experimental data of 10 J impact test and validated against tests of different energy levels and impact locations. The machine learning model achieved 94.3% accuracy in damage classification, outperforming the standard deviation criterion. This integrated system, combining LIG mesh sensing with the KNN algorithm, presents an efficient solution for large-scale structural health monitoring, offering both high precision and minimal labour requirements.

Random void model for strain sensing using longitudinally- engraved LIG: A mathematical model integrating geometric parameters with electrical conductivity variations was developed to describe the piezoresistive behaviour of longitudinally-

engraved LIG up to 1.8% strain using a Weibull-distributed random void model. By establishing the dependence of LIG's piezoresistivity on both width-to-length ratio and applied strain, this model enables the prediction of strain sensing performance for various LIG sensor geometries.

Crack-bridging model for strain sensing using transversely engraved LIG: A mathematical model was developed to characterize the piezoresistivity of transversely-engraved LIG on composite surfaces. The model specifically captures the stable crack dynamics occurring from 0.2% strain up to 1.2% strain preceding the final failure above 1.4% strain. Through this approach, an exponential relationship between resistance change and applied strain was established.

7.2 Future work

The following can be proposed for future work to optimise the sensing performance of LIG sensors for structural health monitoring of composite structures.

(1) For impact damage sensing applications, the LIG mesh can be upscaled to cover a bigger test area with more channels to study its performance in the event of multiple impact. More advanced machine learning algorithms (e.g. neural network approaches) could be explored to improve prediction accuracy when sufficient datasets are available.

(2) Further modelling efforts are warranted for strain sensing applications. Multiphysics simulations using Representative Volume Element (RVE) and Finite Element Analysis (FEA) could be conducted to determine the critical parameters governing both electromechanical response and structural degradation in LIG. For instance, mechanical strain simulations can additionally account for ply orientation, conductive interlayer thickness, and geometric configuration. For electromechanical simulations, fibre-matrix debonding disrupts conductive pathways at the mesoscale, increasing bulk resistance in relation to local percolation thresholds and interfacial shear stresses However, more experiments and material testing will be needed to generate the empirical data needed as the input for the simulation. For instance, mechanical strain simulations must additionally account for ply orientation, conductive interlayer thickness, and geometric configuration. For electromechanical simulations, fibre-matrix debonding disrupts conductive pathways at the mesoscale, increasing bulk resistance in relation to local percolation thresholds and interfacial shear stresses.

(3) For paper derived-LIG composite, sensitivity of the LIG strain sensor can be further optimised by adjusting the gap between LIG lines or incorporating serpentine design. The

effect of complex multiaxial strain and ambient temperature on the sensing performance of LIG can also be explored. Beyond substrate selection, alternative materials such as linen or natural fibre-based components could replace brown paper while maintaining the same LIG synthesis procedures which relied on the balance of LIG electrical conductivity and morphological properties.

(4) For multifunctional sensing applications, an assembly of multiple LIG sensors with different designs can be engineered and packed on a single piece of substrate. Through data post-processing, simultaneous monitoring of strain and moisture can be achieved by decoupling their respective sensing responses. Further expansion of this low-cost surface strain sensor's applicability in structural health monitoring could involve investigating its responses to additional environmental factors, such as temperature fluctuations (as a thermometer) or exposure to acidic rain.

7.3 Contributions

This PhD project was sponsored by the studentship from the University of Southampton Malaysia and School of Engineering, University of Southampton. The work has led to five published or potential publications (three published, one under review and one in preparation).

Publications list:

Journal paper:

1. Chen, X., Gan, K., Pu, S., Jalalvand, M., & Hamilton, A. (2025). Laser-induced graphene as an embedded sensor for impact damage in composite structures assisted by machine learning. Structural Health Monitoring. https://doi.org/10.1177/14759217241311516.
2. Piezoresistive laser-induced graphene as a low-cost strain sensor for composite structures.(Sensor and Actuators A: Physical, https://doi.org/10.1016/j.sna.2025.116776)
3. Surface strain monitoring of composite materials using paper-derived laser-induced graphene. (Composites Structure, to be submitted)

Conference paper:

1. Chen, X., Patil, I. G., Kou, R., Tan, K. K., Lim, J., Hoo, R. Y., Ling, T. Y., Gan, K. W., & Pu, S. H. (2023). Encapsulated laser-induced graphene flexible piezo-resistive sensors for speech recognition. 2023 IEEE International Conference on Sensors and Nanotechnology (SENNANO) (pp.180–183). Putrajaya, Malaysia. https://doi.org/10.1109/SENNANO57767.2023.10352566

2. Chen, X., Gan, K., & Pu, S. (2024). Laser-induced graphene for moisture and micro-volume liquid sensing. International Conference on Green Energy, Computing and Intelligent Technology

(GEn-CITy 2024) (pp. 209–213). Online Conference, Iskandar Puteri, Malaysia. https://doi.org/10.1049/icp.2025.0257

Bibliography

1. Chung, D.D.L., *Self-sensing structural composites in aerospace engineering*, in *Advanced Composite Materials for Aerospace Engineering*. 2016. p. 295-331.

2. Ferreira, P.M., et al., *Embedded Sensors for Structural Health Monitoring: Methodologies and Applications Review*. Sensors, 2022. **22**.

3. Farrar, C.R. and K. Worden, *An introduction to structural health monitoring*. Philos Trans A Math Phys Eng Sci, 2007. **365**(1851): p. 303-15.

4. Duchene, P., et al., *A review of non-destructive techniques used for mechanical damage assessment in polymer composites*. Journal of Materials Science, 2018. **53**(11): p. 7915-7938.

5. Morampudi, P., et al., *Review on glass fiber reinforced polymer composites*. Materials Today: Proceedings, 2021. **43**: p. 314-319.

6. Zhang, Z., et al., *Self-sensing properties of smart composite based on embedded buckypaper layer*. Structural Health Monitoring, 2015. **14**(2): p. 127-136.

7. Chung, D.D.L., *Damage detection using self-sensing concepts*. Proceedings of the Institution of Mechanical Engineers, Part G: Journal of Aerospace Engineering, 2007. **221**(4): p. 509-520.

8. Mironovs, D., S. Ručevskis, and K. Dzelzītis, *Prospects of Structural Damage Identification Using Modal Analysis and Anomaly Detection*. Procedia Structural Integrity, 2022. **37**: p. 410-416.

9. Rajak, D.K., et al., *Fiber-Reinforced Polymer Composites: Manufacturing, Properties, and Applications*. Polymers, 2019. **11**(10): p. 1667.

10. Malhotra, A. and F.J. Guild, *Impact Damage to Composite Laminates: Effect of Impact Location*. Applied Composite Materials, 2014. **21**(1): p. 165-177.

11. Pumera, M., et al., *Graphene for electrochemical sensing and biosensing*. TrAC Trends in Analytical Chemistry, 2010. **29**(9): p. 954-965.

12. Pontefisso, A. and L. Mishnaevsky Jr, *Nanomorphology of graphene and CNT reinforced polymer and its effect on damage: Micromechanical numerical study*. Composites Part B: Engineering, 2016. **96**: p. 338-349.

13. Somani, P.R., S.P. Somani, and M. Umeno, *Planer nano-graphenes from camphor by CVD*. Chemical Physics Letters, 2006. **430**(1): p. 56-59.

14. Chandarana, N., et al., *Early Damage Detection in Composites by Distributed Strain and Acoustic Event Monitoring*. Procedia Engineering, 2017. **188**: p. 88-95.

15. Etxaniz, J., et al., *Ultrasound-based structural health monitoring methodology employing active and passive techniques*. Engineering Failure Analysis, 2023. **146**: p. 107077.

16. Schilling, P., et al., *X-Ray Computed Microtomography of Internal Damage in Fiber Reinforced Polymer Matrix Composites*. Composites Science and Technology - COMPOSITES SCI TECHNOL, 2005. **65**: p. 2071-2078.

17. Carosena, M. and M.C. Giovanni, *Recent advances in the use of infrared thermography*. Measurement Science and Technology, 2004. **15**(9): p. R27.

18. Theodosiou, A., *Recent Advances in Fiber Bragg Grating Sensing*. Sensors, 2024. **24**: p. 532.

19. Meehan, D.G., W. Shoukai, and D.D.L. Chung, *Electrical-resistance-based Sensing of Impact Damage in Carbon Fiber Reinforced Cement-based Materials*. Journal of Intelligent Material Systems and Structures, 2009. **21**(1): p. 83-105.

20. Angelidis, N., C.Y. Wei, and P.E. Irving, *The electrical resistance response of continuous carbon fibre composite laminates to mechanical strain*. Composites Part A: Applied Science and Manufacturing, 2004. **35**(10): p. 1135-1147.

21. Wen, J., Z. Xia, and F. Choy, *Damage detection of carbon fiber reinforced polymer composites via electrical resistance measurement*. Composites Part B: Engineering, 2011. **42**(1): p. 77-86.

22. Aly, K., A. Li, and P.D. Bradford, *In-situ monitoring of woven glass fiber reinforced composites under flexural loading through embedded aligned carbon nanotube sheets*. Journal of Composite Materials, 2018. **52**(20): p. 2777-2788.

23. Souri, H. and D. Bhattacharyya, *Electrical conductivity of the graphene nanoplatelets coated natural and synthetic fibres using electrophoretic deposition technique*. International Journal of Smart and Nano Materials, 2018. **9**(3): p. 167-183.

24. Li, Z., et al., *Carbon-based functional nanomaterials: Preparation, properties and applications*. Composites Science and Technology, 2019. **179**: p. 10-40.

25. Nam, I.W., et al., *Mechanical properties and piezoresistive sensing capabilities of FRP composites incorporating CNT fibers*. Composite Structures, 2017. **178**: p. 1-8.

26. Fiorillo, A.S., C.D. Critello, and S.A. Pullano, *Theory, technology and applications of piezoresistive sensors: A review*. Sensors and Actuators A: Physical, 2018. **281**: p. 156-175.

27. Han, S., et al., *Thermally and electrically conductive multifunctional sensor based on epoxy/graphene composite*. Nanotechnology, 2020. **31**(7): p. 075702.

28. Du, X., et al., *Graphene/epoxy interleaves for delamination toughening and monitoring of crack damage in carbon fibre/epoxy composite laminates*. Composites Science and Technology, 2017. **140**: p. 123-133.

29. Yi, M. and Z. Shen, *A review on mechanical exfoliation for scalable production of graphene*. J. Mater. Chem. A, 2015. **3**.

30. Zhang, L., et al., *Size-controlled synthesis of graphene oxide sheets on a large scale using chemical exfoliation*. Carbon, 2009. **47**(14): p. 3365-3368.

31. Ciesielski, A. and P. Samorì, *Graphene via sonication assisted liquid-phase exfoliation*. Chemical Society Reviews, 2014. **43**(1): p. 381-398.

32. Balaji, R. and M. Sasikumar, *Graphene based strain and damage prediction system for polymer composites*. Composites Part A: Applied Science and Manufacturing, 2017. **103**: p. 48-59.

33. Mahmood, H., et al., *Mechanical properties and strain monitoring of glass-epoxy composites with graphene-coated fibers*. Composites Part A: Applied Science and Manufacturing, 2018. **107**: p. 112-123.

34. Han, S., et al., *Epoxy/graphene film for lifecycle self-sensing and multifunctional applications*. Composites Science and Technology, 2020. **198**.

35. Sandy Lee, I.Y., et al., *Direct measurement of polymer temperature during laser ablation using a molecular thermometer*. Journal of Applied Physics, 1992. **72**(6): p. 2440-2448.

36. Lin, J., et al., *Laser-induced porous graphene films from commercial polymers*. Nat Commun, 2014. **5**: p. 5714.

37. Luo, Y.-R., *Comprehensive handbook of chemical bond energies*. 2007: CRC press.

38. Bityurin, N. and A. Malyshev, *Bulk photothermal model for laser ablation of polymers by nanosecond and subpicosecond pulses*. Journal of Applied Physics, 2002. **92**(1): p. 605-613.

39. Luong, D.X., et al., *Laminated Object Manufacturing of 3D-Printed Laser-Induced Graphene Foams*. Adv Mater, 2018. **30**(28): p. e1707416.

40. Wang, Y., et al., *Laser-Induced Freestanding Graphene Papers: A New Route of Scalable Fabrication with Tunable Morphologies and Properties for Multifunctional Devices and Structures*. Small, 2018. **14**(36): p. e1802350.

41. Duy, L.X., et al., *Laser-induced graphene fibers*. Carbon, 2018. **126**: p. 472-479.

42. Burke, M., et al., *Fabrication and Electrochemical Properties of Three-Dimensional (3D) Porous Graphitic and Graphenelike Electrodes Obtained by Low-Cost Direct Laser Writing Methods*. ACS Omega, 2020. **5**(3): p. 1540-1548.

43. You, X., et al., *Novel Graphene Planar Architecture with Ultrahigh Stretchability and Sensitivity*. ACS Appl Mater Interfaces, 2020. **12**(16): p. 18913-18923.

44. Luo, S., P.T. Hoang, and T. Liu, *Direct laser writing for creating porous graphitic structures and their use for flexible and highly sensitive sensor and sensor arrays*. Carbon, 2016. **96**: p. 522-531.

45. Romero, F.J., et al., *In-Depth Study of Laser Diode Ablation of Kapton Polyimide for Flexible Conductive Substrates*. Nanomaterials (Basel), 2018. **8**(7).

46. Wang, L., et al., *A Comparative Study of Laser-Induced Graphene by CO2 Infrared Laser and 355 nm Ultraviolet (UV) Laser*. Micromachines (Basel), 2020. **11**(12).

47. Zhu, Y., et al., *Fabrication of Low-Cost and Highly Sensitive Graphene-Based Pressure Sensors by Direct Laser Scribing Polydimethylsiloxane*. ACS Appl Mater Interfaces, 2019. **11**(6): p. 6195-6200.

48. Rahimi, R., et al., *Highly stretchable and sensitive unidirectional strain sensor via laser carbonization*. ACS Appl Mater Interfaces, 2015. **7**(8): p. 4463-70.

49. Stanford, M.G., et al., *Laser-Induced Graphene Triboelectric Nanogenerators*. ACS Nano, 2019. **13**(6): p. 7166-7174.

50. Nasser, J., et al., *Laser induced graphene fibers for multifunctional aramid fiber reinforced composite*. Carbon, 2020. **158**: p. 146-156.

51. Carvalho, A.F., et al., *Laser-Induced Graphene Strain Sensors Produced by Ultraviolet Irradiation of Polyimide*. Advanced Functional Materials, 2018. **28**(52).

52. Bobinger, M.R., et al., *Flexible and robust laser-induced graphene heaters photothermally scribed on bare polyimide substrates*. Carbon, 2019. **144**: p. 116-126.

53. Groo, L., et al., *Laser induced graphene for in situ damage sensing in aramid fiber reinforced composites*. Composites Science and Technology, 2021. **201**.

54. Steinke, K., L. Groo, and H.A. Sodano, *Laser induced graphene for in-situ ballistic impact damage and delamination detection in aramid fiber reinforced composites*. Composites Science and Technology, 2021. **202**: p. 108551.

55. Wang, G., et al., *A self-converted strategy toward multifunctional composites with laser-induced graphitic structures*. Composites Science and Technology, 2020. **199**.

56. Luong, D.X., et al., *Laser-Induced Graphene Composites as Multifunctional Surfaces*. ACS Nano, 2019. **13**(2): p. 2579-2586.

57. Groo, L., et al., *Transfer printed laser induced graphene strain gauges for embedded sensing in fiberglass composites*. Composites Part B: Engineering, 2021. **219**.

58. Huang, L., et al., *Wearable Flexible Strain Sensor Based on Three-Dimensional Wavy Laser-Induced Graphene and Silicone Rubber*. Sensors (Basel), 2020. **20**(15).

59. Yao, Y., et al., *Self-Sealing Carbon Patterns by One-Step Direct Laser Writing and Their Use in Multifunctional Wearable Sensors*. ACS Appl Mater Interfaces, 2020. **12**(45): p. 50600-50609.

60. Li, G., *Direct laser writing of graphene electrodes*. Journal of Applied Physics, 2020. **127**(1).

61. Groo, L., et al., *Laser induced graphene in fiberglass-reinforced composites for strain and damage sensing*. Composites Science and Technology, 2020. **199**.

62. Kulyk, B., et al., *Laser-Induced Graphene from Paper for Mechanical Sensing*. ACS Appl Mater Interfaces, 2021. **13**(8): p. 10210-10221.

63. Yang, W., et al., *Fabrication of Smart Components by 3D Printing and Laser-Scribing Technologies*. ACS Appl Mater Interfaces, 2020. **12**(3): p. 3928-3935.

64. Dallinger, A., et al., *Stretchable and Skin-Conformable Conductors Based on Polyurethane/Laser-Induced Graphene*. ACS Appl Mater Interfaces, 2020. **12**(17): p. 19855-19865.

65. Wang, H., et al., *A soft and stretchable electronics using laser-induced graphene on polyimide/PDMS composite substrate*. npj Flexible Electronics, 2022. **6**(1).

66. Wang, W., et al., *Fingerprint-Inspired Strain Sensor with Balanced Sensitivity and Strain Range Using Laser-Induced Graphene*. ACS Appl Mater Interfaces, 2022. **14**(1): p. 1315-1325.

67. Kulyk, B., et al., *Laser‐Induced Graphene from Paper by Ultraviolet Irradiation: Humidity and Temperature Sensors*. Advanced Materials Technologies, 2022. **7**(7).

68. Vivaldi, F.M., et al., *Three-Dimensional (3D) Laser-Induced Graphene: Structure, Properties, and Application to Chemical Sensing*. ACS Appl Mater Interfaces, 2021. **13**(26): p. 30245-30260.

69. Stanford, M.G., et al., *Laser-Induced Graphene for Flexible and Embeddable Gas Sensors*. ACS Nano, 2019. **13**(3): p. 3474-3482.

70. Wang, Y., et al., *Freestanding laser induced graphene paper based liquid sensors*. Carbon, 2019. **153**: p. 472-480.

71. Houeix, Y., et al., *Responsible Humidity Sensor by Direct Laser Writing on Cork Substrate*. Advanced Sustainable Systems, 2024.

72. C. Claro, P.I., et al., *Sustainable carbon sources for green laser-induced graphene: A perspective on fundamental principles, applications, and challenges*. Applied Physics Reviews, 2022. **9**(4).

73. Imbrogno, A., et al., *Laser-Induced Graphene Supercapacitors by Direct Laser Writing of Cork Natural Substrates*. ACS Applied Electronic Materials, 2022. **4**(4): p. 1541-1551.

74. Silvestre, S.L., et al., *Cork derived laser-induced graphene for sustainable green electronics*. Flexible and Printed Electronics, 2022. **7**(3): p. 035021.

75. Uribe-Riestra, G.C., et al., *Influence of electrode configuration on impact damage evaluation of self-sensing hierarchical composites*. Journal of Intelligent Material Systems and Structures, 2020. **31**(11): p. 1416-1429.

76. Chyan, Y., et al., *Laser-Induced Graphene by Multiple Lasing: Toward Electronics on Cloth, Paper, and Food*. ACS Nano, 2018. **12**(3): p. 2176-2183.

77. Eckmann, A., et al., *Probing the nature of defects in graphene by Raman spectroscopy*. Nano Lett, 2012. **12**(8): p. 3925-30.

78. Lee, M.D., M.A. Butavicius, and R.E. Reilly, *Visualizations of binary data: A comparative evaluation*. International Journal of Human-Computer Studies, 2003. **59**(5): p. 569-602.

79. Sharma, A., et al. *Prediction of the Fracture Toughness of Silicafilled Epoxy Composites using K-Nearest Neighbor (KNN) Method*. in *2020 International Conference on Computational Performance Evaluation (ComPE)*. 2020.

80. Vitola, J., et al., *A Sensor Data Fusion System Based on k-Nearest Neighbor Pattern Classification for Structural Health Monitoring Applications*. Sensors (Basel), 2017. **17**(2).

81. Diaz-Escobar, J., et al., *Classification and Characterization of Damage in Composite Laminates Using Electrical Resistance Tomography and Supervised Machine Learning*. Structural Control and Health Monitoring, 2023. **2023**: p. 1-19.

82. Chawla, N., et al., *SMOTE: Synthetic Minority Over-sampling Technique*. J. Artif. Intell. Res. (JAIR), 2002. **16**: p. 321-357.

83. Pedregosa, F., et al., *Scikit-learn: Machine Learning in Python*. J. Mach. Learn. Res., 2011. **12**(null): p. 2825–2830.

84. Bradski, G. and A. Kaehler, *Learning OpenCV - computer vision with the OpenCV library: software that sees*. 2008.

85. Fawcett, T., *An introduction to ROC analysis*. Pattern Recognition Letters, 2006. **27**(8): p. 861-874.

86. Sokolova, M. and G. Lapalme, *A systematic analysis of performance measures for classification tasks*. Information Processing & Management, 2009. **45**(4): p. 427-437.

87. Powers, D., *Evaluation: From Precision, Recall and F-Factor to ROC, Informedness, Markedness & Correlation*. Mach. Learn. Technol., 2008. **2**.

88. Chen, X., et al., *Laser-induced graphene as an embedded sensor for impact damage in composite structures assisted by machine learning*. Structural Health Monitoring. **0**(0): p. 14759217241311516.

89. O'Brien, D.J., P.T. Mather, and S.R. White, *Viscoelastic Properties of an Epoxy Resin during Cure*. Journal of Composite Materials, 2001. **35**(10): p. 883-904.

90. Papanicolaou, G.C., S.P. Zaoutsos, and E.A. Kontou, *Fiber orientation dependence of continuous carbon/epoxy composites nonlinear viscoelastic behavior.* Composites Science and Technology, 2004. **64**(16): p. 2535-2545.

91. Chhetry, A., et al., *MoS2-Decorated Laser-Induced Graphene for a Highly Sensitive, Hysteresis-free, and Reliable Piezoresistive Strain Sensor.* ACS Applied Materials & Interfaces, 2019. **11**(25): p. 22531-22542.

92. Kelly, A. and W.R. Tyson, *Tensile properties of fibre-reinforced metals: Copper/tungsten and copper/molybdenum*. Journal of the Mechanics and Physics of Solids, 1965. **13**(6): p. 329-350.

93. Kim, B.J. and I.W. Nam, *Experimental Investigation into the Mechanical and Piezoresistive Sensing Properties of Recycled Carbon-Fiber-Reinforced Polymer Composites for Self-Sensing Applications*. Polymers (Basel), 2024. **16**(17).

94. Robert, C., et al., *Multifunctional Carbon Nanotubes Enhanced Structural Composites with Improved Toughness and Damage Monitoring.* Journal of Composites Science, 2019. **3**(4).

95. Jamison, R.D., *The role of microdamage in tensile failure of graphite/epoxy laminates*. Composites Science and Technology, 1985. **24**(2): p. 83-99.

96. Kirkpatrick, S., *Percolation and Conduction.* Reviews of Modern Physics, 1973. **45**(4): p. 574-588.

97. McLachlan, D.S., *Analytical Functions for the dc and ac Conductivity of Conductor-Insulator Composites*. Journal of Electroceramics, 2000. **5**(2): p. 93-110.

98. Stauffer, D., & Aharony, A., *Introduction To Percolation Theory: Second Edition (2nd ed.). Taylor & Francis*. 1992.

99. Li, B., B. Wang, and S.R. Reid, *Effective elastic properties of randomly distributed void models for porous materials*. International Journal of Mechanical Sciences, 2010. **52**(5): p. 726-732.

100. Molinari, A. and T.W. Wright, *A physical model for nucleation and early growth of voids in ductile materials under dynamic loading.* Journal of the Mechanics and Physics of Solids, 2005. **53**(7): p. 1476-1504.

101. Li, J., et al., *Correlations between Percolation Threshold, Dispersion State, and Aspect Ratio of Carbon Nanotubes*. Advanced Functional Materials, 2007. **17**(16): p. 3207-3215.

102. Wong, T.-f., et al., *Microcrack statistics, Weibull distribution and micromechanical modeling of compressive failure in rock.* Mechanics of Materials, 2006. **38**(7): p. 664-681.

103. Prabhakaran, S., et al., *Biodegradation behaviour of green composite sandwich made of flax and agglomerated cork.* Polymers and Polymer Composites, 2022. **30**.

104. Ogihara, S. and N. Takeda, *Interaction between transverse cracks and delamination during damage progress in CFRP cross-ply laminates*. Composites Science and Technology, 1995. **54**(4): p. 395-404.

105. Mehmood, A., et al., *Graphene based nanomaterials for strain sensor application—a review*. Journal of Environmental Chemical Engineering, 2020. **8**(3): p. 103743.

106. Stankovich, S., et al., *Graphene-based composite materials*. Nature, 2006. **442**(7100): p. 282-286.

107. Pagès, H., et al., *Demonstration of paper cutting using single emitter laser diode and infrared-absorbing ink*. Optics Express, 2005. **13**: p. 2351-2357.

108. Lei, Z., et al., *Interfacial Micromechanics in Fibrous Composites: Design, Evaluation, and Models*. TheScientificWorldJournal, 2014. **2014**: p. 282436.

109. Wang, W., et al., *Scorpion-inspired dual-bionic, microcrack-assisted wrinkle based laser induced graphene-silver strain sensor with high sensitivity and broad working range for wireless health monitoring system*. Nano Research, 2022. **16**(1): p. 1228-1241.

110. Higson, G.R., *Recent advances in strain gauges*. Journal of Scientific Instruments, 1964. **41**(7): p. 405.

111. Meng, Q., et al., *Damage monitoring of aircraft structural components based on large-area flexible graphene strain sensors*. Sensors and Actuators A: Physical, 2024. **369**: p. 115092.

112. Bažant, Z.P., *Size effect on structural strength: a review*. Archive of Applied Mechanics, 1999. **69**(9): p. 703-725.

113. Sakorikar, T., et al., *Thickness-dependent Crack Propagation in Uniaxially Strained Conducting Graphene Oxide Films on Flexible Substrates*. Scientific Reports, 2017. **7**(1): p. 2598.

114. Alidoust, A., et al., *A numerical conductive network model for investigating the strain-sensing response of graphene nanoplatelets-filled elastomeric strain sensors*. Results in Engineering, 2024. **24**: p. 103341.

115. Park, B., et al., *Dramatically Enhanced Mechanosensitivity and Signal-to-Noise Ratio of Nanoscale Crack-Based Sensors: Effect of Crack Depth*. Adv Mater, 2016. **28**(37): p. 8130-8137.

116. Meunier, V., et al., *Physical properties of low-dimensional ${sp}^{2}$-based carbon nanostructures*. Reviews of Modern Physics, 2016. **88**(2): p. 025005.

117. Gillet, C., et al., *Parameters Influencing Moisture Diffusion in Epoxy-Based Materials during Hygrothermal Ageing-A Review by Statistical Analysis*. Polymers (Basel), 2022. **14**(14).

118. Cai, L.W. and Y. Weitsman, *Non-Fickian Moisture Diffusion in Polymeric Composites*. Journal of Composite Materials, 1994. **28**(2): p. 130-154.

119. Schindelin, J., et al., *Fiji: an open-source platform for biological-image analysis*. Nature Methods, 2012. **9**(7): p. 676-682.

120. Lazic, V., et al., *Sample Preparation for Repeated Measurements on a Single Liquid Droplet Using Laser-Induced Breakdown Spectroscopy*. Appl Spectrosc, 2017. **71**(4): p. 670-677.

121. Airale, A.G., et al., *Moisture effect on mechanical properties of polymeric composite materials*. AIP Conference Proceedings, 2016. **1736**(1).

122. Melo, R.Q.C., et al., *Water Absorption Process in Polymer Composites: Theory Analysis and Applications*, in *Transport Phenomena in Multiphase Systems*, J.M.P.Q. Delgado and A.G. Barbosa de Lima, Editors. 2018, Springer International Publishing: Cham. p. 219-249.

123. Merdas, I., et al., *Factors governing water absorption by composite matrices*. Composites Science and Technology, 2002. **62**(4): p. 487-492.

124. McKenzie, S. and H.C. Kang, *Squeezing water clusters between graphene sheets: energetics, structure, and intermolecular interactions*. Physical Chemistry Chemical Physics, 2014. **16**(47): p. 26004-26015.

125. Arnold, J.C., S.M. Alston, and F. Korkees, *An assessment of methods to determine the directional moisture diffusion coefficients of composite materials*. Composites Part A: Applied Science and Manufacturing, 2013. **55**: p. 120-128.

126. Suh, D.-W., et al., *Equilibrium Water Uptake of Epoxy/Carbon Fiber Composites in Hygrothermal Environmental Conditions*. Journal of Composite Materials, 2001. **35**(3): p. 264-278.

127. Wang, C., J. Wang, and A.H. Barber, *Stress concentrations in nanoscale defective graphene*. AIP Advances, 2017. **7**(11): p. 115001.

128. Baltazar-y-Jimenez, A. and A. Bismarck, *Wetting behaviour, moisture up-take and electrokinetic properties of lignocellulosic fibres*. Cellulose, 2007. **14**(2): p. 115-127.

Appendix A

KNN classification code for cork-derived LIG composites in impact sensing

```
import numpy as np
import operator
import matplotlib as mpl
import matplotlib.pyplot as plt
import pandas as pd
import sklearn
from sklearn import neighbors
from sklearn.model_selection import train_test_split
from sklearn.neighbors import KNeighborsClassifier#KNN
from sklearn.preprocessing import label_binarize
from sklearn import metrics
from scipy.stats import zscore
df1['Resistance Change'] = np.clip(df1['Resistance Change'], a_min=None, a_max=threshold)
df1['Resistance Change'] = zscore(df1['Resistance Change'])
df1['Absolute_Resistance Change'] = np.clip(df1['Absolute_Resistance Change'],
a_min=lower_threshold_a, a_max=upper_threshold_a)
df1['Absolute_Resistance Change'] = zscore(df1['Absolute_Resistance Change'])
bestScore=0
bestK=-1
bestWeight=" "
# weight==uniform
for k in range(1,10):
clf = KNeighborsClassifier(n_neighbors=k,weights="uniform")
clf.fit(X_train,Y_train)
scor=clf.score(X_test,Y_test)
if scor > bestScore:
bestScore=scor
bestK=k
bestWeight="uniform"
# weight==distance
for k in range(1,10):
for p in range(1,4):
clf=KNeighborsClassifier(n_neighbors=k,weights="distance",p=p)
clf.fit(X_train,Y_train)
scor = clf.score(X_test, Y_test)
if scor > bestScore:
bestScore = scor
bestK = k
bestWeight = "distance"
print("the best n_neighbors", bestK)
print("the best weights", bestWeight)
print("the best p", p)
best_knn = grid_search.best_estimator_
accuracy = best_knn.score(X_test, Y_test)
print("test accuracy", accuracy)
```

Appendix B Curve Fitting code for cork-derived LIG

```
import numpy as np
from sklearn.metrics import r2_score
def curve_fit(A, t):
 x = np.linspace(0, 1, 100)
 # three curve to be fitted
 Y1 = (400*A + 1.76)*x + (200000*A*t + 704*A + 1.1932)*x**2
 Y2 = (225*A + 1.76)*x + (112500*A*t + 396*A + 1.1932)*x**2
 Y3 = (144*A + 1.76)*x + (72000*A*t + 253.44*A + 1.1932)*x**2
 # target value of fitting
 y1 = A1*x**2 + B1*x
 y2 = A2*x**2 + B2*x
 y3 = A3*x**2 + B3*x
 # R-squared value
 r2_1 = r2_score(y1, Y1)
 r2_2 = r2_score(y2, Y2)
 r2_3 = r2_score(y3, Y3)
 avg_r2 = (r2_1 + r2_2 + r2_3) / 3
 return avg_r2, r2_1, r2_2, r2_3, Y1, Y2, Y3
# searching range
A_range = np.linspace(0, 0.0401, 100)
t_range = np.linspace(0, 2.01, 100)
# grid search
best_avg_r2 = -np.inf
best_A = best_t = None
best_r2_1 = best_r2_2 = best_r2_3 = None
best_Y1 = best_Y2 = best_Y3 = None
for A in A_range:
 for t in t_range:
 avg_r2, r2_1, r2_2, r2_3, Y1, Y2, Y3 = curve_fit(A, t) if avg_r2 > best_avg_r2:
 best_avg_r2 = avg_r2
 best_A, best_t = A, t
 best_r2_1, best_r2_2, best_r2_3 = r2_1, r2_2, r2_3
 best_Y1, best_Y2, best_Y3 = Y1, Y2, Y3
# output
print(f"Best A: {best_A:.6f} ")
print(f"Best t: {best_t:.6f}")
print(f"Average R-squared: {best_avg_r2:.6f}")
print(f"R-squared 1: {best_r2_1:.6f}")
print(f"R-squared 2: {best_r2_2:.6f}")
print(f"R-squared 3: {best_r2_3:.6f}")
# visualisation
import matplotlib.pyplot as plt
x = np.linspace(0, 1, 100)
y1 = 5863.29*x**2 + 14.96*x
y2 = 3421.01*x**2 + 10.32*x
y3 = 2089.93*x**2 + 3.20*x
plt.figure(figsize=(12, 8))
plt.plot(x, y1, label='Target y1')
plt.plot(x, y2, label='Target y2')
plt.plot(x, y3, label='Target y3')
plt.plot(x, best_Y1, '--', label='Fitted Y1')
plt.plot(x, best_Y2, '--', label='Fitted Y2')
```

```
plt.plot(x, best_Y3, '--', label='Fitted Y3')
plt.legend()
plt.title('Target vs Fitted Curves')
plt.xlabel('x')
plt.ylabel('y')
plt.show()
```